

UNIVERSITY OF LEEDS

DOCTORAL THESIS

---

**Simulating the lattice thermal  
conductivity of iron-bearing bridgmanite  
with implications on core-mantle  
boundary heat flux**

---

*Author:*

**Ben TODD**

*Supervisor:*

Dr. Stephen STACKHOUSE

Dr. Andrew M. WALKER

Dr. Jon E. MOUND

*A thesis submitted in fulfillment of the requirements*

*for the degree of Doctor of Philosophy*

*in the*

**Institute of Geophysics and Tectonics**

**School of Earth and Environment**

June 7, 2019

## Declaration of Authorship

I, Ben TODD, declare that this thesis titled, “Simulating the lattice thermal conductivity of iron-bearing bridgmanite with implications on core-mantle boundary heat flux” and the work presented in it are my own. I confirm that:

- This work was done wholly or mainly while in candidature for a research degree at this University.
- Where any part of this thesis has previously been submitted for a degree or any other qualification at this University or any other institution, this has been clearly stated.
- Where I have consulted the published work of others, this is always clearly attributed.
- Where I have quoted from the work of others, the source is always given. With the exception of such quotations, this thesis is entirely my own work.
- I have acknowledged all main sources of help.
- Where the thesis is based on work done by myself jointly with others, I have made clear exactly what was done by others and what I have contributed myself.

Signed:

---

Date:

---



*Do it!*  
*Just do it!*

*Don't let your dreams be dreams.*  
*Yesterday you said tomorrow, so just do it!*  
*Make your dreams come true!*  
*Just do it!*

*Some people dream of success,*  
*while you're gonna wake up,*  
*and work hard at it!*  
*Nothing is impossible!*

*You should get to the point,*  
*where anyone else would quit,*  
*and you're not going to stop there.*  
*No, what are you waiting for?*

*Do it!*  
*Just do it!*  
*Yes you can!*  
*Just do it!*

*If you're tired of starting over,*  
*stop*  
*giving*  
*up.*

Shia LeBeouf



UNIVERSITY OF LEEDS

# *Abstract*

Faculty of Environment

School of Earth and Environment

Doctor of Philosophy

**Simulating the lattice thermal conductivity of iron-bearing bridgmanite with  
implications on core-mantle boundary heat flux**

by Ben TODD

The Thesis Abstract is written here (and usually kept to just this page). The page is kept centered vertically so can expand into the blank space above the title too...





## *Acknowledgements*

The acknowledgments and the people to thank go here, don't forget to include your project advisor...



# Contents

<b>Declaration of Authorship</b>	<b>iii</b>
<b>Abstract</b>	<b>vii</b>
<b>Acknowledgements</b>	<b>ix</b>
<b>1 June 7th - Thermal conductivity and the Earth's interior</b>	<b>1</b>
1.1 Structure of the Earth . . . . .	1
1.1.1 Lithosphere and mantle transition zone . . . . .	1
1.1.2 Lower mantle . . . . .	2
1.1.3 Inner and outer core . . . . .	5
1.2 Geophysical processes . . . . .	5
1.2.1 Mantle dynamics . . . . .	6
1.2.2 Heat flow . . . . .	7
1.2.3 Geomagnetism . . . . .	7
1.3 Defining thermal conductivity . . . . .	8
1.3.1 Man-made applications considering thermal conductivity . . . . .	9
1.4 Components of thermal conductivity . . . . .	10
1.4.1 Electron . . . . .	10
1.4.2 Photon . . . . .	10
1.4.3 Phonon . . . . .	11
1.5 What affects thermal conductivity? . . . . .	13
1.5.1 Pressure-dependence . . . . .	13
1.5.2 Temperature-dependence . . . . .	14
1.5.3 Composition . . . . .	14
1.6 Previous work . . . . .	16
1.6.1 Experiments . . . . .	16

1.6.2	Calculations . . . . .	17
1.6.3	Radiative conductivity . . . . .	20
1.7	Project summary . . . . .	23
1.7.1	Aims & objectives . . . . .	23
1.7.2	Thesis outline . . . . .	23
<b>2</b>	<b>Computing thermal conductivity</b>	<b>25</b>
2.1	Atomic-scale modelling . . . . .	25
2.1.1	Computational regimes . . . . .	26
	Molecular dynamics . . . . .	26
	Lattice dynamics . . . . .	28
2.1.2	Calculating atomic interactions . . . . .	28
	Density functional theory . . . . .	28
	Classical interatomic potentials . . . . .	29
2.1.3	Finite-size effects . . . . .	29
	Why use LAMMPS? . . . . .	30
2.1.4	Oganov's bridgmanite potential . . . . .	30
	CALIBRATING CUTOFFS . . . . .	31
	COMPARING RESULTS . . . . .	32
2.2	Computing thermal conductivity . . . . .	36
2.2.1	Direct method . . . . .	36
	System setup . . . . .	37
	Data processing . . . . .	38
	Finite-size effects . . . . .	40
2.2.2	Green-Kubo . . . . .	41
	Methodology . . . . .	41
	Data processing . . . . .	42
2.3	Previous work . . . . .	43
2.3.1	Method comparison . . . . .	44
2.3.2	Bridgmanite FSE . . . . .	44
2.4	Conclusion . . . . .	45

<b>3</b>	<b>Examining finite-size effects in thermal conductivity computations</b>	<b>47</b>
3.1	Introduction . . . . .	47
3.1.1	Finite-size effects . . . . .	47
3.2	Green-Kubo . . . . .	48
3.2.1	Correlation length convergence . . . . .	49
3.2.2	Integral sample convergence . . . . .	51
3.2.3	Simulation length convergence . . . . .	52
3.2.4	Finite-size effect convergence . . . . .	54
3.3	Direct method . . . . .	56
3.3.1	Setting up supercells . . . . .	56
3.3.2	FIDDLING WITH BIN WIDTH . . . . .	58
3.3.3	Temperature gradient convergence . . . . .	59
3.3.4	Simulation time convergence . . . . .	59
3.3.5	Data processing . . . . .	62
3.3.6	Inverse extrapolation procedure . . . . .	62
3.3.7	Finite-size effects . . . . .	63
	4000 K . . . . .	63
	1000 K . . . . .	66
3.3.8	Explaining CSA effect . . . . .	68
3.4	Summary . . . . .	68
<b>4</b>	<b>Modelling the thermal conductivity of Fe-bearing bridgmanite at the CMB</b>	<b>71</b>
4.1	Simulating the effect of atomic impurities . . . . .	72
4.1.1	How do impurities affect conductivity? . . . . .	72
4.1.2	Why does this model work? . . . . .	73
4.1.3	What effects the magnitude of impurity scattering? . . . . .	73
4.1.4	Phonon frequency and relaxation time . . . . .	75
4.2	Methodology . . . . .	77
4.2.1	How does iron behave? . . . . .	77
4.2.2	Where do the impurities go? . . . . .	79
4.3	Results . . . . .	79

4.4	Parameterising composition and temperature effects on CMB conductivity . . . . .	82
4.4.1	Compositional dependence . . . . .	84
4.4.2	Why does this model work? . . . . .	86
4.4.3	Temperature dependence . . . . .	88
4.5	Discussion . . . . .	91
4.5.1	Significance of mass and atomic interactions on the iron potential . . . . .	91
4.5.2	Backcalculating mean free path . . . . .	91
4.5.3	Scaling MFP to quantify phonon-defect scattering . . . . .	93
4.5.4	$C(1 - C)$ model limitations . . . . .	95
<b>5</b>	<b>Using STUFF to do THINGS</b>	<b>101</b>
5.1	Draft words . . . . .	101
5.1.1	Notes . . . . .	103
<b>6</b>	<b>Summary/Discussion/Conclusion</b>	<b>105</b>
6.1	Main Section 1 . . . . .	105
6.1.1	Subsection 1 . . . . .	105
<b>A</b>	<b>Frequently Asked Questions</b>	<b>107</b>
A.1	How do I change the colors of links? . . . . .	107
	<b>Bibliography</b>	<b>109</b>

# List of Figures

1.1	EARTH STRUCTURE DIAGRAM . . . . .	2
1.2	TRONNES EARTH STRUCTURE DIAGRAM . . . . .	3
1.3	TRONNES PERIDOTITE COMPOSITION DIAGRAM . . . . .	4
1.4	PHONON TYPE DIAGRAM . . . . .	12
1.5	DEBYE MODEL . . . . .	14
1.6	KAPPA AGAINST TEMP . . . . .	15
1.7	Thermal conductivity against Fe-content . . . . .	19
2.1	MD process flowchart draft . . . . .	26
2.2	BUCK CUTOFF . . . . .	32
2.3	The unit cell represents the smallest box of atoms that can be replicated to produce a crystal structure. A supercell is an arrangement of unit cells. . . . .	38
2.4	DIRECT METHOD SCHEMATIC . . . . .	39
2.5	Idealised example of linear extrapolation procedure. Inverse computed conductivities are plotted against inverse simulation lengths. Extrapolation to y-axis gives conductivity of an infinite system length, i.e. the bulk material. . . . .	40
2.6	Normalised ACF. Correlation is taken over a longer length than shown on this plot (100 ps), however the function decays to less than 1% of its initial value at 2 ps. It continues to oscillate about zero, with a positive average value. . . . .	41

2.7	Integrated ACF, multiplied by constants to get thermal conductivity. Large variation in the first 1 ps corresponds to the correlation time where the ACF is unconverged (still decaying / large oscillations). Thermal conductivity is averaged from correlation time of 5 – 10 ps (region in red box). . . . .	43
3.1	gk int 3000 000pc trio . . . . .	50
3.2	gk int 1000 000pc trio . . . . .	50
3.3	gk simulation length convergence . . . . .	52
3.4	gk integrals, simulation length convergence . . . . .	53
3.5	gk fse 4k . . . . .	54
3.6	gk fse 1k . . . . .	55
3.7	direct temperature profile 3 . . . . .	57
3.8	direct bin width . . . . .	58
3.9	direct conv . . . . .	60
3.10	direct conv . . . . .	61
3.11	direct inv 4000 . . . . .	63
3.12	direct inv cut up 4000 . . . . .	65
3.13	direct extrap gk comp 4000 . . . . .	65
3.14	direct inv 1000 . . . . .	66
3.15	direct inv cutup 1000 03 . . . . .	67
3.16	direct inv cutup 1000 01 . . . . .	68
4.1	CONTENTS BIT . . . . .	76
4.2	CONTENTS BIT . . . . .	80
4.3	CONTENTS BIT . . . . .	81
4.4	CONTENTS BIT . . . . .	82
4.5	CONTENTS BIT . . . . .	83
4.6	CONTENTS BIT . . . . .	86
4.7	CONTENTS BIT . . . . .	87
4.8	CONTENTS BIT . . . . .	88
4.9	CONTENTS BIT . . . . .	90
4.10	kc iso pot full . . . . .	92



4.11	kc 4000 mfp norm . . . . .	94
4.12	gk mfp scattering 4000K . . . . .	98
4.13	gk mfp scattering 1000K . . . . .	99
4.14	gk mfp ph-d significance 4000K . . . . .	100
4.15	gk mfp ph-d mass demo . . . . .	100
5.1	SPHERICAL HARMONICS . . . . .	102



# List of Tables

1.1	CONTENTS CAPTION . . . . .	22
2.1	CONTENTS BIT . . . . .	31
2.2	Comparison of $\text{MgSiO}_3$ perovskite properties calculated using the Oganov et al. (2000) potential at 0 GPa . . . . .	34
2.3	Comparison of calculated $\text{MgSiO}_3$ peroskite unit cell parameters with Ammann et al., 2014 . . . . .	35
3.1	CONTENTS1 . . . . .	55
3.2	CONTENTS2 . . . . .	55
4.1	CONTENTS BIT . . . . .	78
4.2	CONTENTS BIT . . . . .	85
4.3	CONTENTS BIT . . . . .	91
4.4	4000 K GK MFP table . . . . .	97



# List of Abbreviations

<b>CMB</b>	Core-mantle boundary
<b>LLSVP</b>	Large, low-shear-velocity province
<b>ULVZ</b>	Ultra low velocity zone
<b>TBL</b>	Thermal boundary layer
<b>DAC</b>	Diamond anvil cell
<b>MgSiO<sub>3</sub></b>	Magnesium Silicate
<b>FeSiO<sub>3</sub></b>	Iron Silicate
<b>bdg</b>	bridgmanite
<b>pv</b>	perovskite
<b>ppv</b>	post-perovskite
<b>LAMMPS</b>	Large-scale Atomic/Molecular Massively Parallel Simulator
<b>DFT</b>	Density Functional Theory
<b>MD</b>	Molecular Dynamics
<b>EMD</b>	Equilibrium Molecular Dynamics
<b>NEMD</b>	Non-equilibrium Molecular Dynamics
<b>DM</b>	Direct Method
<b>GK</b>	Green-Kubo
<b>ACF</b>	Auto-correlation function
<b>MFP</b>	Mean free path
<b>FSE</b>	Finite-size effects
<b>BPT</b>	Ballistic phonon transport



# Physical Constants

Boltzmann constant  $k_B = 1.380\,648\,528 \times 10^{-23} \text{ J K}^{-1}$

Boltzmann constant  $k_B = 8.617\,330\,350 \times 10^{-5} \text{ eV/K}$





# List of Symbols

$a$	distance	m
$P$	power	W (J s <sup>-1</sup> )
$\omega$	angular frequency	rad



*For/Dedicated to/To my...*



## Chapter 1

# June 7th - Thermal conductivity and the Earth's interior

### 1.1 Structure of the Earth

The average radius of the Earth is 6371 km, the properties of which change dramatically with depth to the centre. I will be focused on the lower mantle, particularly the region close to the core (the core mantle boundary, CMB). Events in the lower mantle influence (and are influenced by) the upper mantle and lithosphere above, and the core below (see Figure 1.1). Heat transport throughout the Earth is influenced by thermal conductivity, which in turn affects the dynamics of the system, the surface expression of this being plate tectonics. Heat flow also affects the core geodynamo, which produces the Earth's magnetic field (see Figure 1.2).

#### 1.1.1 Lithosphere and mantle transition zone

!!! IS THE WADSLEYITE TO RINGWOODITE CHANGE SUDDEN OR GRADUAL?

The lithosphere and upper mantle lie above the transition zone (down to 660 km depth), the bottom of which marks the top of the lower mantle. Although the composition of these regions is similar to that of the lower mantle, the physical conditions and mineral phases are different. Eruptive and subductive behaviour associated with plate tectonics is perhaps the most obvious consequence of mantle dynamics at the Earth's surface, and generally to humanity.

The "rocky" portion of the Earth (from the surface down to CMB) is largely composed of magnesium silicates and oxides, often with iron and aluminium impurities.

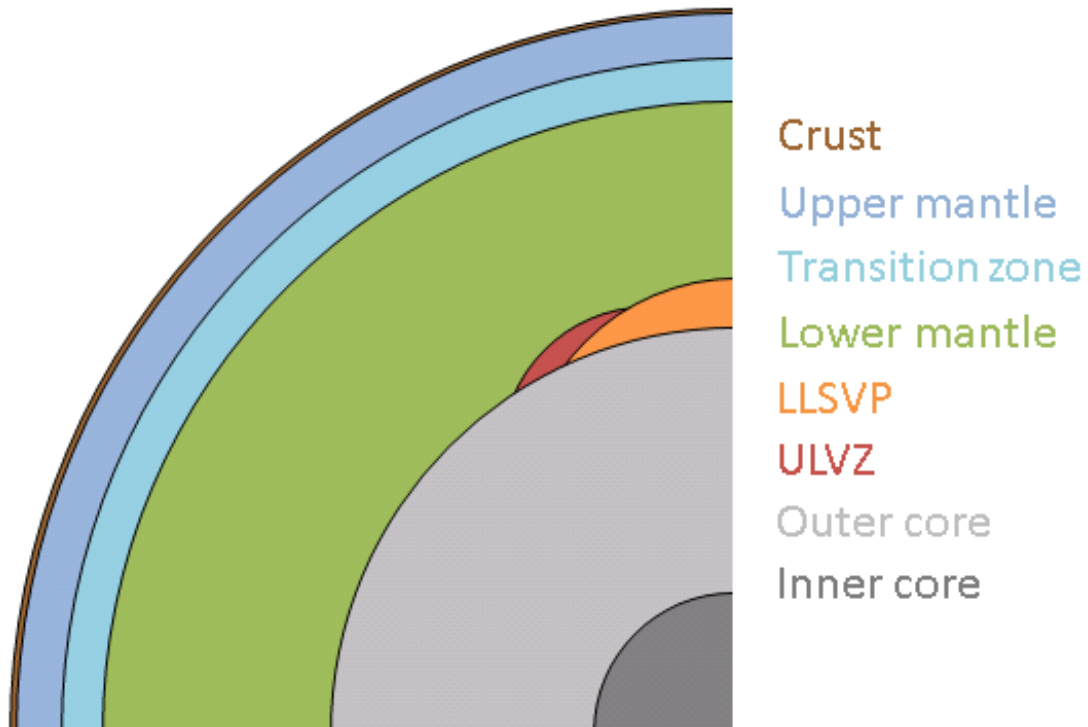


FIGURE 1.1: THE IDEA HERE IS FOR ME TO MAKE A FIGURE THAT INCLUDES ON THE MOST RELEVANT BITS OF THE EARTH, BASED OFF WHAT I MENTION IN FOLLOWING PARAGRAPHS. ADD SCALEBAR/DISTANCES? TEXT ON FIGURE? MARK CMB? MARK ATMOSPHERE/SURFACE?

The two main phase transitions from the Earth's surface to the top of the lower mantle are pyroxene to garnet (40% composition), and olivine through wadsleyite to ringwoodite (60%, see Figure 1.3 Trønnes, 2009). The olivine to wadsleyite phase change occurs at 410 km, marking the top of the mantle transition zone. Wadsleyite transitions to ringwoodite through this zone until 660 km, at which point it breaks down into lower mantle bridgmanite and ferropericlase.

### 1.1.2 Lower mantle

The lower mantle encompasses the region below the mantle transition zone (660 km deep,  $\sim 1900$  K,  $\sim 25$  GPa) to the CMB (2900 km deep,  $\sim 4000$  K, 136 GPa). The mineral proportion of this region is thought to be 75% bridgmanite ( $\text{MgSiO}_3$ , magnesium silicate perovskite), 20% periclase ( $\text{MgO}$ , magnesium oxide), and 5% calcium silicate ( $\text{CaSiO}_3$ ) perovskite (Lee et al., 2004; Trønnes, 2009, see Figure 1.3).

Bridgmanite and periclase are insulators with the potential for the inclusion of

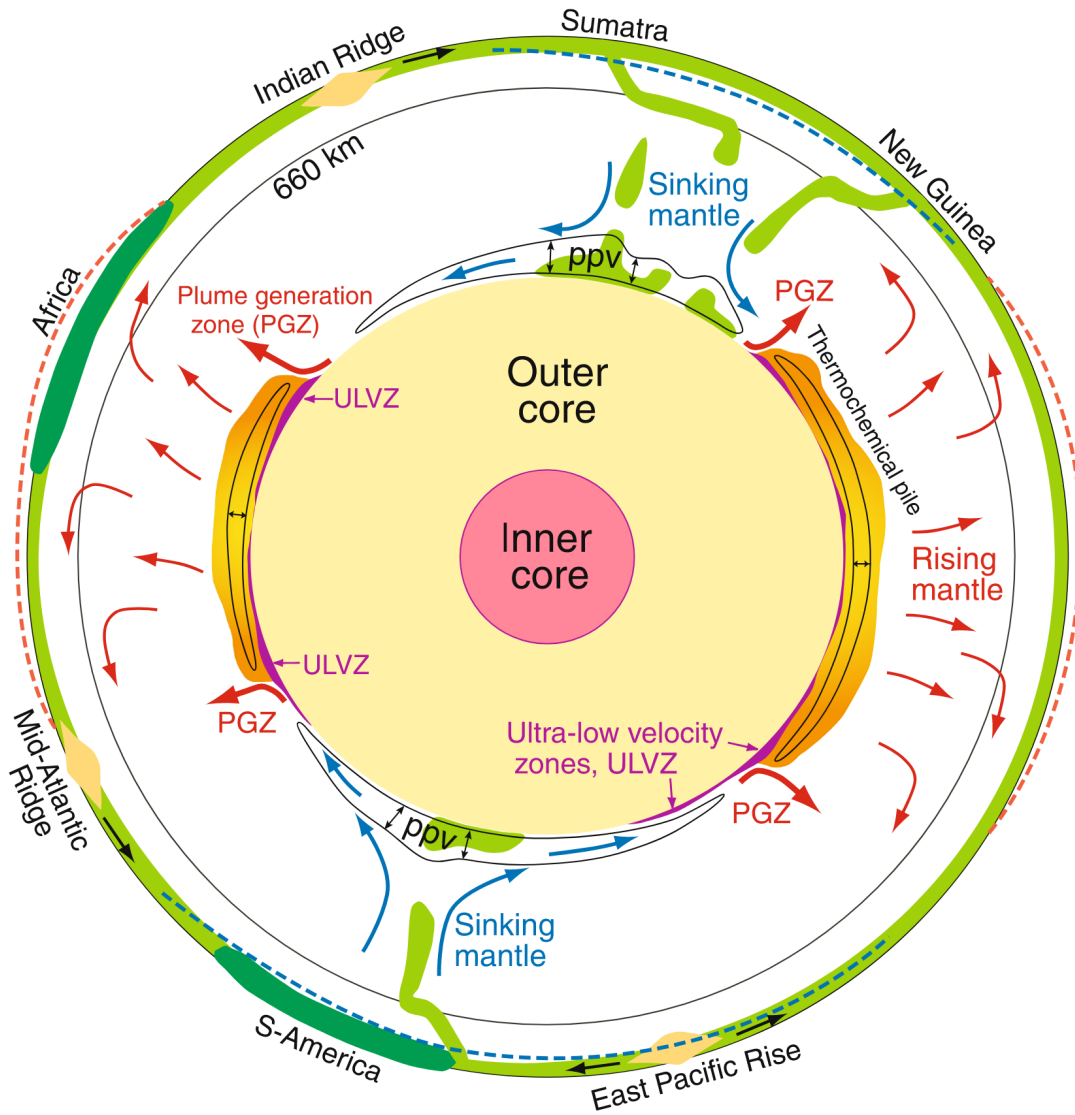


FIGURE 1.2: REPRODUCED WITH PERMISSION FROM TRONNES  
2009

iron impurities (and aluminium in the case of bridgmanite). Ferrous ( $2+$ ) and ferric ( $3+$ ) iron enters the bridgmanite structure, which have varying electron spin states depending on pressure. The concentration of iron is not partitioned evenly between silicates and oxides, with periclase taking a larger proportion than bridgmanite (Muir and Brodholt, 2016). The nature of partitioning changes with composition, where aluminium can enrich  $\text{Fe}^{3+}$  content in bridgmanite (McCammon, 1997), and post-perovskite may behave differently to bridgmanite.

It is widely believed that bridgmanite is stable in the lower mantle until the bottom few 100 km, where it undergoes a pressure-driven phase change to post-perovskite (Murakami et al., 2004; Oganov and Ono, 2004). In places, close proximity

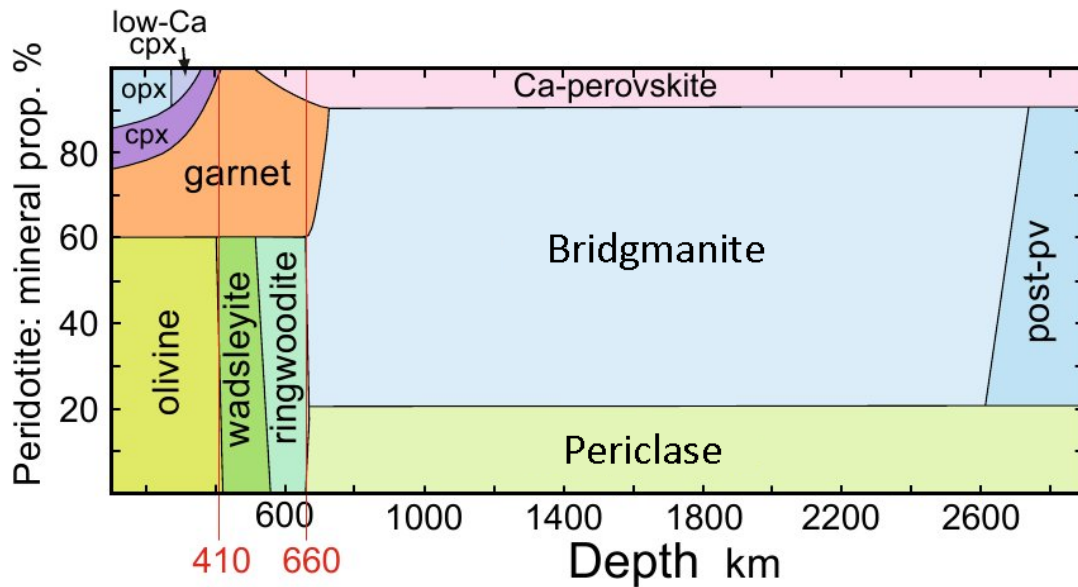


FIGURE 1.3: MODIFIED WITH PERMISSION FROM TRONNES 2009

to the CMB might transform post-perovskite back to perovskite structure due to the increased temperature. This “double crossing” of the bridgmanite stability range can be imaged seismically, where lens-like bands of post-perovskite are shown to pinch out laterally (Lay et al., 2006).

There are two large-scale features on the CMB. Two large low shear velocity provinces (LLSVPs, see Garnero and McNamara, 2008) can be found roughly underneath Africa and the Pacific. They are identified seismically by a  $\sim 3\%$  reduction in shear wave velocity. An associated feature is the ultra-low velocity zones (ULVZs, see Rost et al., 2005), identified around the edges of LLSVPs. These can be observed seismically by a 25% reduction in shear wave velocity, but the reason they exist is unclear. It is suggested they are “thermo-chemical features”, hotter and denser than the regular lower mantle (Garnero and McNamara, 2008). Increasing temperature and density tend to reduce seismic velocity, with increased density to offset the additional buoyancy from raised temperature. “Thermo” intuitively refers to the change in temperatures, while “chemical” changes are required to explain density increase. As a result, thermal conductivity will vary within these regions. Adding impurities such as iron would be a possible cause for density increase, such that the conductivity change should be quantified.



### 1.1.3 Inner and outer core

The region below the CMB (starts at 2900 km depth) is the core, comprised of its outer and inner sections. The liquid outer core extends to 5100 km depth, where the pressure-driven transition to solid inner core occurs. The composition of the core is dominated by iron, with various light elements suggested as possible alloying components (e.g. Allègre et al., 1995; Alfè et al., 2007).

Relative to the lower mantle, the outer core is a vigorously convecting system, and the core-side CMB can be considered to be an isothermal boundary. Heat transfer across the CMB depends on mantle conductivity and temperature. A second issue is possible chemical transfer between core and mantle, where iron from the core would be exchanged with various light mantle elements. Fe-content may increase in the lower mantle with CMB proximity, which in turn could affect conductivity and the temperature profile for CMB heat flux.

## 1.2 Geophysical processes

!!! ADVECT?

Within the lower mantle, thermal conductivity influences the rate at which heat is transferred from core cooling towards the surface, and more importantly the mechanisms by which it does so (Lay et al., 2008). High thermal conductivity systems will preferentially transport heat by conduction. Systems will convect (ADVECT?) where there is too much heat to be transported by conduction alone (i.e. low conductivity conditions).

Observations of plume structures and cyclic subduction patterns (see Garnero and McNamara, 2008) suggest convective behaviour in the lower mantle. Thermal conductivity is poorly constrained in this region, obtaining a comprehensive depth profile is not a trivial task. Additional difficulties are pressure, temperature, and compositional dependences, including isotopic variation (Tang and Dong, 2010; Dalton et al., 2013; Tang et al., 2014) and inclusion of impurities (Manthilake et al., 2011; Ammann et al., 2014; Ohta et al., 2014). Thermal conductivity in the deep Earth influences dynamic processes such as mantle convection and heat loss from the core

(Lay et al., 2008). In this section I will discuss the prominent thermal conductivity-dependent processes.

### 1.2.1 Mantle dynamics

In the lower mantle thermal conductivity changes with pressure, temperature, and composition, influencing features on a large scale. For example, Naliboff and Kellogg (2006) used numerical models of mantle convection to show size and stability of convective plumes are sensitive to thermal conductivity above the core mantle boundary (CMB).

Dubuffet and Yuen (2000) investigated the effects of temperature and pressure-dependent thermal conductivity on mantle convection, finding that depth-dependent thermal conductivity encouraged heat transport via convective plumes. Compared to a constant conductivity model, vertical heat transfer was concentrated to these “pipe-like” structures, despite the horizontally-averaged heat flow for both systems being around the same value. Variable conductivity, even in one dimension, increased the spatial and temporal stability of convection. Plumes were thicker, had heads of larger surface area, and were hotter, compared to the uniform conductivity mantle model.

Tosi et al. (2013) perform two-dimensional numerical simulations of mantle convection with varying compositions and pressure-dependent thermal expansivity and thermal conductivity. Depth-dependent conductivity implemented in models leads to a higher bulk mantle temperature, which then inhibits plume buoyancy and their effect on mantle dynamics. When variable thermal conductivity and expansion are considered together, slabs can be observed to stagnate and move laterally at the transition zone. Changes in mantle behaviour affect the presence of post-perovskite above the CMB, which itself affects the mantle by having a different thermal conductivity to bridgmanite. These outcomes show thermal conductivity is an important property for mantle dynamics simulations to consider, in order to produce “Earth-like” behaviour.

### 1.2.2 Heat flow

The most accessible estimate of the Earth's energy is the total heat flow at the surface, with a value of  $46 \pm 3$  TW is accepted as the upper bound (Lay et al., 2008). Sources of surface heat flow include; radiogenic heating ( $20 \pm 3$  TW), mantle cooling (8–28 TW), and the conduction of heat across the CMB from core cooling. Conductive heat flow is constrained by thermal conductivity, a model of which is not well constrained for realistic mantle compositions.

Better constraints on thermal conductivity are required to estimate CMB heat flow. This in turn would tell us more about the temperatures either side of the CMB, as well as the presence and nature of the lower mantle thermal boundary layer (TBL). Employing the most commonly used value for lower mantle conductivity,  $10 \text{ W m}^{-1} \text{ K}^{-1}$ , heat flow across the CMB is expected to be 5–13 TW (Lay et al., 2008). Both higher and lower values have been proposed, to be discussed in Section 1.6.

### 1.2.3 Geomagnetism

Using shear wave velocity as a proxy for CMB heat flow, Gubbins et al. (2007) showed that variations in mantle temperature gradients above the CMB can influence Earth's geodynamo. The present day magnetic field strength aligns with regions of fast shear wave velocity on the CMB. Ignoring compositional effects in the mantle, seismically-fast regions can be assumed to be cold. Colder regions facilitate larger heat flows through steeper temperature gradients from the isothermal CMB (see Equation 1.1).

Gubbins et al. (2007) recreated the geomagnetic observation of the aforementioned lobes using a core geodynamo simulation, where the upper boundary (CMB, lowermost mantle bottom) condition was a laterally varying heat flux. Knowing the thermal conductivity, especially as it changes with temperature, would better constrain mantle boundary conditions used in this and similar core dynamics models (Ammann et al., 2014).

### 1.3 Defining thermal conductivity

Thermal conductivity is a material property, indicative of the ease with which heat is transferred through conduction. Fourier's law relates heat flux ( $q$ ) through a material to its thermal conductivity ( $\kappa$ ), and the temperature gradient ( $\nabla T$ ) across the body as

$$q = -\kappa \nabla T. \quad (1.1)$$

The transfer of thermal energy can occur between an object and its surroundings, two bodies brought into contact, or along a temperature gradient within an object. The possible mechanisms by which this can occur are conduction, convection, and radiation. Conduction is the transfer of heat by atomic vibrations and electron transport in metallic substances (such as in the outer core, e.g. Pozzo et al., 2012). Convection is the transfer of thermal energy via a moving medium, generally in liquids and gases (but expected in the mantle). Density differences are the driving force for convection, due to the volume change associated with thermal expansion. Radiation refers to the transport of heat by electromagnetic radiation in the form of photons.

I am primarily concerned with lattice conduction through the lower mantle, and secondly the convective behaviour therein. Mantle minerals are expected to be insulators, meaning there is no contribution from electron transport. The radiative component of thermal conductivity in the mantle is thought to be small (Goncharov et al., 2008), and will not be determined as part of this work. In the event that radiation contributes significantly to the effective thermal conductivity (Keppler et al., 2008), it can simply be added to the lattice component.

Convection in the mantle is dependent on thermal conductivity, and will occur if heat cannot be sufficiently transported by conductive processes. The value of the Rayleigh number describes the behaviour of heat flow in a fluid, relative to a critical value for the system. The Rayleigh number related to internal heating in the lower mantle can be expressed as

$$\text{Ra}_H = \frac{g\rho_0^2\beta HD^5}{\eta\alpha\kappa}, \quad (1.2)$$

where  $H$  is radiogenic heat production per unit mass,  $g$  is the acceleration due to gravity,  $\rho_0$  is the reference density,  $\beta$  is the thermal expansion coefficient,  $D$  is the

depth in the mantle,  $\eta$  is dynamic viscosity,  $\alpha$  is the thermal diffusivity, and finally  $\kappa$  is thermal conductivity. While many variables are required to determine the Rayleigh number, most important here is inverse proportionality with thermal conductivity. If the calculated Rayleigh number is lower than the critical value, conduction is the dominant process. When the Rayleigh number is greater, the ratio between it and the critical value describes the vigour and style of convection.

### 1.3.1 Man-made applications considering thermal conductivity

Knowledge of the thermal conductivity of solids is key for a wide range of technological applications, in addition to developing our understanding of natural systems. For known substances thermal conductivity spans about six orders of magnitude, from silica aerogels with  $0.005 \text{ Wm}^{-1}\text{K}^{-1}$  (Lee et al., 1995) to graphene with  $5000 \text{ Wm}^{-1}\text{K}^{-1}$  (Balandin et al., 2008). Conductivity determines whether a material is a conductor or insulator of heat, both of which have many uses, technological or otherwise. Oven gloves introduce an insulating, low conductivity layer between our hands and a hot object which would otherwise cause injury. Vacuum flasks utilise a low conductivity construction to keep liquids hot, houses have wall insulation to keep the heat in. While a saucepan may have an insulating rubber handle, it may also have a conductive copper base, allowing it to heat up quickly with an even temperature distribution.

Heat exchangers are found in many systems, where one substance is used to cool or heat another. While the heat transfer is affected by the thermal conductivity of the media in question, the material that separates the two must have high conductivity for the system to be efficient. Domestic examples include central heating system, fridges, and cars. Industrial examples include solar water heating, and power plants, from geothermal to nuclear.

Thermoelectric materials convert waste heat into electricity, thereby improving the efficiency of domestic, automotive, and industrial processes. They are proposed to increase the sustainability of our current electricity base, but suitable materials must have a low thermal conductivity (Snyder and Toberer, 2008).

## 1.4 Components of thermal conductivity

The transport of heat, rather than the transport of hot material, can be split into three components which contribute to the overall thermal conductivity of a material. These transport mechanisms can be explained on an atomic level, and in the case of this study within a crystal lattice. Atoms have translational symmetry within a crystal, the lattice can be thought of a regular, repeating pattern of atomic arrangement.

### 1.4.1 Electron

Electrical thermal conductivity refers to the transport of heat via free electrons in an atomic structure. Close parallels exist between thermal and electrical conduction. The conduction of thermal energy in metals is predominantly due to the motion and interaction of free electrons. Heat is transferred as electrons move and collide in the lattice. There is no net transport of electrons in order to maintain charge neutrality within the lattice. Lower mantle minerals are insulators, and thus electrical thermal conductivity is of little significance unless very high concentrations of iron minerals exist.

### 1.4.2 Photon

Radiative thermal conductivity is the transport of heat via photons, or packets of electromagnetic energy. Any body with a non-absolute zero temperature emits thermal radiation as light, or photons. Radiative thermal conductivity is determined by a material's optical absorptivity, which describes how heat is transferred by electromagnetic radiation. On the atomic scale, charged particles vibrate and emit light. Energy is transferred from one particle to another when this light is scattered or absorbed. The transfer of heat by radiation is limited similarly to the transfer of visible light, with difficulty passing through opaque media. Unlike lattice conductivity at mantle conditions, radiative conductivity increases with temperature (Hofmeister, 1999). This relation has been used to assume thermal conductivity could be constant through the lower mantle if radiative processes are significant, where the lattice component decreases at the same rate the radiative increases (Tang et al., 2014).

### 1.4.3 Phonon

Phonons are packets of vibrational energy, a quasiparticle used to describe atomic motions which contribute to lattice thermal conductivity (often referred to as just “conductivity” elsewhere in this thesis). As an atom vibrates it exerts a force on its neighbours, where the velocity of the motion is related to heat. Hot atoms in a closed system transfer energy to cold atoms in this way, until energy and temperature are both equilibrated. Considering a crystalline arrangement of atoms, there is long-range structure and well-defined bonds between atoms. Much like standing waves on a string, atoms can vibrate in-phase. These patterns of vibrations are called phonons, and can be differentiated by wavelength and the relative motions of atoms.

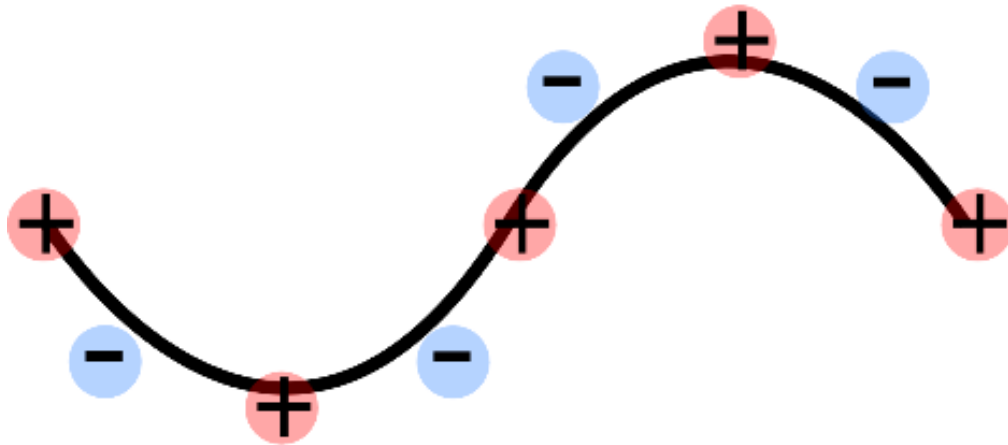
There are two types of phonon, acoustic and optic (see Fig. 1.4). Both types can be longitudinal or transverse, referring to the motion of atoms relative to the direction of energy propagation. Longitudinal means atoms move only in the direction of motion with no perpendicular displacement. Transverse refers to perpendicular displacement of atoms away from the direction of propagation, with no lateral motion along it. The former is like extension/compression of a spring, the latter a standing wave on a string.

Acoustic phonons are propagated by atoms displaced in-phase from their equilibrium positions, generating forces on their neighbours and thus subsequent displacement. Optic phonons are propagated by out of phase motion of adjacent positive and negatively-charged ions (conserving momentum, the lighter atom moves further). This motion is generated from the electric fields of external electromagnetic radiation, and is typically of a higher energy than its acoustic counterpart.

Similar to how photons have wave particle duality (i.e. properties of energy and matter), phonons are known as quasiparticles. This is useful for explaining how phonons waves interact with structural discontinuities and in phonon-phonon collisions. As a particle, a phonon is a quantised packet of vibrational energy. Phonon “particles” move from hot to cold regions, but there is no net motion of atoms within the lattice.

The mean free path (MFP) of a phonon is the average distance it travels before

## Acoustic Mode



## Optic Mode

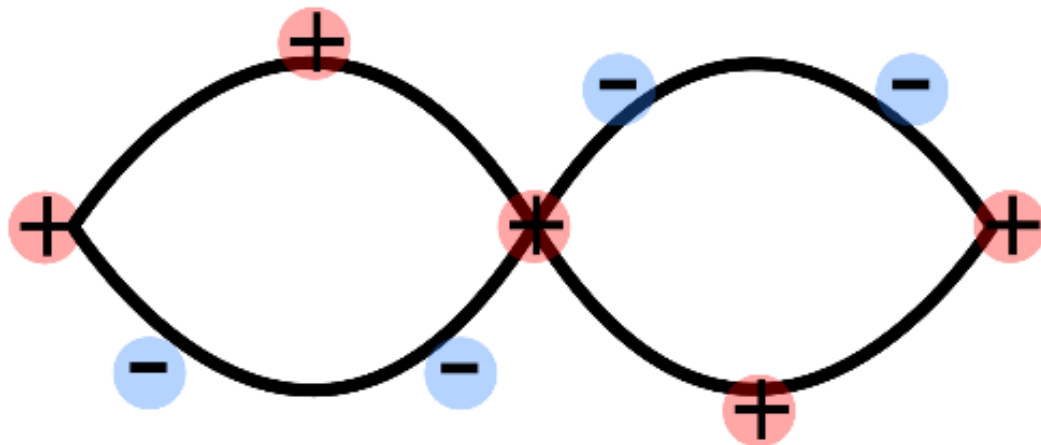


FIGURE 1.4: STOLEN FROM UNI WARWICK  
<https://warwick.ac.uk/fac/sci/physics/current/postgraduate/regs/mpagswarwick/ex5/phonons/>

scattering. The further the longer the MFP, the more efficient the heat transport and thus higher the thermal conductivity. There are several different phonon scattering mechanisms, collisions with (1) other phonons in the lattice, (2) boundaries in the material, and (3) defects in atomic structure. The MFP can be determined via Matthiessen's rule (see Klemens, 1959), which states the total thermal resistivity



(inverse of conductivity) is equal to the sum of individual resistivities,

$$\frac{1}{\kappa} = \frac{1}{\kappa_{\text{ph}}} + \frac{1}{\kappa_{\text{b}}} + \frac{1}{\kappa_{\text{d}}} , \quad (1.3)$$

where **p**honon, **b**oundary, and **d**efect scattering effects are considered. The MFP is proportional to conductivity, thus inversely proportional to resistivity. The shorter the phonon path of a scattering mechanism, the more it influences and contributes to, or detracts from, the MFP. This is apparent in Equation 1.3, where the inverse of the smallest number contributes the most to the sum.

## 1.5 What affects thermal conductivity?

Lattice thermal conductivity can be expressed (e.g. Schelling et al., 2002; Stackhouse et al., 2010) as a simplification of kinetic theory in the form

$$\kappa_{\text{lat}} = \frac{1}{3} C_v v l , \quad (1.4)$$

where  $C_v$  is the volumetric heat capacity,  $v$  is the average acoustic phonon velocity, and  $l$  is the phonon mean free path.

### 1.5.1 Pressure-dependence

The volume of material decreases with increasing pressure, with increasing depth into the Earth. This tends to increase the bulk and shear moduli, causing the seismic wave velocity (Eq. 1.5), and thus the acoustic phonon velocity, to increase.

$$v_p = \sqrt{\frac{K + \frac{4}{3}\mu}{\rho}} , \quad (1.5)$$

where  $v_p$  is the p-wave seismic velocity,  $K$  is the bulk modulus,  $\mu$  is the shear modulus, and  $\rho$  is the density of the medium. Referring back to Equation 1.4, increasing pressure therefore causes a conductivity increase, as the atomic motions become more harmonic.

### 1.5.2 Temperature-dependence

The phonon MFP increases with the volumetric heat capacity, until saturation at a material's Debye temperature (see Figure 1.5). Lattice conductivity is proportional to the MFP (Eq. 1.4), so also increases with temperature up to the Debye limit.

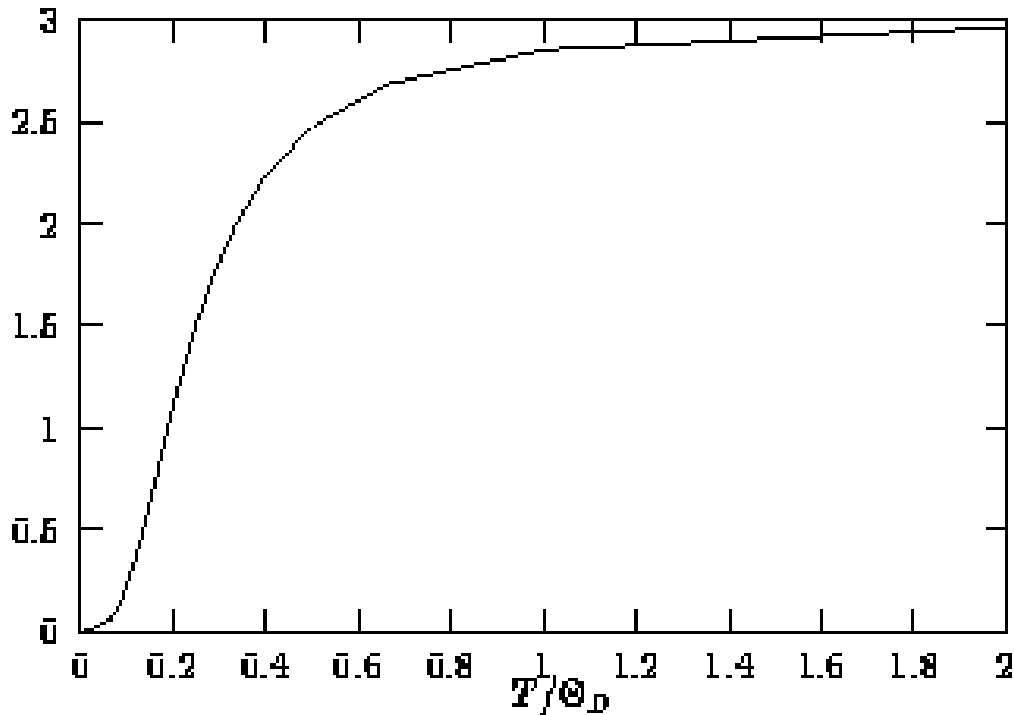


FIGURE 1.5: <http://borisv.lk.net/matsc597c-1997/systems/Lecture4/node4.html>

The effect of phonon-phonon scattering increases with temperature past the Debye temperature. Conductivity change is inversely proportional to temperature at this point, decreasing, and eventually saturating (see Fig. 1.6), to a minimum value as the MFP reaches its minimum (on the order of atomic spacing). While I observe this saturation effect, there is debate within the community whether phonons actually reach a minimum MFP (e.g. Ghaderi et al., 2017). Bridgmanite is above its Debye temperature for all lower mantle conditions I will consider. I can safely assume its conductivity will decrease with rising temperature.

### 1.5.3 Composition

Considering a “pure” material, like  $\text{MgSiO}_3$  bridgmanite, the main source of scattering is phonon-phonon (phonon-boundary scattering exists, but is of small significance). Addition of impurities, such as in  $(\text{Mg,Fe})\text{SiO}_3$  perovskite, introduces

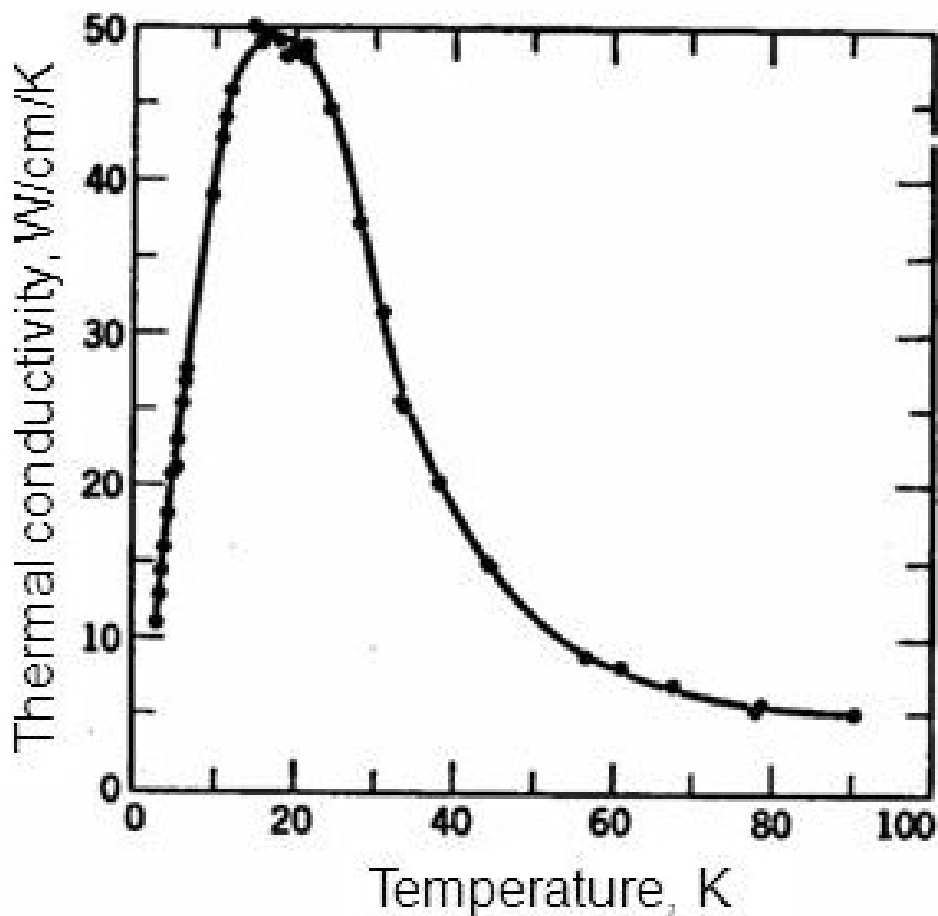


FIGURE 1.6: <https://slideplayer.com/slide/9699097/31/images/29/Thermal+Conductivity+Metals+Dielectrics+Wiedemann-Franz+law%3A.jpg>

phonon-impurity scattering and can reduce conductivity (refer back to Eq. 1.4). The effect of impurities is less significant at high temperatures, when conductivity is already reduced by phonon-phonon scattering. When the phonon-impurity path is much shorter than those of other scattering sources however, impurities can greatly reduce conductivity (via Matthiessen rule, above). Because of these relations, impurities will affect conductivity more higher in the mantle, with the effect reducing towards the CMB. The effect of impurities on thermal conductivity will be discussed extensively in Chapter 4.

## 1.6 Previous work

A range of experimental and atomic-scale simulation methods are available to determine the lattice thermal conductivity of materials. Many studies assume lowermost mantle thermal conductivity to be  $10 \text{ Wm}^{-1}\text{K}^{-1}$  (e.g. Lay et al., 2008), but as discussed later, uncertainty in the extrapolation of experimental results made at low pressures and temperatures gives a range of  $4\text{--}16 \text{ Wm}^{-1}\text{K}^{-1}$  (Brown, 1986; Osako and Ito, 1991; Hofmeister, 1999; Goncharov et al., 2009; Manthilake et al., 2011). Theoretical methods are invaluable for calculating thermal conductivity at conditions which are inaccessible to experiments, i.e. the extreme conditions found in the Earth's lower mantle.

The significance of radiative thermal conductivity, the transport of heat by photonic processes, is an ongoing discussion in terms of the lower mantle (see Section 1.6.3). Until proven otherwise, it is convenient to assume the radiative component is small compared to the lattice component. The components can simply be added to determine the total conductivity (ignoring electrical conductivity), a correction that could be applied to my results at a later date.

Below, I give a review of experimental and computational determinations for thermal conductivity of Earth materials at relevant conditions, where the Direct and Green-Kubo calculation methods are elaborated on in Chapter 2. I focus on determining the conductivity of bridgmanite, as this makes up a much bigger proportion of the lower mantle compared to ferropericlase or Ca-perovskite.

### 1.6.1 Experiments

There have been several experimental studies to measure the lattice thermal conductivity of bridgmanite at CMB conditions. Osako and Ito (1991) measured the lattice thermal conductivity of  $\text{MgSiO}_3$  perovskite, using a modified Ångström method. They investigated a temperature range of  $160\text{--}340 \text{ K}$  at ambient pressure. At  $300 \text{ K}$ , a conductivity of  $5.1 \text{ Wm}^{-1}\text{K}^{-1}$  was obtained. This value is reported by the authors to be consistent with chemical and structural analogues,  $\text{MgSiO}_3$  enstatite ( $5.0 \text{ Wm}^{-1}\text{K}^{-1}$ ,

Horai, 1971) and  $\text{CaTiO}_3$  perovskite ( $4 \text{ Wm}^{-1}\text{K}^{-1}$ , Touloukian et al., 1970). The authors extrapolated the value to mantle conditions via a semi-empirical relation, neglecting the radiative component thermal conductivity. Based on their extrapolation, they predicted a value of  $3.0 \text{ Wm}^{-1}\text{K}^{-1}$  just beneath the mantle transition zone at 1900 K, and  $12.0 \text{ Wm}^{-1}\text{K}^{-1}$  at the top of the  $D''$  layer at 2500 K, a four-fold increase.

Manthilake et al. (2011) measured the thermal conductivity of  $\text{MgSiO}_3$  perovskite at 26 GPa and 473–1073 K, and periclase at 8 and 14 GPa between 373–1273 K. In order to estimate values of thermal conductivity at the top and bottom of  $D''$  for a lower mantle compositional model of 4 perovskite : 1 periclase, the authors extrapolated their measurements to high temperature and pressure. For an iron-free mantle, thermal conductivities of  $18.9 \pm 1.6 \text{ Wm}^{-1}\text{K}^{-1}$  and  $15.4 \pm 1.4 \text{ Wm}^{-1}\text{K}^{-1}$  were estimated for the top of  $D''$  and CMB respectively. Similarly, for a mantle composition with Fe, thermal conductivities of  $9.1 \pm 1.2 \text{ Wm}^{-1}\text{K}^{-1}$  and  $8.4 \pm 1.2 \text{ Wm}^{-1}\text{K}^{-1}$  were calculated for the same regions. This highlights the importance of impurities in controlling thermal conductivity in the lower mantle. The authors mention the inhibiting factor that iron is likely to have on the radiative component of heat transport, and perform their experiments in a manner to reduce the radiative effect.

Ohta et al. (2012) measured the lattice thermal diffusivity of  $\text{MgSiO}_3$  perovskite and post-perovskite at room temperature and pressures up to 144 GPa (using a diamond-anvil cell and light heating thermorefectance). These results suggest a majority perovskite lowermost mantle would have conductivity of  $\sim 11 \text{ Wm}^{-1}\text{K}^{-1}$ , and that parts of the lowermost mantle where post-perovskite is stable will have a conductivity approximately 60% higher. The authors suggest that these differences in conductivity between phases will not have a large effect on CMB heat flux, assuming the double-crossing perovskite phase model. The lattice conductivity of  $\text{MgSiO}_3$  perovskite is shown to increase with pressure and decrease with temperature as expected. The inclusion of impurities is expected to decrease lattice thermal conductivity.

### 1.6.2 Calculations

Haigis et al. (2012) used the Green-Kubo method (refer to REF) to calculate the lattice thermal conductivity of bridgmanite, post-perovskite, and periclase at lower mantle

conditions (ignoring effects of radiative heat transport). Assuming an iron-free composition with four parts bridgmanite to one part periclase, they constructed a model of density and temperature-dependent thermal conductivity along a geotherm. This model suggests great variation over the lower mantle, with a value of  $9.5 \text{ Wm}^{-1}\text{K}^{-1}$  at the top and  $20.5 \text{ Wm}^{-1}\text{K}^{-1}$  above D''. Based on the results of Manthilake et al. (2011), Haigis et al. (2012) suggest the inclusion of iron will lower thermal conductivity by up to half, bringing their result in line with the accepted value of  $10 \text{ Wm}^{-1}\text{K}^{-1}$  (Lay et al., 2006).

Dekura et al. (2013) used *ab initio* anharmonic lattice dynamics with density functional theory (DFT) to calculate the lattice thermal conductivity of bridgmanite. At temperature of 300 K, they found conductivity increases from  $9.8 \text{ Wm}^{-1}\text{K}^{-1}$  at 23.5 GPa to  $43.6 \text{ Wm}^{-1}\text{K}^{-1}$  at 136 GPa. At 100 GPa conductivity decreases from  $28.1 \text{ Wm}^{-1}\text{K}^{-1}$  at 300 K to  $2.3 \text{ Wm}^{-1}\text{K}^{-1}$  at 4000 K. They approximate the effect of radiative conductivity as a function of temperature, and show that total conductivity increases along a typical geotherm, the radiative component being proportional to the increasing temperature and offsetting the decrease in lattice component. From their results they calculated a Rayleigh number ( $Ra$ ) of  $10^5$ – $10^7$  for the mantle, in agreement with the geophysically-expected thermal convection (when  $Ra < 10^3$ – $10^4$ ). These results suggest that a CMB region at 136 GPa and 3200 K will have a conductivity of  $5.3 \text{ Wm}^{-1}\text{K}^{-1}$ .

Ammann et al. (2014) used the direct method, a non-equilibrium molecular dynamics technique, to calculate the lattice thermal conductivity of bridgmanite and post-perovskite under D'' conditions. They found the conductivity of post-perovskite to be around 50% larger than bridgmanite for the same conditions ( $12 \text{ Wm}^{-1}\text{K}^{-1}$  compared to  $8.5 \text{ Wm}^{-1}\text{K}^{-1}$ ). This relation is true even in the TBL, where increases in temperature reduce lattice conductivity for all  $\text{MgSiO}_3$  phases.

Ammann et al. (2014) also investigated the effects of impurities on conductivity, substituting magnesium with iron. The lower mantle distribution of iron is not yet well-understood, specifically the partitioning between bridgmanite, post-perovskite, and periclase. Interestingly, the authors observed saturation in the conductivity reduction associated with atomic impurities, even for small Fe concentrations (see 1.7). Extrapolations of variable-composition experimental results must be

applied carefully, increasing iron content past a certain point will not reduce conductivity any further.

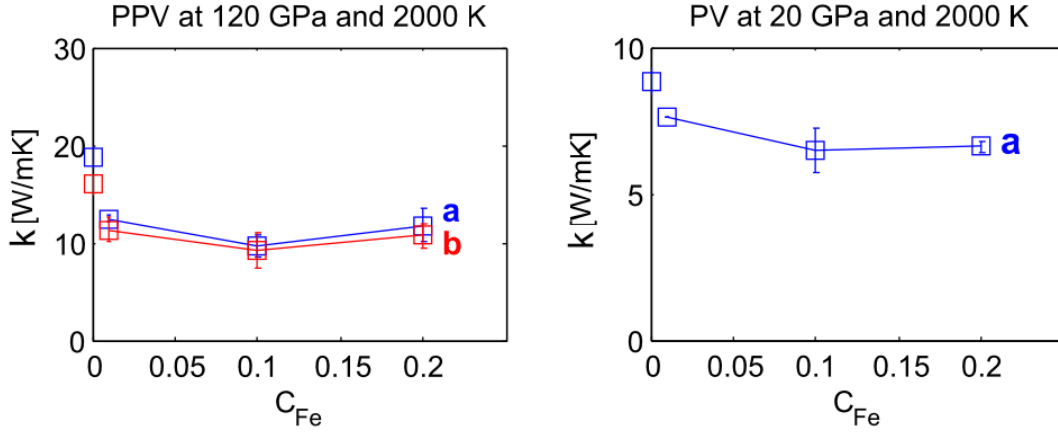


FIGURE 1.7: Thermal conductivity decrease due to inclusion of impurities is shown to saturate with increasing Fe-content, for  $\text{MgSiO}_3$  post-perovskite and perovskite phases. **a** and **b** refer to crystallographic directions along which conductivity was calculated. Figure from Ammann et al. (2014) with permission.

Tang et al. (2014) performed first-principles calculations to assess the thermal conductivity of  $\text{MgSiO}_3$  and the effect of Fe inclusions therein. These results feed into a model of conductivity (including radiative, see Section 1.6.3) along a lower mantle geotherm, of aggregate composition 4 bridgmanite: 1 periclase with 12.5% Fe impurities. Their calculations model  $(\text{Mg,Fe})\text{SiO}_3$  by increasing atomic mass, but not changing the force constants, in a manner similar to Ammann et al. (2014). The inclusion of impurities has little effect at 136 GPa-4000 K, on the order of a few percent, but they note MgO should be affected more considering its higher conductivity. The observation that conductivity is reduced less when it is already small due to the effect of temperature, matches the saturation described in Ammann et al. (2014). Haigis et al. (2012) report conductivity of their aggregate approximately halving however, showing the large uncertainty when extrapolating data especially when considering the (temperature-dependent) effect of impurities.

Ghaderi et al. (2017) investigate the lattice conductivity of bridgmanite using ab initio lattice dynamics calculations, considering a range of pressures at room temperature (mirroring previous experimental measurements).  $\text{MgSiO}_3$  conductivity is found to increase from  $10.7 \text{ Wm}^{-1}\text{K}^{-1}$  at 0 GPa, to  $59.2 \text{ Wm}^{-1}\text{K}^{-1}$  at 100 GPa. Conductivity is extrapolated to lower mantle conditions and determined for a sample

geotherm. The value initially increases with depth as the effect of increasing pressure dominates, until around 400 km above the CMB, where temperature effects take over and conductivity reduces. A value of  $\sim 5.2 \text{ Wm}^{-1}\text{K}^{-1}$  for CMB conditions of 136 GPa and 4000 K.

The concept of a minimum phonon mean free path is discussed by Ghaderi et al. (2017), the idea that a minimum MFP causes conductivity to saturate at high temperatures, showing a dependence different to the expected  $1/T$ . The authors suggest an explanation for this phenomena, which is radiative heat transport. The cause of low MFP is called into question, whether it be small group velocities, or short phonon lifetimes. In any case, the authors assume the minimum MFP to not be correct, and extrapolate to high temperatures with a  $1/T$  relation.

### 1.6.3 Radiative conductivity

Hofmeister (1999) produced a model of thermal conductivity for the entire mantle using data from infrared reflectivity methods. The radiative component at maximum was found to be small compared to the lattice conductivity, between 10–15% depending on the geotherm model used. This corresponds to radiative conductivity values of  $0.67\text{--}0.82 \text{ Wm}^{-1}\text{K}^{-1}$  compared to  $5.8\text{--}6.7 \text{ Wm}^{-1}\text{K}^{-1}$  for the total conductivity at the top of D''.

Keppler et al. (2008) studied the near-infrared and optical absorption spectra of silicate perovskite up to pressures of 125 GPa at room temperature. From both their tests and visual inspection, it was shown that their synthesised perovskite remains transparent at high pressures. Extrapolating their results to high temperatures (4500 K) they suggest that the maximum radiative thermal conductivity above the CMB is around  $10 \text{ Wm}^{-1}\text{K}^{-1}$ , implying that radiative conductivity is likely to be an important component of the total conductivity at lower mantle conditions. The study does not measure the variation of absorption spectra with temperature and pressure, which is currently unfeasible for experiments.

Goncharov et al. (2008) performed a similar optical absorption spectra analysis up to 133 GPa, but reached the opposite conclusion to Keppler et al. (2008). They agreed the radiative conductivity was dependent on the amount, redox state, and



spin state of iron, but disagreed with its significance. Goncharov et al. (2008) estimated radiative conductivity would not exceed  $0.54 \text{ Wm}^{-1}\text{K}^{-1}$  at the top of the D'' layer, a value in line with Hofmeister (1999) but at odds with Keppler et al. (2008).

Tang et al. (2014) re-evaluated the works of Keppler et al. (2008) and Goncharov et al. (2008) to create a profile of radiative conductivity in the lower mantle. Tang et al.'s profile suggests that the previous works have a more reasonable agreement than they show, reducing the order of magnitude difference to a factor of 2 or 3, and a value around  $4 \text{ Wm}^{-1}\text{K}^{-1}$  at CMB conditions. Radiative heat transfer is inhibited in the same way as conductive, by impurities and grain boundaries which are not considered when calculating this upper bound. Unlike lattice thermal conductivity, radiative conductivity increases with temperature, strongly in the mantle thermal boundary layer. When the opposing temperature dependencies of lattice and radiative conductivity are considered together, they suggest that the thermal conductivity of the lower mantle is largely temperature-independent above the D'' region at around  $3 \text{ Wm}^{-1}\text{K}^{-1}$ . Thermal conductivity is found to increase to  $5.5 \text{ Wm}^{-1}\text{K}^{-1}$  in the TBL, due to the increased significance of the radiative component.

More recently, Lobanov et al. (2017) determine the radiative conductivity of post-perovskite ( $1.2 \pm 0.2 \text{ Wm}^{-1}\text{K}^{-1}$ , 10% Fe), bridgmanite ( $2.2 \pm 0.4 \text{ Wm}^{-1}\text{K}^{-1}$ , 10% Fe), and ferropericlase ( $0.2 \pm 0.1 \text{ Wm}^{-1}\text{K}^{-1}$ , 15% Fe) at 130 GPa and  $\sim 3000 \text{ K}$ . They measure optical absorption from diamond anvil cell experiments, extrapolating radiative conductivity from absorption coefficients to lower mantle conditions ( $\sim 130 \text{ GPa}$ ,  $4000 \text{ K}$ ). While the model shows radiative conductivity generally increasing towards the CMB, it decreases from bridgmanite to post-perovskite. Ferropericlase is found to have a lower radiative conductivity than either of the (Mg,Fe)SiO<sub>3</sub> phases, with all of the considered minerals having higher lattice conductivities compared to radiative. The authors conclude that the lattice conductivity will decrease faster than radiative with the inclusion of Fe-impurities, changing the relative significance from low to high Fe content. The results from this study agree with the previous works, that radiative heat transport is not the dominant component in the lower mantle, compared to lattice conductivity, but it cannot be ignored.

TABLE 1.1: THIS TABLE IS NOT UPDATED FOR GHADERI OR LOBANOV. Comparison of previous lower mantle thermal conductivity values.

Paper	Type	Material	Pressure (GPa)	Temp. (K)	Thermal Conductivity ( $\text{Wm}^{-1}\text{K}^{-1}$ )	Notes
Osako and Ito, 1991	Experiment	MgSiO <sub>3</sub> perovskite	0	300	5.1	Measurement, w / analogues  Extrapolation
		MgSiO <sub>3</sub> enstatite	0	300	5.0	
		CaTiO <sub>3</sub> perovskite	0	300	4	
		MgSiO <sub>3</sub> perovskite	24	1900	3	
Manthilake et al., 2011	Experiment	4 MgSiO <sub>3</sub> pv : 1 periclase	127	2500	12	Extrap., mantle model (w / Fe) Extrap., mantle model (no Fe)
			127	2600	$9.1 \pm 1.2$	
			136	4100	$8.4 \pm 1.2$	
			127	2600	$18.9 \pm 1.6$	
Ohta et al., 2012	Experiment	MgSiO <sub>3</sub> perovskite	136	3700	$9.0 \pm 1.6$	Extrapolation
		MgSiO <sub>3</sub> post-perovskite			$16.8 \pm 3.7$	
		4 MgSiO <sub>3</sub> pv : 1 periclase			$11.0 \pm 2.0$	
		4 MgSiO <sub>3</sub> ppv : 1 periclase			$17.8 \pm 3.9$	
Haigis et al., 2012	Green-Kubo Calculation	4 MgSiO <sub>3</sub> pv : 1 periclase	24	2200	9.5	Calculation
		Pv / periclase aggregate	127	2900	20.5	
		Pv / periclase aggregate	136	3739	$16.4 \pm 2.7$	
		Pv / periclase aggregate w / Fe			$16.6 \pm 2.7$	
Dekura et al., 2013	Lattice Dynamics	MgSiO <sub>3</sub> perovskite	Pv / periclase aggregate w / Fe	3200	8.2	Extrapolation, mantle model
			Pv / periclase aggregate w / Fe		8.3	
			23.5	300	9.8	
			136	300	43.6	
Ammann et al., 2014	Direct method	MgSiO <sub>3</sub> perovskite	100	300	28.1	Calculation
			100	300	2.3	
			100	4000	5.3	
			136	3200	5.3	
Tang et al., 2014	Peierls Boltzmann	4 MgSiO <sub>3</sub> pv : 1 periclase	MgSiO <sub>3</sub> perovskite	3739	8.5	Calculation
			MgSiO <sub>3</sub> post-perovskite		12	
			24	2000	2.5	
			127	3000	3.5	
Tang et al., 2014	Peierls Boltzmann	4 MgSiO <sub>3</sub> pv : 1 periclase	136	4000	5.5	Including Fe, with radiative
			136	4000	5.5	

## 1.7 Project summary

### 1.7.1 Aims & objectives

The aim of the work presented in this thesis is to model thermal conductivity at the core mantle boundary (CMB). I will running simulations at high pressure and varying temperatures, considering the effects of composition across an entire solid solution.

By parameterising the temperature and compositional-dependence, thermal conductivity can be determined as a function of both at any condition. In order to perform this parameterisation, I will need to explore the equations that describe these dependencies, adapting them where necessary to compliment my result set.

Working on the atomic-scale, compositional variations are more important than in a sample of bulk material. A relatively low amount of possible sites for impurities to be placed means clumping is possible, and must be considered when randomly substituting atoms.

Fundamental characteristics of heat transport in atomic systems mean that the size of the system / number of atoms affect the magnitude of the conductivity result. Measures exist to quantify these effects, but simulations may yield incorrect results if system size is not considered. I will look into this to validate my calculated results, but also to offer analysis of these finite size effects (FSE) for atomic simulations in general.

### 1.7.2 Thesis outline

In this Chapter, I introduced the concepts surrounding thermal conductivity generally and in the deep earth. A great deal of uncertainty surrounds this parameter at those conditions, which I explore in subsequent chapters.

In Chapter 2, I provide an overview of the methods and expand on issues. I outline my computational approaches, for the non-equilibrium molecular dynamics direct method and equilibrium molecular dynamics Green-Kubo method. I show convergence of computed conductivity with respect to simulation time and physical conditions.

In Chapter 3, I investigate the effect of system size and shape on the converged, computed conductivities. By comparing and contrasting methodologies, I am able to establish the requisite system properties to obtain accurate results at a given condition. This leads me to analyse previous works, and suggest results which may not be correct due to effects of simulation size.

In Chapter 4, I apply my converged computational techniques to investigate the effect of introducing Fe impurities into bridgmanite, and how this affects the resultant conductivity across the entire endmember suite. Furthermore the effect is constrained across multiple lower mantle temperatures, allowing me to create a model of (Mg,Fe)SiO<sub>3</sub> conductivity as a function of temperature.

In Chapter 5, I discuss the temperature and compositional-dependence on heat flow across the CMB, and the effect this has on the whole lower mantle. A review of findings will be presented with suggestions for future work, both in thermal conductivity computations and applications thereof to deep earth studies.

## Chapter 2

# Computing thermal conductivity

In Chapter 1, I introduced the key concepts surrounding this study. I will be investigating the magnitude of thermal conductivity throughout the deep Earth, considering the effect of physical conditions and Fe impurities.

I will be using computation to obtain results, a key part of which is ensuring the simulations behave faithful to the material of interest, and to the physical processes which operate in bulk materials. In this chapter, I introduce the background to calculating conductivity through simulation, and show fundamental system setup and parameter convergence.

The following chapters apply theory introduced here to investigate how conductivity is affected by; system shape and size, and adding impurities to an otherwise regular crystal structure.

## 2.1 Atomic-scale modelling

Knowledge of thermal conductivity is important for modelling the deep earth, but can not be measured experimentally at core mantle boundary conditions. Atomic scale simulations sidestep experimental limitations, but system size must be chosen carefully in order to determine accurate conductivity values.

A range of atomic scale simulation methods are available to determine the lattice thermal conductivity of materials. These are invaluable for calculating thermal conductivity at conditions of which experiments are difficult, e.g. the extreme conditions found in the Earth's lower mantle (pressures and temperatures up to 136 GPa and 4000 K at the core-mantle boundary).

### 2.1.1 Computational regimes

Before you can calculate material properties of interest, you need to determine how the atoms will interact with one another in your system. I do not mean the magnitude of the interactions or the parameters you choose to replicate a material, but the specific theoretical approach of atomic-scale modelling. There are multiple regimes for doing so, a couple of which are described below.

#### Molecular dynamics

In a molecular dynamics (MD) calculation, atoms in a simulation cell have masses, velocities, and forces acting between them. At each computational timestep the net force on each atom is calculated from all the other atoms. Accelerations are then calculated from Newton's second law of motion, which are used to update the velocities and positions of the atoms. The process is repeated, iteratively updating parameters every timestep (see Figure 2.1).

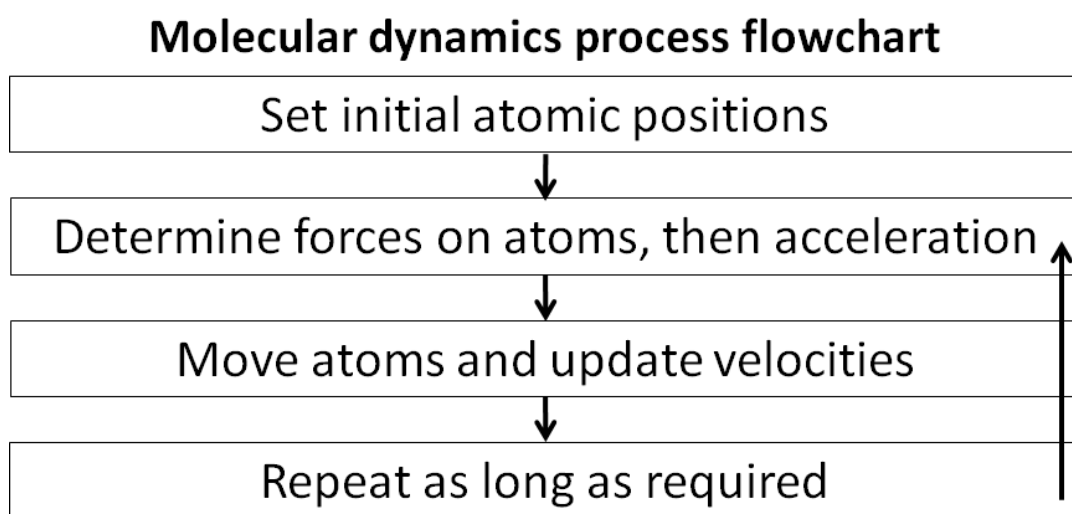


FIGURE 2.1: follow arrows to learn how to MD simplified. DO I EVEN NEED THIS FIGURE?

At zero temperature, a parameter such as unit cell volume will converge, but this is not true when finite temperatures are considered. Temperature fluctuations mean cell volume will constantly change, regardless of simulation length. The solution is to take the cumulative average of a parameter over many timesteps, which converges eventually.

There are 3 styles of molecular dynamics ensemble that I will utilise over the course of this project to perform different kinds of calculations. These are NPT, NVT, and NVE, where N refers to the number of atoms, P to pressure, T to temperature, V to volume, and E to energy. The number of atoms is kept constant in all cases presented here.

In NPT and NVT simulations, the system is thermostatted to a specified temperature. In NPT a barostat is also set, and the cell volume is allowed to equilibrate with the pressure and temperature conditions. This kind of simulation is performed before calculating parameters like thermal conductivity, in order to recreate physical conditions (like the CMB, i.e. 136 GPa, 4000 K). One cannot simply equilibrate the system at high pressure and then run temperature initialisation, this adds the effect of thermal pressure. If this equilibration is performed incorrectly, it is possible to end up with a CMB at 145 GPa for example, ultimately causing conductivity results to be overestimated (as they increase with pressure). When considering temperature while barostatting, thermal pressure will increase system volume accordingly whilst achieving the target pressure.

Once the cell is of a suitable volume for the conditions of interest, the temperature of the system (via the velocities of the atoms) can be initialised through computation in the NVT regime. Freedom to control the initial temperature condition is great for studies where repeatability or gathering a sample of data is important. The structure, conditions, and subsequent computation workflow don't change, but the result will vary in a given distribution from the random nature of atomic velocities and motion. While pressure is free to change, it will remain constant assuming the aforementioned NPT equilibration is performed to obtain a suitable cell volume. Volume can't change, and temperature is thermostatted, so there are no variations in thermal pressure.

Once a reasonable distribution and steady average temperature are obtained, a system can be computed in the NVE ensemble. For both the direct and Green-Kubo methods I utilise, conductivity results are determined in this regime. The kinetic and potential energies of the atoms are held constant, allowing local temperature variations. The same point about variable pressure applies here as well as with NVT, but an overall consistent average temperature means a similarly average pressure.

NVE is used over the similar NVT when calculating parameters, as thermostating can artificially influence the dynamics of the system.

### **Lattice dynamics**

!!! ADD A REFERENCE AND FORGET ABOUT IT? DO I NEED TO SAY WHY I AM NOT USING LD? WHY AM I NOT USING LD!?

An alternative approach to MD is lattice dynamics (LD), where the response of all atoms to the motion of one is considered. Each atom in the simulation cell is perturbed in turn, the motions and response of the other atoms stored in a 3 by 3 tensor for each atom pairing. The tensor takes significant time to compute compared to a single MD timestep, but can be used to calculate various material properties once obtained. The focus of this study will be on MD approaches, but LD results from literature will be reviewed for comparison.

### **2.1.2 Calculating atomic interactions**

Once we have decided on something like MD or LD to run simulations, we need to establish how the atoms will interact with one another in the simulation cell. This means the forces that act between them, how things like atomic separation and charge are considered. There are varying forms of varying complexity available, with multiple parameterisations to describe the interaction. In this next section I present the general ideas, and the specific models applied in my work.

### **Density functional theory**

!!! ANY OTHER ALTERNATIVE APPROACHES THAT NEED TO GO IN AROUND HERE?

Density functional theory (DFT) is a way of determining accurate interatomic forces. The properties of the electrons are considered along with the nuclei, which increases the computational cost and simulation run time. This additionally limits the size of systems, or number of atoms (on the order of thousands), that can be considered. Calculating from first principles in this manner should only be considered if you know the system parameters for converged results, and they can be completed



on a suitable timescale. I will be opting for a different approach, as I wish to investigate a large amount of big systems systems, potentially for multiple compositional variations.

### Classical interatomic potentials

The alternative to DFT is to use empirically-derived potentials to calculate the interatomic forces. Whereas calculating from first principles considers the interactions of atoms and their outer shell electrons, interatomic potentials use an approximation of the electronic potential component (i.e. a classical atomic model).

Systems on the order of millions of atoms can be considered with atomic potentials, due to significantly reduced computational cost compared to DFT. The trade-off is accuracy however, which is controlled by the characteristics of the employed potential. These potentials are set up to reproduce a set of experimental results, but there is no certainty they reflect true values outside their calibrated range of conditions. A realistic model reproduces the structural, elastic, and thermal properties of a material. A common feature of classical potentials is to underestimate the diagonal terms of the elastic constant tensor, and overestimate the off-diagonal, where the discrepancy increases with pressure (Chen et al., 2012).

#### 2.1.3 Finite-size effects

Computational techniques are not hindered by the reproduction of physical conditions like experiments, this does not mean they are without limitations however. Finite-size effects refer to when the number of atoms, or system shape and size, affects the computed result, compared to that of an infinite system. In the case of thermal conductivity, the problem arises when phonons are truncated by boundaries in the simulation cell. As discussed in Chapter 1.4.3, phonons have wave-like properties, including wavelength.

When a simulation cell is shorter than a phonon's wavelength, that phonon cannot be represented in the system. This will mean a calculation is tending to underestimate conductivity, the phonon population is not being fully represented. Another scenario is if the phonon mean free path is longer than the distance between boundaries in a system, in this case phonon scattering behaviour is not being reproduced

accurately. This leads to overestimations, where phonons are able to transport heat unimpeded, and conductivity is strongly dependent on system size (Tadano et al., 2014).

The FSE observed for a material change with thermal conductivity/phonon MFP, and thus are sensitive to pressure, temperature, and composition. Requiring a minimum simulation cell size to recreate phonon behaviour accurately can be a problem when employing DFT calculations, where systems sizes must be kept small to maintain computational efficiency. Testing system size is also a problem, as calculations of large systems must be performed to check convergence of small system results.

### Why use LAMMPS?

LAMMPS (Large-scale Atomic/Molecular Massively Parallel Simulator) is a classical molecular dynamics code (Plimpton, 1995). I will be using it to look at large systems (up to the order of  $10^5$  atoms) and assess how size and shape of the simulation cell affects results. While calculations using interatomic potentials are not as accurate as those using DFT, a main focus of this work will be on the observations of conductivity change between systems of varying size. The  $\text{Wm}^{-1}\text{K}^{-1}$  result isn't as important as confirming phonon behaviour is not being artificially influenced.

While not considered here, the system size parameters I determine for bridgmanite at a range of temperatures and pressures could be used in a DFT calculation. This ensures a DFT calculation would be using a large enough arrangement of atoms, while providing a useful reliability check for my classical results. This of course assumes my determined system is feasible to compute with DFT.

#### 2.1.4 Oganov's bridgmanite potential

The interatomic potential I will be using was developed by Oganov et al. (2000). Many potentials exist for  $\text{MgSiO}_3$  perovskite (REF), but the aforementioned robust up to lower mantle pressures and temperatures. The interatomic potential function includes ionic, covalent, and van der Waals components. The dominant long-range term is the Coulomb interaction, and the short-range interactions are described using a Buckingham potential with the Born-Mayer potential, and a  $C/r^6$  van der

Waals term. The equation for pair-wise potential (summed for potential energy of the system) takes the form

$$V_{ij}^{\text{Buck}} = \frac{1}{4\pi\epsilon_0} \frac{q_i q_j}{r_{ij}} + b_{ij} \exp\left(\frac{-r_{ij}}{\rho_{ij}}\right) - \frac{c_{ij}}{r_{ij}^6}, \quad (2.1)$$

where  $q_i$  and  $q_j$  are the charges of atoms  $i$  and  $j$ ,  $r_{ij}$  is the distance between them,  $b_{ij}$  is the pre-exponential repulsive parameter for the pair,  $\rho_{ij}$  is the repulsion exponent, and  $c_{ij}$  is the van der Waals parameter. There are three sets of these parameters, for each of the interacting atomic pairs (shown in Table 2.1). The charges for Mg, Si, and O atoms are 1.9104, 2.9043, and  $-1.6049$ , respectively.

TABLE 2.1: Parameters used to define Oganov et al. (2000)'s  $\text{MgSiO}_3$  perovskite potential.

Bond $ij$	$b_{ij}$ (eV)	$\rho_{ij}$ (Å)	$c_{ij}$ (eV.Å <sup>6</sup> )
Mg-O	1041.435	0.2866	0
Si-O	1137.028	0.2827	0
O-O	2023.800	0.2674	13.83

## CALIBRATING CUTOFFS

Part of applying classical potentials is setting up the distance over which they act, the maximum separation between two atoms before they are not paired for force calculation. Too small a cut-off distance, and the material is not being replicated faithfully. Too large a cut-off, you are performing more calculations than you need, increasing computation time. The potential between two atoms is inversely proportional to their separation (see Eq. 2.1), “cutting off” in this manner is acceptable when the potential is tending towards zero with increasingly large interatomic distance. I consider two cut-off distances, for both the Coulombic and the Buckingham interactions.

!!! IT MAKES MORE SENSE TO DO BUCK OR COUL FIRST, RATHER THAN ENERGY OR CELL. THE SPLIT FEELS WEIRD - ACBD

I choose to use Buckingham and Coulombic cutoffs of 14 Å and 8 Å respectively. This choice was influenced by other works, and size of the bridgmanite unit cell. As shown in Figure 2.2a. & c., the choice of Coulombic cutoff is of low significance.

Figure 2.2b. & d. show the convergence of both energy and  $a$  with increasing Buckingham cutoff. The difference between a cutoff of 14 Å and higher values is on the picometer scale, we use the former in the interests of computational efficiency.

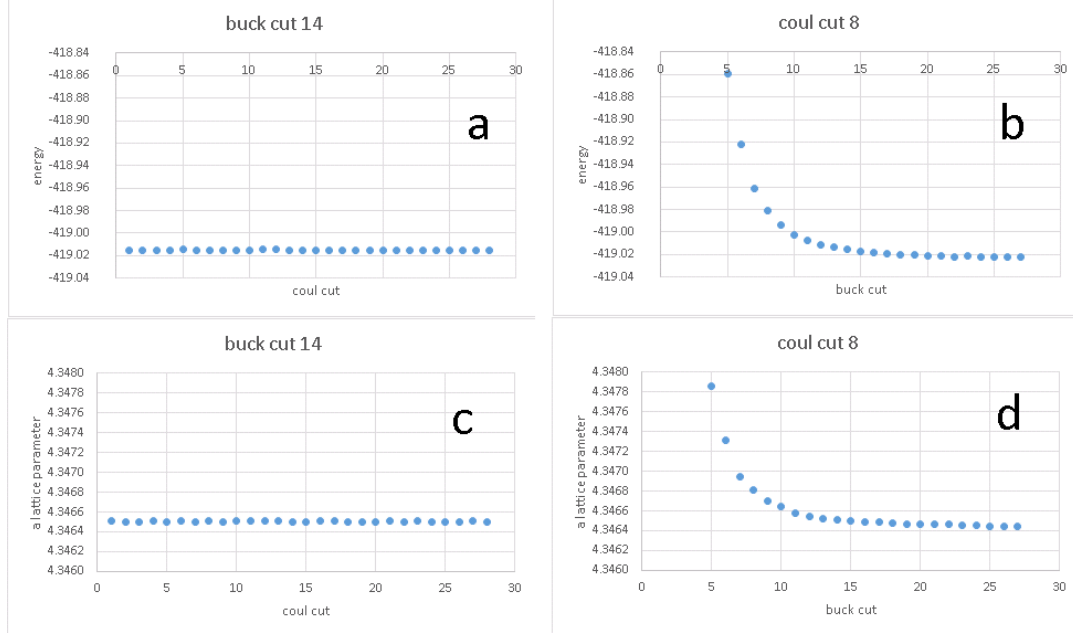


FIGURE 2.2: Top two figures show energy relationship with cutoff, bottom two show lattice parameter  $a$ . Lefthand figures show a Buckingham cutoff of 14 Å, with varying Coulombic cutoff. Righthand figures show the opposite, with Coulombic cutoff of 8 Å. Y-axis set to same scale for both the parameters across the figure. Geometry optimisation formed static at a pressure of 136 GPa.

## COMPARING RESULTS

For my calculations to be valid, I have to be able to reproduce other results calculated using the Oganov et al. (2000) potential in LAMMPS. Oganov et al. provide lattice parameters for a unit cell, along with elastic constants and the bulk and shear moduli. I reproduced their results to acceptable accuracy (see Table 2.2, page 34), using LAMMPS and the lattice dynamics code GULP (Gale, 1997). Of particular note in this table is the agreement of the static LAMMPS and GULP results, showing the potential has been implemented identically for both codes. With regards to the 300 K results, GULP and LAMMPS differ, but only by around 1% for each property. The standard error on the LAMMPS values is smaller than the difference with the GULP values, this disparity is caused by the use of lattice dynamics (LD) opposed to molecular dynamics (MD). The GULP (LD) values are believed to be more accurate

in this case, as 300 K is likely below the Debye temperature for perovskite. Calculations run below this temperature will not accurately recreate the material's thermal properties, due to the inactivity of some phonon modes. This will not be a concern when calculating thermal conductivity, as I will be using temperatures on the order of thousands of Kelvin.

Ammann et al. (2014) used GULP and the Oganov et al. (2000) potential, and provide unit cell lattice parameters for sample lower mantle pressures and temperatures. I reproduced their data to within  $\sim 0.1\%$  (see Table 2.3, page 35), the above mentioned difference between LD and MD reducing at increased temperatures.

TABLE 2.2: Comparison of  $\text{MgSiO}_3$  perovskite properties calculated using the Oganov et al. (2000) potential at 0 GPa

Property	Oganov et al. (Static)	GULP (Static)	LAMMPS (Static)	GULP (LD, 300 K)	LAMMPS (MD, 300 K)
a ( $\text{\AA}$ )	4.7822	4.7875	4.7875	4.8074	4.8022
b ( $\text{\AA}$ )	4.8960	4.9001	4.9002	4.9193	4.9140
c ( $\text{\AA}$ )	6.9322	6.9366	6.9366	6.9598	6.9530
V ( $\text{\AA}^3$ )	162.31	162.73	162.73	164.59	164.08
$C_{11}$ (GPa)	500	507	507	492	487
$C_{22}$ (GPa)	509	519	519	502	498
$C_{33}$ (GPa)	398	411	411	395	395
$C_{12}$ (GPa)	116	125	125	117	116
$C_{13}$ (GPa)	210	209	209	205	201
$C_{23}$ (GPa)	188	192	192	185	184
$C_{44}$ (GPa)	174	177	177	172	170
$C_{55}$ (GPa)	189	189	189	186	184
$C_{66}$ (GPa)	102	108	108	103	102
$K_H$ (GPa)	270.4	276.5	276.5	266.8	269.9
$G_H$ (GPa)	146.3	150.1	150.0	145.2	145.7

a, b, c, and V represent lattice vectors and unit cell volume.  $C_{xx}$  denotes elastic constants.  $K_H$  and  $G_H$  are the Voigt-Reuss-Hill averaged bulk and shear moduli. The MD LAMMPS elastic constants have standard error on the order of 0.1.

TABLE 2.3: Comparison of calculated  $\text{MgSiO}_3$  perovskite unit cell parameters with Ammann et al., 2014

Pressure (GPa)	Value	Lattice parameter ( $\text{\AA}$ ) at a given temperature (K)								
		1000			2000			3000		
		a	b	c	a	b	c	a	b	c
20	My work	4.7281	4.8336	6.8215	4.7701	4.8676	6.8670	4.8220	4.9102	6.9127
	Standard error	0.0001	0.0001	0.0001	0.0001	0.0001	0.0001	0.0006	0.0006	0.0006
	Ammann et al.	4.7281	4.8342	6.8221	4.7708	4.8685	6.8653	4.8293	4.9169	6.9070
	% Difference	0.00	0.01	0.01	0.02	0.02	0.02	0.15	0.14	0.08
130	My work	4.3787	4.5180	6.3290	4.3985	4.5265	6.3495	4.4191	4.5352	6.3706
	Standard error	0.0001	0.0001	0.0001	0.0001	0.0001	0.0001	0.0001	0.0001	0.0001
	Ammann et al.	4.3807	4.5192	6.3236	4.4003	4.5244	6.3438	4.4203	4.5347	6.3691
	% Difference	0.05	0.03	0.08	0.04	0.05	0.09	0.03	0.01	0.02

Data produced using LAMMPS is compared with the GULP results of Ammann et al., 2014, across a range of pressure/temperature conditions. The standard error is calculated from 1E6 timesteps of NVT simulation. The percent difference refers to the variation between my work and Ammann et al.'s.

## 2.2 Computing thermal conductivity

!!! WHAT ELSE NEEDS TO GO HERE? FIXED ENDS? SINUSOIDAL TEMPERATURE PERTURBATION?

I will be using two approaches, both utilising classical interatomic potentials, to calculate thermal conductivity throughout this thesis. They will be explained later in this section, and are as follows,

(1) The non-equilibrium molecular dynamics-based “direct method”, where thermal conductivity is calculated from an imposed heat flux and corresponding temperature gradient via Fourier’s Law (Müller-Plathe, 1997; Nieto-Draghi and Avalos, 2013).

(2) Equilibrium molecular dynamics based on the Green-Kubo relations to determine the thermal conductivity from heat flux fluctuations and their time-dependence (Green, 1954; Kubo, 1957; Kubo, 1966; Schelling et al., 2002).

Stackhouse and Stixrude (2010) review other methods to compute thermal conductivity, including the above, but also

(3) Anharmonic lattice dynamics (Tang and Dong, 2009).

(4) Combined quasiharmonic lattice dynamics and molecular dynamics method (Koker, 2009).

The Green-Kubo and direct method use the same underlying atomic model, but calculate thermal conductivity differently. They have their own unique system setup procedures, data processing work flows, and finite-size effects. In the following sections, each method will be considered individually, before a review of literature comparing the two, and how I will use them to analyse their FSE.

### 2.2.1 Direct method

The direct method is the computational implementation of a typical experiment to measure thermal conductivity, using Fourier’s law to relate heat flux ( $q$ ) and temperature gradient ( $\nabla T$ ) to thermal conductivity ( $\kappa$ )

$$q = -\kappa \nabla T . \quad (2.2)$$



### System setup

In the direct method energy is transferred from one group of atoms to another at regular intervals, creating hot and cold regions between which heat flows (see Figure 2.4.a). This heat transfer process is implemented by taking the velocity of the lowest energy atom in the hot section, and swapping it with the highest energy atom in the cold section (the approach from Müller-Plathe, 1997). The resultant temperature gradient is measured by calculating the temperature of individual groups of atoms along the direction of the heat flux. Thermal conductivity is equal to the ratio of imposed heat flux to the resulting temperature gradient. This can be shown in a rearranged version of Fourier's law

$$k = -\frac{\langle J \rangle}{\langle dT/dx \rangle} , \quad (2.3)$$

where  $k$  is thermal conductivity,  $\langle J \rangle$  is heat flux through a unit cross-sectional area, and  $\langle dT/dx \rangle$  is the temperature gradient between hot and cold regions.

Simulation cells tend to be long relative to their cross-sectional area, defined as height by width (see Figure 2.3). Cell boundaries are periodic and the hot and cold sections are half the cell length apart, meaning heat flows in both directions from hot to cold (one of which is across the length-end periodic boundary). This results in two similar temperature gradients which can be averaged.

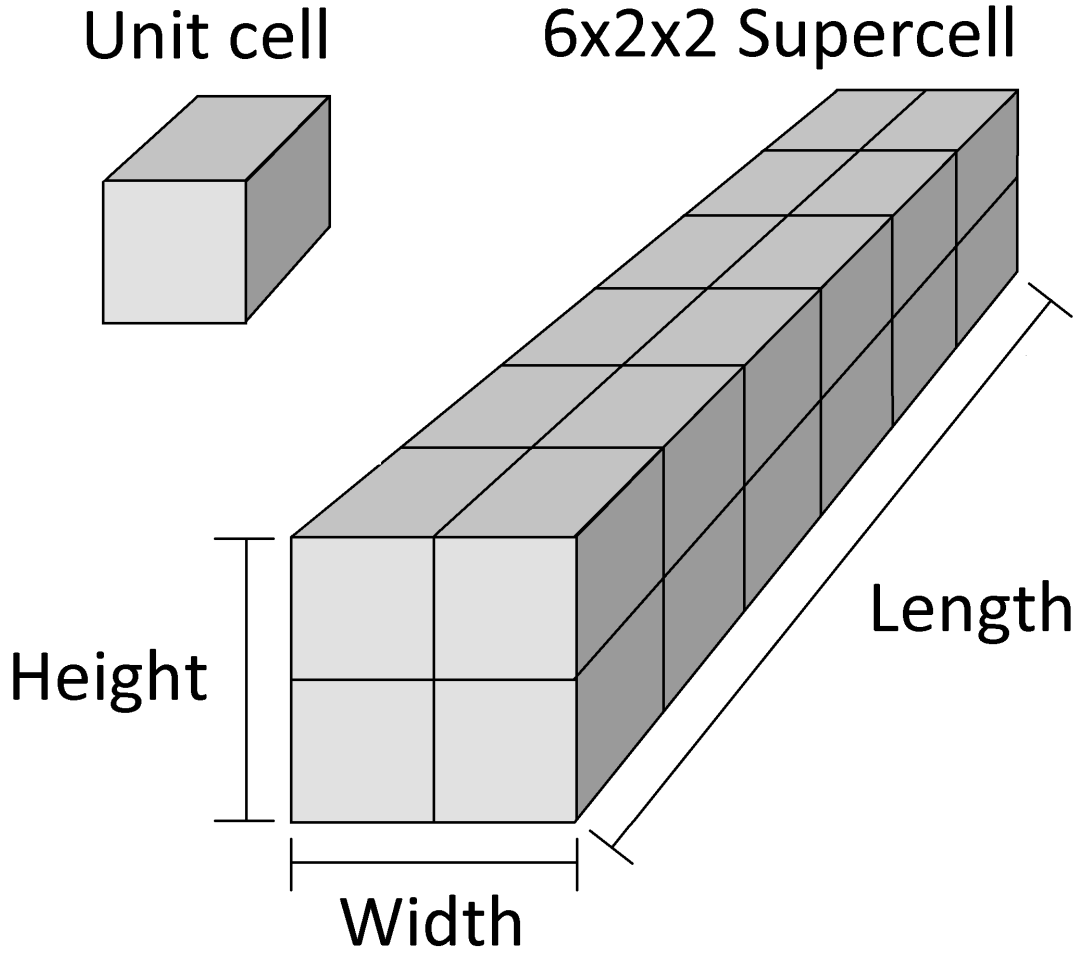


FIGURE 2.3: The unit cell represents the smallest box of atoms that can be replicated to produce a crystal structure. A supercell is an arrangement of unit cells.

### Data processing

In the immediate vicinity of hot and cold regions, the temperature gradient exhibits non-linear behaviour (see Figure 2.4.b) due to the non-Newtonian nature of the heat exchange. Care must be taken to measure the linear portion, which is located roughly in the middle third of the temperature gradient.

The finite size of the simulation cell truncates the mean free path, underestimating conductivity compared to that of the bulk material ( $k_\infty$ ). Using results from simulations of varying cell length ( $L$ ), conductivity is extrapolated to a length-independent value (where  $b$  is a material dependent parameter),

$$k_L^{-1} = bL^{-1} + k_\infty^{-1}. \quad (2.4)$$

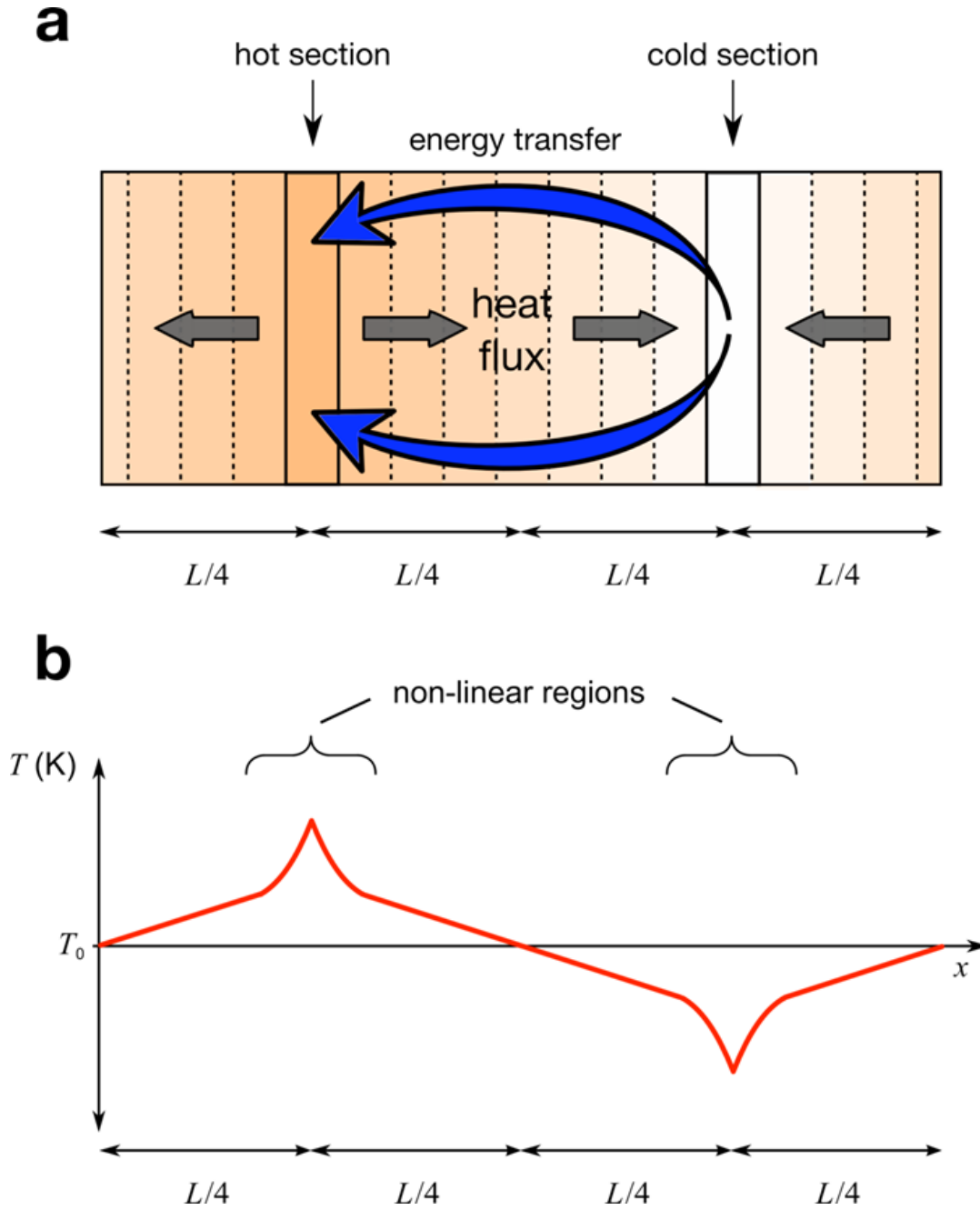


FIGURE 2.4: a. Movement and distribution of heat in the direct method. Orange to white scale represents temperature  
b. Temperature profile along DM simulation cell  
(modified from Stackhouse et al., 2015).

Inverse conductivities from direct method simulations are plotted against corresponding inverse cell lengths. A straight line is fit to the data and extrapolated to the y-axis (at which the inverse cell length equals zero and real length equals infinity), where the intercept gives the inverse of the bulk material conductivity (Schelling et al., 2002).

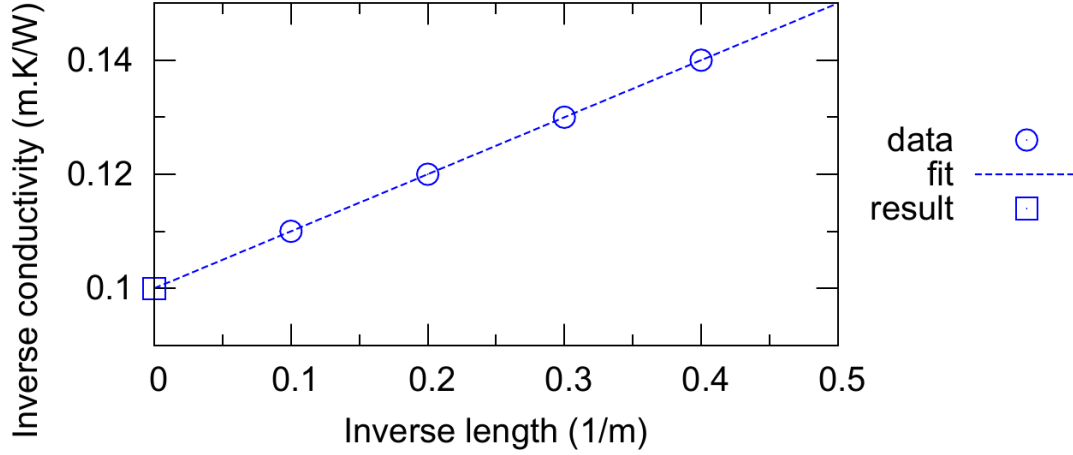


FIGURE 2.5: Idealised example of linear extrapolation procedure. Inverse computed conductivities are plotted against inverse simulation lengths. Extrapolation to y-axis gives conductivity of an infinite system length, i.e. the bulk material.

### Finite-size effects

From kinetic theory [[[REF?]]], conductivities computed by the direct method ( $k_L$ ) are dependent on length of simulation cell,

$$k_L = \frac{1}{3} C_V v l_L, \quad (2.5)$$

where  $C_v$  is the volumetric heat capacity,  $v$  is the average phonon drift velocity, and  $l_L$  is the phonon mean free path.

Problems arise when the data do not support the aforementioned linear trend. There are two effects of finite system size that can cause an individual direct method simulation to diverge away from an inferred/expected linear trend, both of which result in overestimation of the length-dependent conductivity data point. First, when the distance between hot and cold sections (controlled by cell length) is shorter than the MFP, phonons travel ballistically (i.e. without any scattering events) from heat source to sink (Sellan et al., 2010). Conductivities in shorter length cells are overestimated when this occurs, reducing the gradient of the linear fit and thus underestimating the extrapolated conductivity.

For a given length, conductivity is dependent on the CSA, or aspect ratio of the simulation cell. Conductivity is overestimated due to an underestimation of

phonon-phonon scattering, from sparse phonon phase sampling in cells where cross-section is small compared to length. Phonons that aren't resolved cannot contribute to phonon-phonon scattering effects. Reduced scattering means heat transport is artificially more efficient than expected from the bulk material.

### 2.2.2 Green-Kubo

Equilibrium molecular dynamic (EMD) simulations consider systems with constant average temperatures, and a net heat flux of zero. The Green-Kubo method is an example of EMD, looking at heat flux caused by temperature fluctuations. The lattice thermal conductivity of the system is related to the duration of these variations. I will use the Green-Kubo method to compute, but also to validate direct method results and workflow. While the direct method has complex finite-size effects based on length and cross-sectional area, Green-Kubo is simpler in that number of atoms is the main factor. As long as the system is big enough, there is no need to care about arranging the cells or extrapolation procedures.

#### Methodology

The Green-Kubo method uses auto-correlation functions (ACFs) to quantify time-dependence of heat fluxes (shown in Figure 2.6, and Equation 2.6). Instantaneous heat fluxes can be used to determine how energy is dissipated within a system.

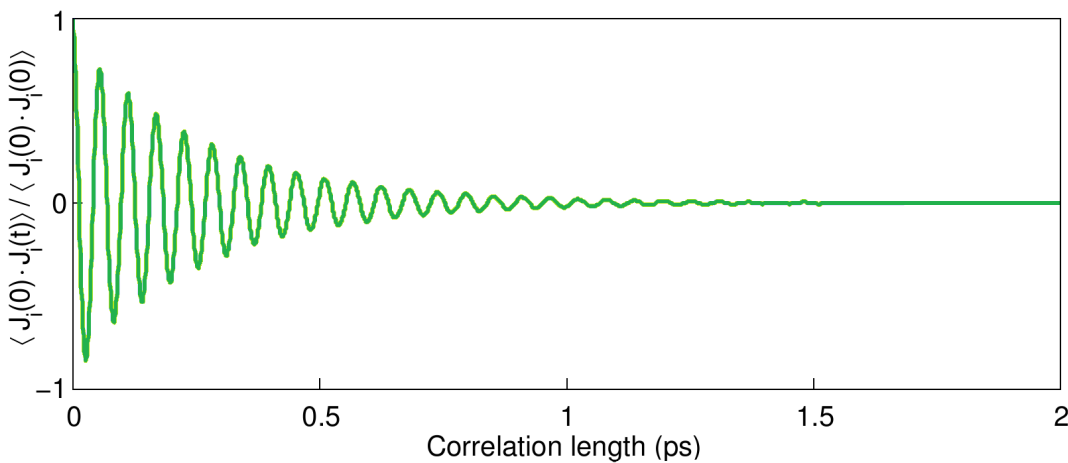


FIGURE 2.6: Normalised ACF. Correlation is taken over a longer length than shown on this plot (100 ps), however the function decays to less than 1% of its initial value at 2 ps. It continues to oscillate about zero, with a positive average value.

The heat flux data required to generate the ACF is obtained from MD simulation in the NVE regime. As always, it is necessary to perform the NPT cell size convergence, and preliminary NVT to populate the atomic velocities.

For a timescale up to a chosen correlation length, the auto-correlation function is obtained over the series of net heat flux in each crystallographic direction

$$ACF_i = \langle J_i(0) \cdot J_i(t) \rangle, \quad (2.6)$$

where  $i$  specifies direction,  $J$  is heat flux, and  $t$  is the correlation length. This acts as a cut-off, the significance of correlating points far apart in time decreases with the separation. The correlation length could be as long as the simulation length, but for large time differences there would be fewer and fewer heat flux pairs. This means there would be increased uncertainty on points of decreasing relevance. The correlation lengths I use are much shorter than the simulation length.

The integral of heat flux ACF is proportional to thermal conductivity via the Green-Kubo equation (see Figure 2.7 and Equation 2.7),

$$\kappa_i = \frac{V}{k_B T^2} \int_0^\infty \langle J_i(0) \cdot J_i(t) \rangle dt, \quad (2.7)$$

where  $V$  is the simulation cell volume,  $k_B$  is the Boltzmann constant, and  $T$  is the average temperature of the system. In this study we use Green-Kubo results as an independent check on the direct method, as they do not have the same finite size-effects. Obtaining a converged conductivity result simply depends on using a large enough cell volume / number of atoms.

### Data processing

The individual integrals obtained from the Green-Kubo show variation from the average combined integral on the order of the mean. Many simulations from different initial temperature conditions are required in order to ensure good sampling of conductivity, as well as ensuring the computation time for each is long enough for convergence. This makes Green-Kubo a computationally expensive method, especially for large systems.

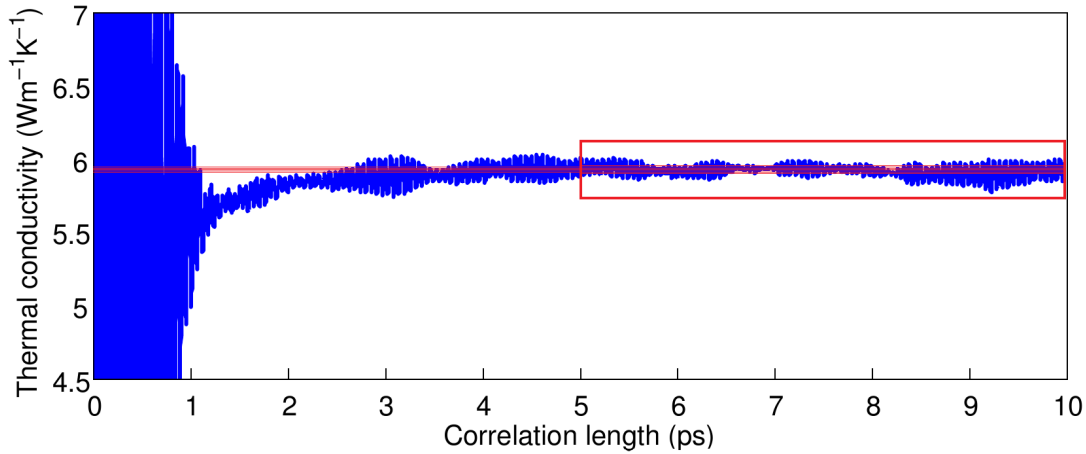


FIGURE 2.7: Integrated ACF, multiplied by constants to get thermal conductivity. Large variation in the first 1 ps corresponds to the correlation time where the ACF is unconverged (still decaying / large oscillations). Thermal conductivity is averaged from correlation time of 5 – 10 ps (region in red box).

From a large sample of integrals, the mean integral is examined to find a time window of convergence. This region exists after the initial large variations, and before any drift behaviour. This correlation window is then applied to all integrals separately, yielding a population of conductivities and uncertainties. I then applied a weighted average to this information, obtaining a conductivity for the entire population.

The ACF should decay to zero as correlation time tends to infinity, however noise in the ACF prevents this. This will ultimately cause the integral to diverge/drift on long timescales. Howell (2012) fits a series of exponential decays to their ACF, forcing the expected decay to zero and subsequent (constant) integral convergence. This represents a significant improvement on the conductivity estimate at long correlation lengths, but is mostly similar with the un-fit integrals early in the correlation.

!!! (STACKHOUSE 2010 REFERENCES Volz and Chen 2000; Sun and Murthy 2006)

## 2.3 Previous work

!!! INSERT TEXT HERE?

### 2.3.1 Method comparison

A wealth of data comparing the conductivities yielded by non-equilibrium and equilibrium molecular dynamics is available for silicon, at temperatures around 1000 K. Schelling et al. (2002) consider Sillinger-Weber silicon, and find good agreement in conductivity results, once FSE are addressed. Sellan et al. (2010) consider the same material and find the two methods don't agree at a lower temperature of 500 K, although it is argued by Howell (2012) that their direct method finite-size scaling was inappropriate. Howell performs their own calculations and review of literature, finding consistent results between the methods and the suite of studies considered. Wang and Ruan (2017) contribute further results consistent with Howell for SW Si at 1000 K, as well showing agreement between methods for graphene and silicene at 300 K.

Dong et al. (2018) show consistency between NEMD and EMD for silicene and Si nanowires. Turney et al. (2009) show very coherent agreements for Lennard-Jones argon across a range of simulation methods, including NEMD, EMD Green-Kubo, along with Boltzmann transport equation and lattice dynamics approaches. None of these studies consider a material as complicated as bridgmanite however, of which I will show the equivalence (or lack thereof) of computed conductivity between the direct and Green-Kubo methods.

### 2.3.2 Bridgmanite FSE

!!! ALSO CONSIDER STACKHOUSE 2015?

As introduced earlier, Ammann et al. (2014) used NEMD to calculate the thermal conductivity of bridgmanite. For conditions of 20 GPa and 2000K, they observe convergence with respect to cross-sectional area (CSA) with dimensions of  $2 \times 2$  unit cells (UC), irrespective of crystallographic direction. They only consider cell lengths up to 32 unit cells however, which means they may be missing the effect underestimated phonon-phonon scattering for a small CSA. Their extrapolation is not incorrect for the results that they have (see their Figure 3), but the gradient can be seen to decrease when  $3 \times 3$  CSA is considered. The computed conductivity of cells over 20 UC decreases as this area increases, possibly due to increased phonon-phonon scattering



effect. I will investigate this further by studying longer systems with larger CSAs.

## 2.4 Conclusion

In this chapter I introduced atomic-scale modelling, how it can be performed, and how atoms can be made to behave like realistic materials. I outline molecular dynamics methodologies for computing thermal conductivity, and potential problems associated with them. In the following chapter I will apply these techniques to study the effects of finite simulation size on computed bridgmanite conductivity result. I will use and compare both of the techniques, as they have independent finite-size effects (FSE).

Once the methodology is checked to have minimized FSE, I will calculate how temperature and composition affect bridgmanite conductivity at CMB conditions. This will feed into calculations of lower mantle heat flux, and how thermo-and/or-chemical piles, the large low shear velocity provinces (LLSVPs), influence lateral variations therein. This will be compared with observed shear wave velocity reductions to offer insight into the extend of LLSVP temperature and chemical heterogeneity.



## Chapter 3

# Examining finite-size effects in thermal conductivity computations

### 3.1 Introduction

!!! EDIT THIS - HOW MUCH OF THIS HAVE I EXPLAINED ALREADY? HOW MUCH IS THAT A PROBLEM?

Knowledge of the thermal conductivity of solids is key in a wide range of technological applications and for our understanding of natural systems. For example, in the Earth's lower mantle thermal conductivity controls the nature of planetary convection (Tosi et al., 2013), and the heat flux out of the core which powers the geotherm. Low thermal conductivities are required in thermoelectric materials, to maximise the efficiency of heat-electricity conversion (Snyder and Toberer, 2008).

A range of atomic scale simulation methods are available to determine the lattice thermal conductivity of materials. These are invaluable for calculating thermal conductivity at conditions of which experiments are difficult, e.g. the extreme conditions found in the Earth's lower mantle (pressures and temperatures up to 136 GPa and 4000 K at the core-mantle boundary).

#### 3.1.1 Finite-size effects

!!! HOW MUCH OF THIS HAVE I EXPLAINED ALREADY? HOW MUCH IS THAT A PROBLEM?

As discussed previously, care must be taken to ensure simulations are faithful to the material and physical conditions. Perhaps most obvious is ensuring you are

representing the chemistry correctly, that the atoms have correct charges, masses, and interactions with neighbours. Even if this chemical information is completely accurate, simulations can produce results wildly different to reality if you do not have enough atoms to reproduce the behaviour of the bulk material. In the case of thermal conductivity, this means ensuring phonons are behaving properly.

Conductivity will be underestimated if the length of the system is comparable to the dominant heat-transporting phonon wavelengths. Phonons that cannot be resolved in the system, cannot contribute to heat flow therein. Another way the effect of finite system size can be observed is in the reproduction, of failure thereof, of thermal resistance. Phonons scatter off of one another, impeding the flow of heat from one point to another. Assuming the above point of having enough length to support phonon wavelengths is considered, phonon-phonon scattering in the direction of heat flow will be accurate. What will not necessarily be correct is the ph-ph scattering in the directions perpendicular. The above principal applies, if the system has too small a cross-sectional area (compared to its length), the phonons involved in lateral scattering cannot be resolved. This tends to reduce thermal resistance within the system, thereby overestimating conductivity.

The severity of these finite-size effects (FSE) increases with the length and expected travel distance of phonons. Longer phonons require longer systems in which to resolve them. This means I want to investigate the conditions at which conductivity will be largest. This means low temperatures, high pressures, and no impurities. While the result of interest is the conductivity at the CMB, 136 GPa and 4000 K, I will also investigate the FSE at 136 GPa and 1000 K, both considering chemically and isotopically pure  $\text{MgSiO}_3$  bridgmanite.

## 3.2 Green-Kubo

Here I will outline my approach for applying the Green-Kubo method for computing conductivity to bridgmanite at lower mantle conditions. First I show accurate results can be obtained within the chosen correlation length. I then show how results represent a large sample of possible conditions, and a way of minimising error by combining multiple heat flux autocorrelation functions (ACFs). Finally I show

that all these components are valid with respect to total simulation time, before presenting how finite simulation size affects conductivity results.

After determining cell parameters appropriate to the simulated conditions (NPT), I initialise a temperature distribution (NVT). To obtain heat flux auto-correlation functions, a simulation for each initial temperature condition is run for  $X$  ns, with 9 successive repeats for a total of 10 jobs. This gives 10 ACFs from each initial condition. Simulation runs are split in this manner to be feasible computationally, jobs submitted to the high-performance computing facilities have a maximum length of 48 hours. Each job finished in this manner produces an ACF, somewhat of a bootstrapping process on the total simulation series.

### 3.2.1 Correlation length convergence

I compute ACFs up to correlation lengths of 100 ps, with (100,000) 1 fs timesteps. This length is longer than required but selected as a proof of concept to show convergence in the conductivity result, additionally to display the extent and behaviour of drift in the integrals for long correlation times. Figure 2.6 shows that the magnitude of the ACF decays to much less than 1% of its initial value around a correlation time of 2 ps, inferring the start of convergence for the integral and thus conductivity.

Considering bridgmanite at lower mantle pressures, I find correlation time window extrema of 2-30 ps to be suitable. At the low-end, this allows the initial high-variability in integral value to be ignored. At the high-end, the time is long enough for good sampling of the integral, but short enough to ignore the drift-effects. The magnitude and range of the window typically increases with conductivity (or with decreasing temperature etc.), e.g. 2-10 ps at 3000 K (Figure 3.1b), and 10-30 ps at 1000 K (Figure 3.2b). These correlation lengths are on the same order of magnitude as used by Haigis et al. (2012). They observe convergence in MgO conductivity results after 30 ps, albeit at a temperature of 300 K.

As shown in Figure 3.1c & 3.2c, the integral drifts considerably outside of the chosen correlation window. This effect needs to be resolved before accurate conductivity results can be determined, and is caused by an increase in the ACF signal to

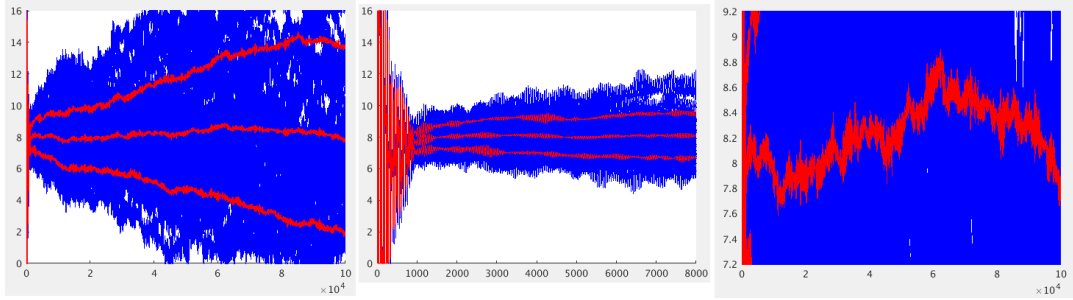


FIGURE 3.1: Integral populations (blue) from GK calculation at 3000 K, with mean integral and plus/minus standard deviation (red). **a.** shows the range of conductivity series over the full correlation length. **b.** shows the series up to the end of the correlation window (8 ps, the window starts at 2 ps). **c.** focuses on the mean integral over all the correlation length, past the correlation window where it begins to drift away from a converged value.

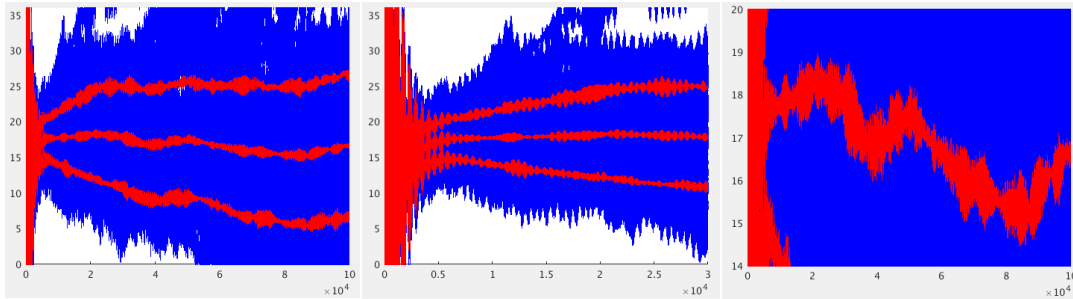


FIGURE 3.2: Integral populations (blue) from GK calculation at 1000 K, with mean integral and plus/minus standard deviation (red). **a.** shows the range of conductivity series over the full correlation length. **b.** shows the series up to the end of the correlation window (30 ps, the window starts at 10 ps). **c.** focuses on the mean integral over all the correlation length, past the correlation window where it begins to drift away from a converged value.

noise ratio at long correlation lengths. Theoretically, the ACF tends to zero as correlation length tends to infinity. In practice this doesn't happen because of noise, but it can be thought of as the signal tending to zero and the noise remaining finite.

### 3.2.2 Integral sample convergence

!!! IS THIS SECTION EVEN NECESSARY?

ACFs produced by each simulation are integrated separately, and averaged into a single series. From this combined integral I pick a window of correlation lengths to capture a flat, converged region (or the section just after the 'bottleneck' if convergence is not obvious). This correlation length window is then applied to all integrals constituent to the combined series, giving a sample of integral averages and corresponding standard deviations. A weighted average is then taken of these data points, to give a single value with uncertainty. This value is directly proportional to thermal conductivity, as given by Equation 2.7. REFERENCING TOO FAR BACK? REPEAT EQUATION?

!!!SHOULD I BOOTSTRAP THE INTEGRALS, HOPEFULLY SHOW THAT THE RESULT DOESNT CHANGE?

### 3.2.3 Simulation length convergence

!!! NO ONE HAS EVER READ THIS SECTION, TRIPLE CHECK!

The number of integrals and their correlation length is ultimately more important than the simulation length the integrals were derived from. This is of course assuming individual simulation length is much longer than the required correlation length window maximum.

In this example I use an individual simulation length of 10 ns (for 289 runs) with up to 100 ps correlation length, i.e. simulation 100 times longer than correlation. Converged conductivity can be obtained from windows ranging between 5–10 ps, so it will this 10 ps that the simulation length must be longer than. I reprocess the ACFs in such a way that the individual simulation time is reduced, reducing the effective simulation time but not the number of integrals averaged.

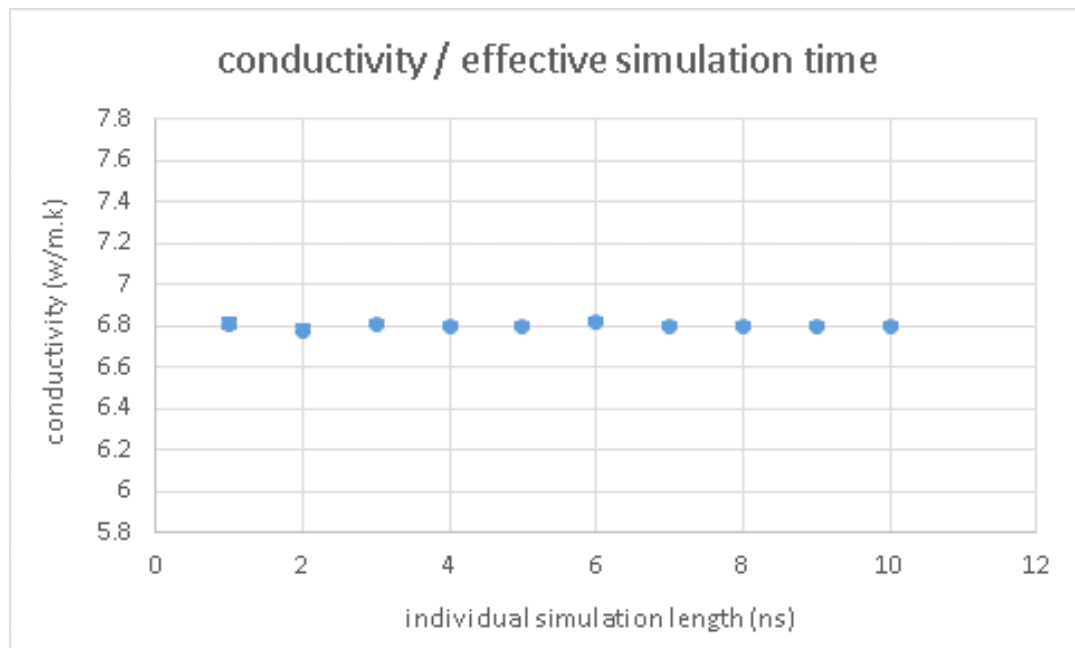


FIGURE 3.3

Figure 3.3 shows little variability in conductivity result average from the 5–10 ps window, when individual simulation length to obtain each integral changes from 1 to 10 ns. The variation is  $\pm 0.02$  on an average of  $6.80 \text{ Wm}^{-1}\text{K}^{-1}$ .

While statistics show the conductivity is converged, it does not mean the integral set is the same. The Figure 3.4.a corresponds to individual simulation length of 1 ns (the leftmost data point on Figure 3.3), and 3.4.b 10 ns (the rightmost point).



Increasing simulation length means the individual integrals converge on the mean, reducing the spread and standard deviation. Negative conductivities can be seen on 3.4.a, which is obviously unphysical, reinforcing the idea that averaging a large enough sample of integrals is more important than the simulation time that went into producing a single series.

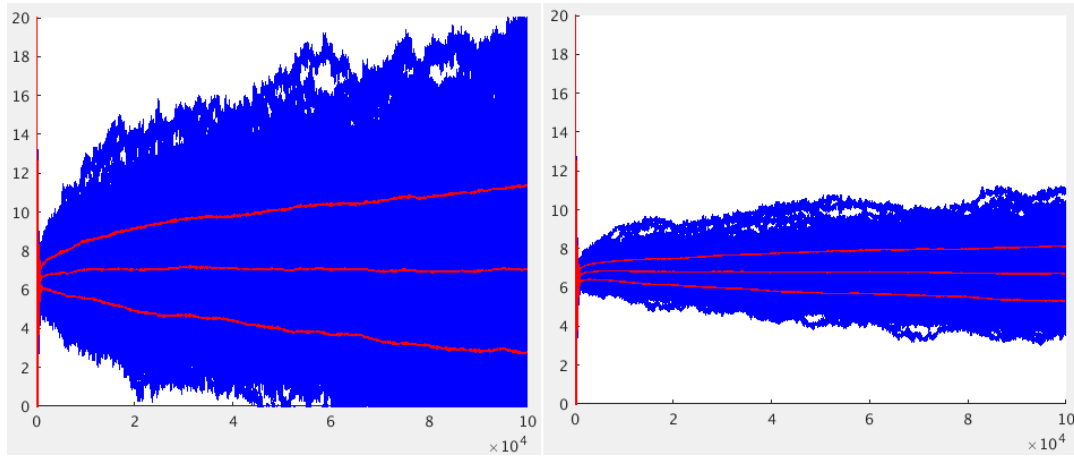


FIGURE 3.4

### 3.2.4 Finite-size effect convergence

The bridgmanite unit cell is orthorhombic (i.e.  $a:b:c = 1:1:1.4$ ), so I assemble supercell structures of  $3 \times 3 \times 2$ ,  $4 \times 4 \times 3$ ,  $5 \times 5 \times 4$ , and  $6 \times 6 \times 4$  to make a supercell arrangement approximating a cube. These supercells house 360, 960, 2000, and 2880 atoms respectively (20 atoms in unit cell). The goal here was to keep the height to area ratio as small as possible in each direction, while increasing the atom count.

The supercell arrangement of  $3 \times 3 \times 2$  fails to reproduce conductivities on the same order as the larger cells for both temperatures (see Figures 3.5 & 3.6. The conductivity obtained from the  $4 \times 4 \times 3$  supercell is in good agreement with the larger cells. This is a useful result in terms of computation efficiency, as  $6 \times 6 \times 4$  supercells are 3 times as large as  $4 \times 4 \times 3$ .

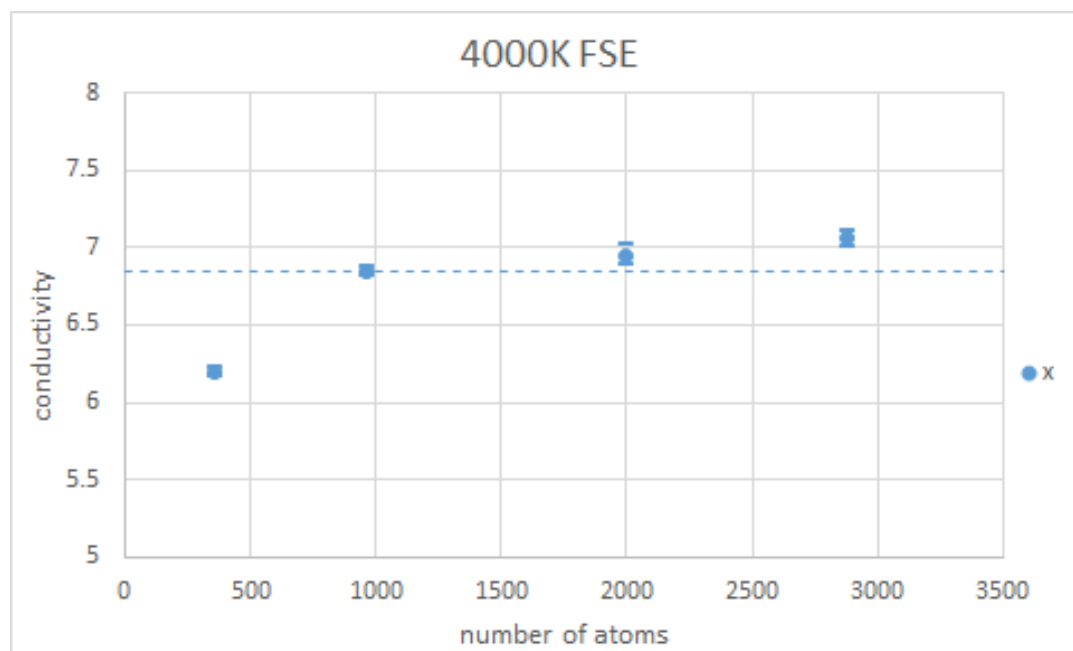


FIGURE 3.5

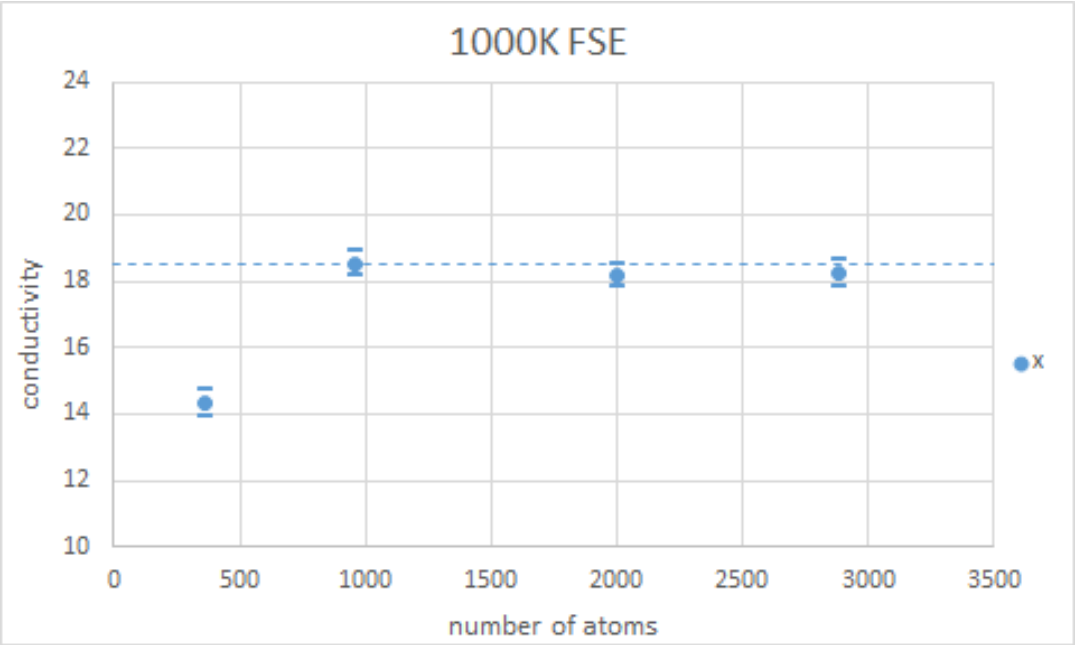


FIGURE 3.6

!!! MOVE TO APPENDIX? - The following lists of simulations were performed to obtain the results displayed in the 1000 K and 4000 K finite-size effect plots.

TABLE 3.1: 4000 K

Supercell	Simulation length	# initial conditions	Total run time	
3x3x2	10 ns	20	2 $\mu$ s	
4x4x3	10 ns	30	3 $\mu$ s	
5x5x4	5 ns	20	1 $\mu$ s	1.7 $\mu$ s
	1 ns	70	0.7 $\mu$ s	
6x6x4	1 ns	80	0.8 $\mu$ s	

TABLE 3.2: 1000 K

Supercell	Simulation length	# initial conditions	Total run time
3x3x2	1 ns	20	0.2 $\mu$ s
4x4x3	1 ns	50	0.5 $\mu$ s
5x5x4	1 ns	50	0.5 $\mu$ s
6x6x4	1 ns	50	0.5 $\mu$ s

### 3.3 Direct method

In this section I will talk specifically about how I apply the direct method to compute the thermal conductivity of bridgmanite. I cover the initial system setup, the supercell geometry and how the system is divided into sections to determine the temperature gradient. I then cover properties which must be monitored to ensure accurate results, namely the magnitude of the temperature difference across the gradient, and the convergence of computed conductivity with total simulation time. I briefly introduce the data processing methodology, before explaining how the effects of finite system size are considered and mitigated. Finally I correlate my observed results with theoretical predictions, and discuss the required system size to compute the conductivity of bridgmanite at lower mantle conditions.

!!! FLOW CHART, OVERVIEW FIGURE OF BELOW STEPS AND PROCESS?

#### 3.3.1 Setting up supercells

In order to investigate how FSE can affect direct method results, I plan to use very large cells, both in length and cross sectional area. I will use supercells up to 96 unit cells long in the x-direction of heat flow (specifically 6, 8, 10, 12, 16, 24, 48, and 96 unit cells long). Perpendicular to this length, I will use supercells with a cross section up to  $12 \times 12$  unit cells ( $1 \times 1$ ,  $2 \times 1$ ,  $2 \times 2$ ,  $4 \times 4$ ,  $8 \times 8$ , and  $12 \times 12$ ).

The simulation supercell is split into sections along its length, where the average temperature of atoms within is determined to calculate the gradient across the system. The symmetry of the bridgmanite crystal system allows unit cells to be divided into two, such that the width of sections is half a unit cell along the length of the supercell (the direction of heat flow).

Two of these sections, half the supercell length apart, are designated as the heat source and heat sink. It is within these sections that the energy of the atoms is swapped. Heat flows in both directions from the hot section because of cell periodicity (refer back to Section 2.2.1), meaning there are two temperature gradients to sample and combine.

Where  $L$  is supercell length in unit cells and  $S (= 2L)$  gives the number of sections, there are  $S/2 + 1$  temperature points to fit the gradient to. Width of a section,  $S_W$ , is

half that of a single unit cell. Because the temperature gradient is non-linear around the heat source and sink, I ignore  $S/12$  sections (rounded to nearest integer) from both ends of the temperature gradient. For a given simulation cell,  $S/3 + 1$  points are used to fit the temperature gradient. The minimum supercell length considered is 6 unit cells (12 sections, 5 data points for fitting), in order for sufficient sampling of the temperature gradient.

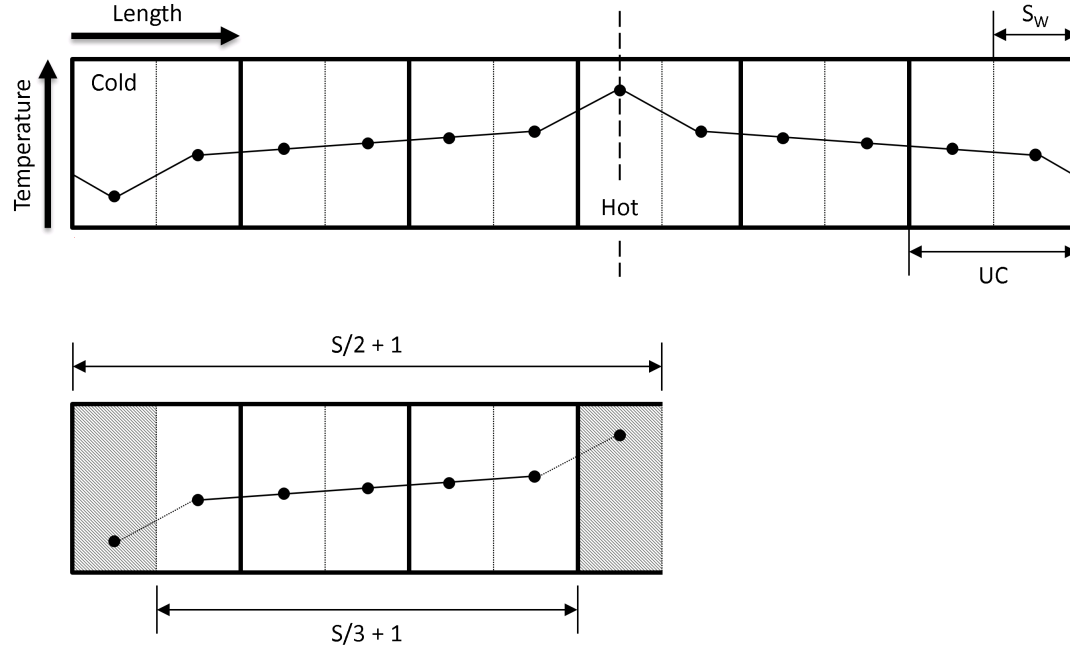


FIGURE 3.7: Temperature profile and geometry schematic for a cell 6 unit cells long. The temperature profile is non-linear, steeper gradient than the surrounding, immediately around the heated sections. In longer cells, the non-linear region will be wider than one section, requiring more sections to be ignored. The temperature profile is folded over onto itself to average one temperature gradient. The equations discussed hold as long as a unit cell is divided into two sections, and a twelfth of the total sections are removed from each end of the combined gradient.

### 3.3.2 FIDDLING WITH BIN WIDTH

Changing the width of the heated sections has no effect on the conductivity result, assuming you have enough temperature points to fit the linear gradient. Furthermore, changing the width (and thus number) of temperature bins has no effect on the sampled gradient, assuming resolution is large enough to capture the non-linear region around the heat source/sink (see Figure ??).

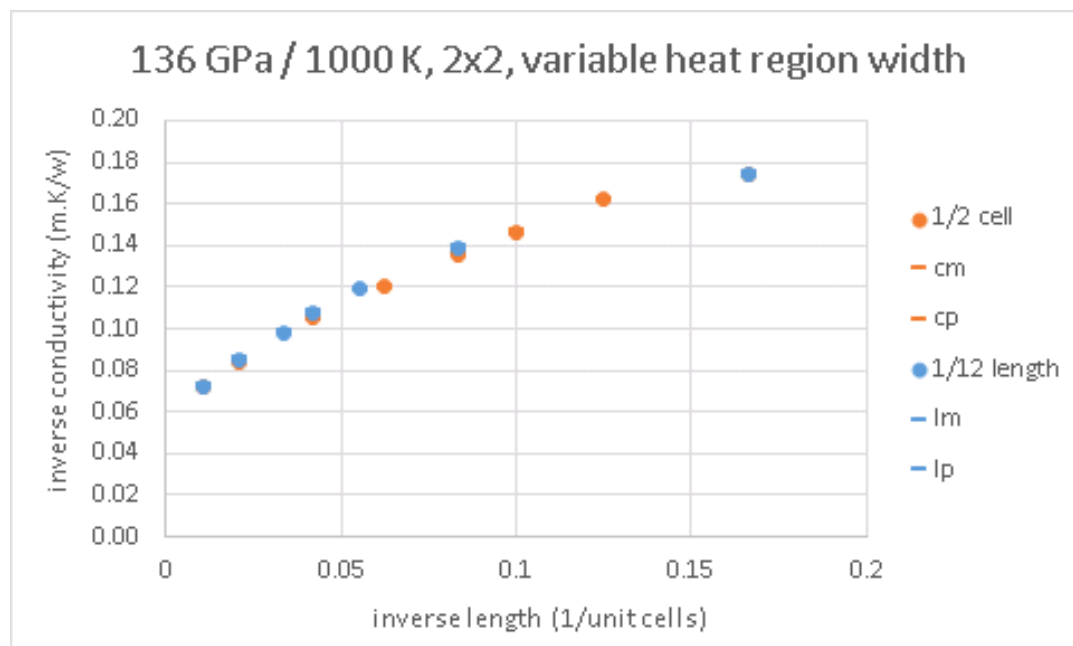


FIGURE 3.8: Conductivity results from direct method when temperature is calculated from sections half a unit cell wide, and also a twelfth of the total length. The amount of points in the temperature gradient changes when the section width depends on the unit cell, but not on the length (i.e. there are always twelve sections, the gradient is fit to five data points).

### 3.3.3 Temperature gradient convergence

An important factor for utilising the direct method is maintaining a sensible temperature gradient, such that Fourier's law (REF) remains valid, i.e. conductivity is constant along the length of the cell. Thermal conductivity is strongly temperature-dependent at upper lower-mantle conditions (1000 K), it is therefore undesirable to have substantially different conductivities as a function of temperature across the cell. The opposite case is also true, the difference in temperature between hot and cold sections must be larger than the uncertainty in the average system temperature.

As a general rule, I try to keep the temperature difference between the ends of the gradient to 20% the mean temperature. I control the magnitude of the gradient by altering the interval at which heat is exchanged, via swapping atomic velocities in the hot and cold sections (see Section 2.2.1). To produce the desired gradient magnitude as outlined above, shorter intervals are required as cell length decreases, cross-sectional area increases, and system equilibrium temperature decreases. The easier it is for heat to flow from hot to cold (smaller distance between, more area for heat transport, lower temperature/less thermal resistance), the more heat must be transported (in the form of shorter intervals between heat swaps) to maintain a temperature gradient.

### 3.3.4 Simulation time convergence

Initial results from the direct method show a large variability in conductivity, despite the separate temperature equilibration performed beforehand. This is related to the setup of the temperature gradient and its transition to steady behaviour. For this reason, the timesteps containing this behaviour are ignored when determining conductivity. This simply means removing the temperature gradient and heat flow data from the rest of the series. How this is applied varies in practice, but on a 1 ns simulation, I would typically ignore the first 100 ps (10% simulation time).

After removing the first portion of the data there is still variability in the calculated conductivity, but this typically converges quickly over the course of the simulation. If you have enough timesteps, the cumulative average of conductivity will

tend towards a value while the uncertainty decreases. This is a simple check to ensure accurate results, where the simulation can be extended if more data is required.

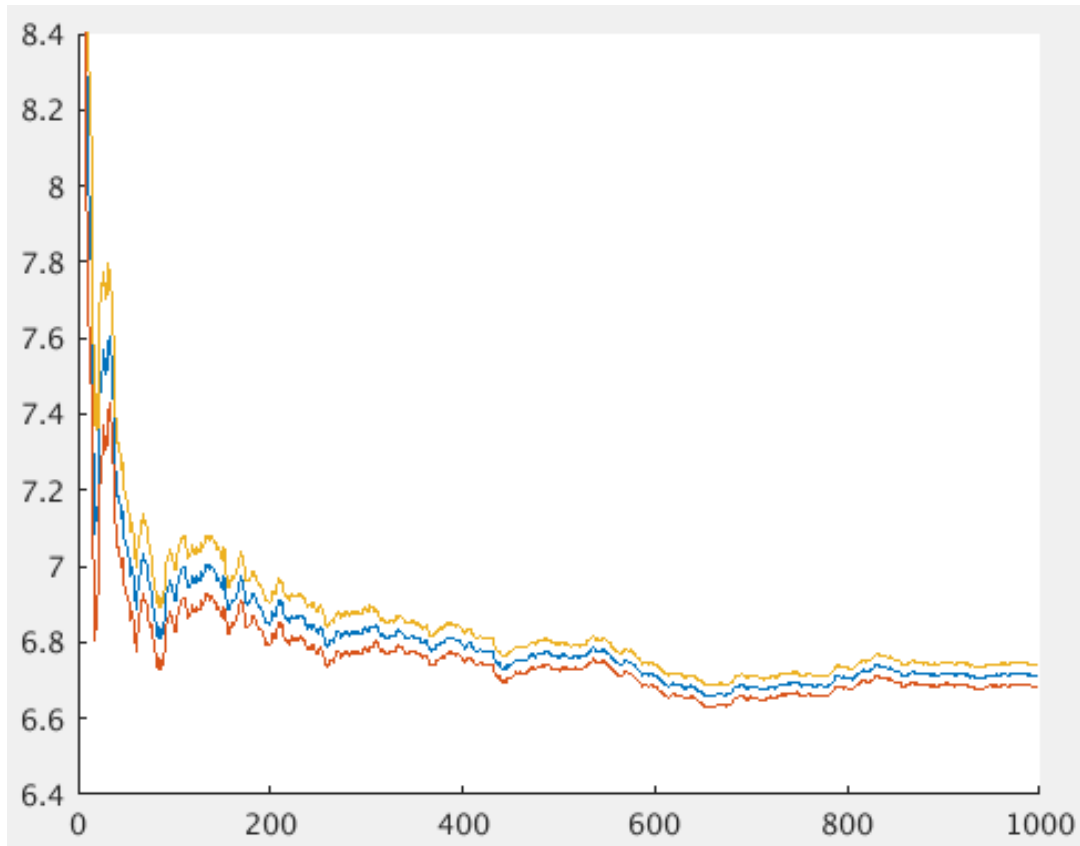


FIGURE 3.9: THIS FIGURE SHOWS CONVERGENCE - length = 48,



It is possible for a simulation to be too long however, where the conductivity result will drift from its converged position. This is due to inaccuracies in the molecular dynamics calculations, typically in the form of steepening temperature gradient over time. It is difficult to spot by just looking at the conductivity result and uncertainty, but easy to observe in the time series and/or graphically. The conductivity value obviously begins to change irrationally, and the uncertainty begins to increase. The uncertainty would never increase if the result was still converging, making this a useful marker to look for in the series.

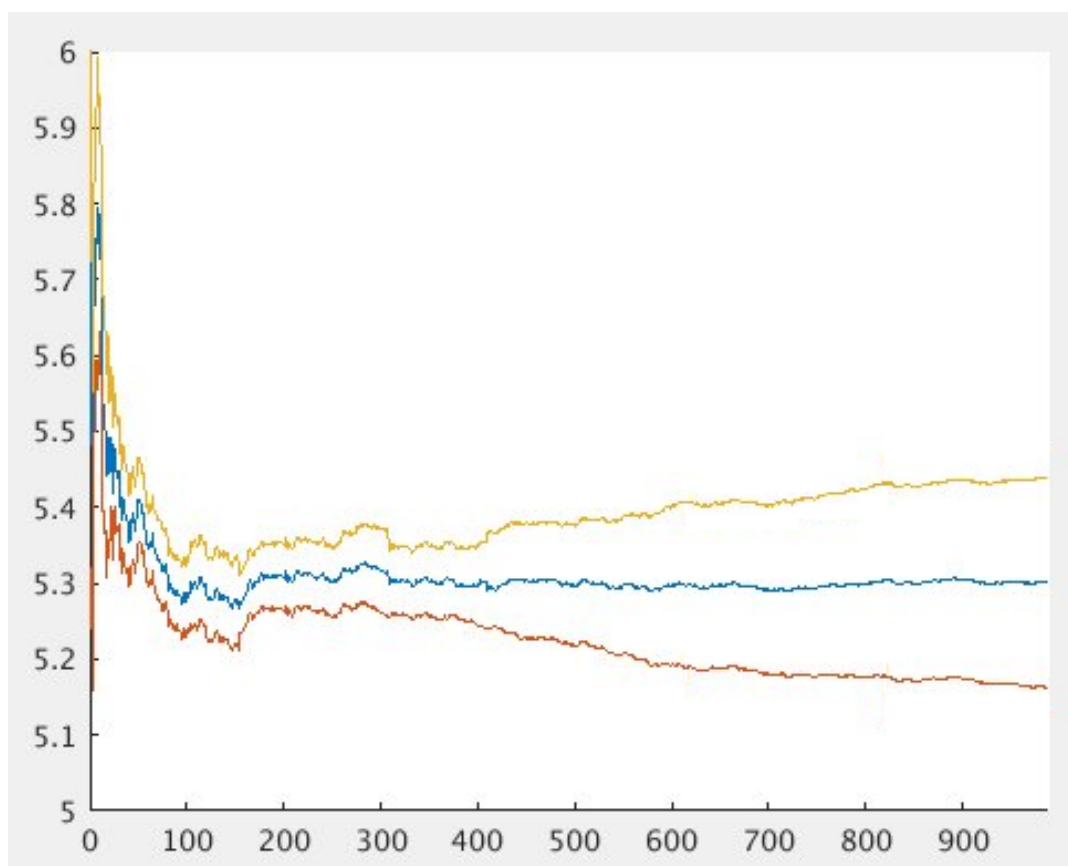


FIGURE 3.10: THIS FIGURE SHOWS DRIFT - length = 8, the equivalent raw would also work

### 3.3.5 Data processing

!!! FLYVBERG AND STUFF - ASK STEPHEN

### 3.3.6 Inverse extrapolation procedure

As discussed in Chapter 2.2.1, the results from simulations of varying cell lengths are combined to produce the conductivity result representative of the bulk material.

As I am aiming for a linear fit, I can use the lack of a linear fit to identify a simulation with problems caused by FSE.

### 3.3.7 Finite-size effects

4000 K

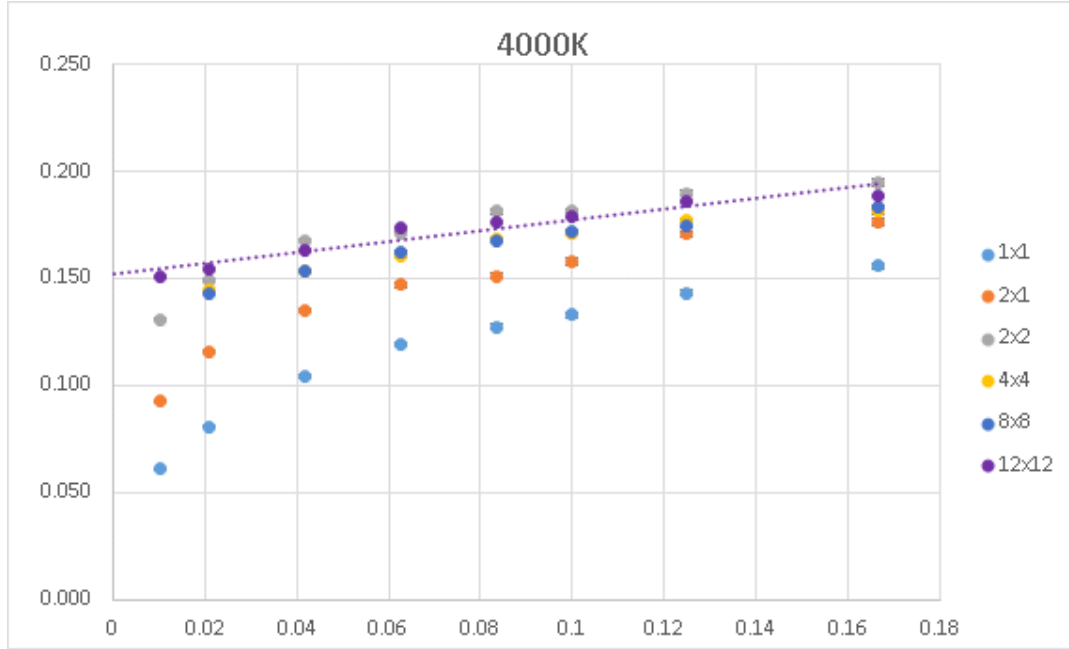


FIGURE 3.11: CAPTION

OBVIOUS CSA - One thing immediately obvious is that supercell CSAs of  $1 \times 1$  and  $2 \times 1$  overestimate conductivity (underestimate inverse conductivity) with respect to the larger CSAs. As discussed earlier, this can be attributed to the absence of realistic phonon scattering within a narrow material. For the supercells with shorter lengths (larger inverse length), increasing CSA (to  $2 \times 2$ ) brings the results into alignment.

TOO SHORT - Another problem becomes apparent when looking at the shortest cells in the series (longest inverse length), they appear to overestimate conductivity (underestimate inverse etc.) with respect to the expected linear fit through the other short cells (see the linear trend on Figure 3.11). This can be explained by the cell being on the order of the phonon MFP, allowing for phonons to travel from hot to cold without any scattering events (Ballistic Phonon Transport). This means the simulation does not have thermal resistance representative of the material. No correction can be applied here, the 6 unit cells long cells must be excluded from the extrapolation.

NOT-OBVIOUS CSA - While the shorter cells across all cross-sectional areas produce similar conductivity results, they diverge from the expected linear trend with length. The nature of the divergence is an overestimation of conductivity, the magnitude of which appears to be greater with smaller CSA. This suggests that there is some sort of aspect ratio finite-size effect. This is similar to the CSA effect mentioned above, whereby phonon-phonon scattering behaviour is not being replicated correctly. This explains why effect is larger the smaller the CSA, fewer possible phonons to participate in scattering events.

The divergence is all but removed when the  $12\times 12$  CSA is considered (see the small difference between data and fit in Figure 3.11). This is a significant computational cost however, and not really an efficient option for employing the direct method to calculate conductivity. I recommend ignoring cells with lengths longer than 24 UC. Computational cost increases with length, as does the divergence from linear behaviour. I can still produce accurate results using the cell lengths where  $2\times 2$  CSA cells produce the same results as those from  $12\times 12$  (see Figure 3.12), at a fraction of the cost. These key dimensions are somewhat arbitrary, only inferred from observations of the finite-size effects. Different materials require their own FSE analysis, despite any similarities in chemistry to bridgmanite or conditions to the lower mantle.

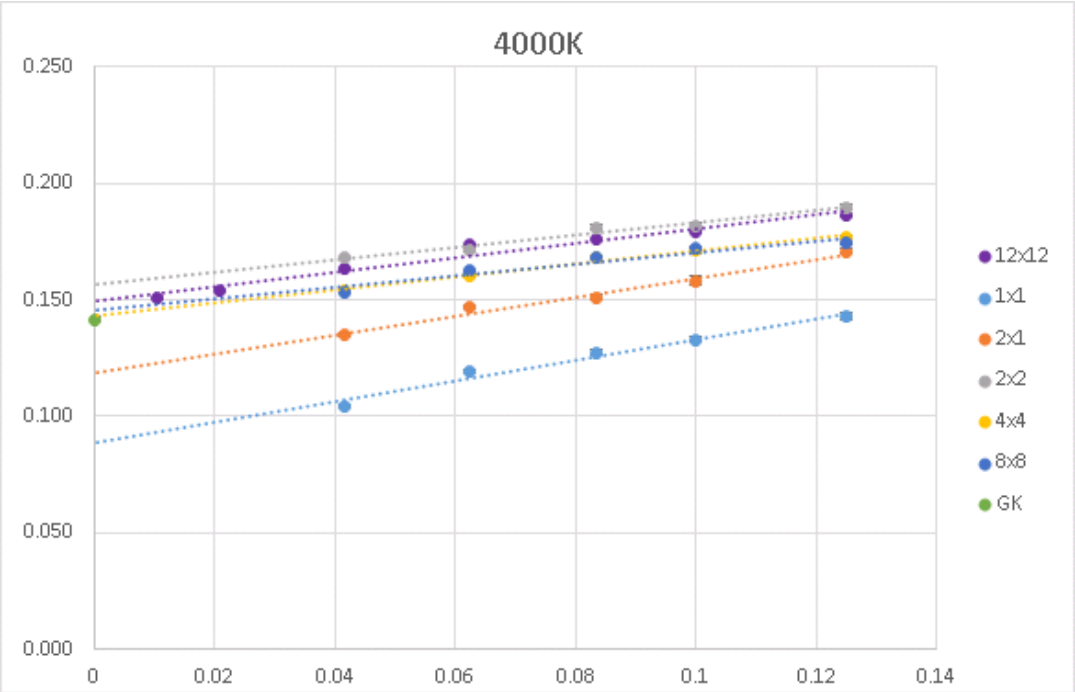


FIGURE 3.12: CAPTION

Comparison with the equivalent Green-Kubo point shows good agreement for the extrapolations from CSAs  $2\times 2$  and above. The  $12\times 12$  series extrapolates to  $6.7\text{ Wm}^{-1}\text{K}^{-1}$ , the spread of the other extrapolations is  $\pm 0.3\text{ Wm}^{-1}\text{K}^{-1}$ , with the GK point at around  $7.0\text{ Wm}^{-1}\text{K}^{-1}$ . WHAT MORE DO I SAY HERE?

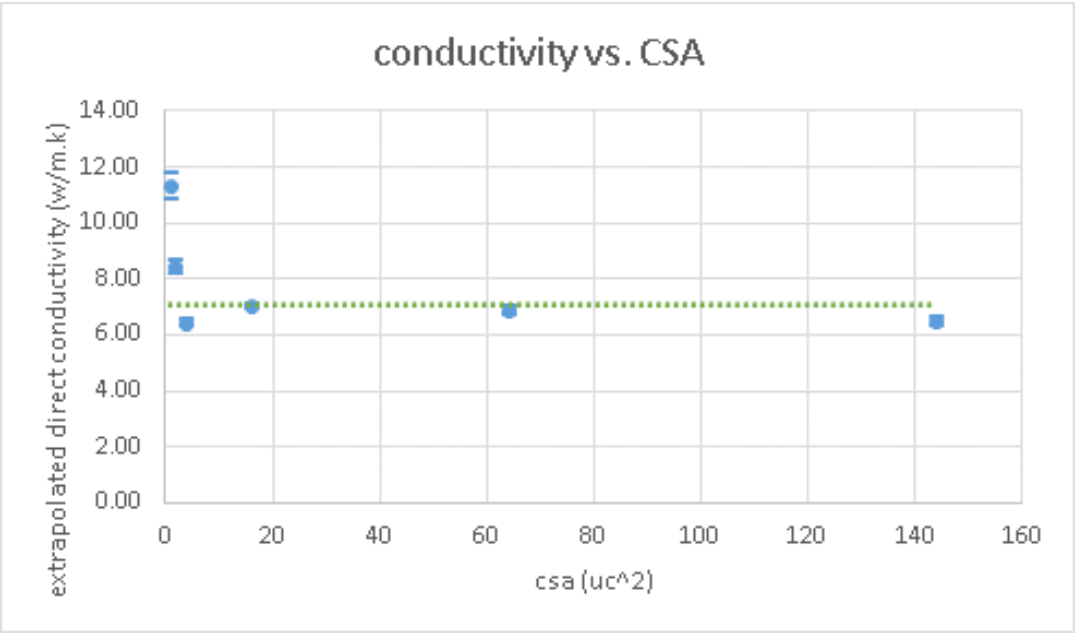


FIGURE 3.13: CAPTION

REDUNDANCY WITH THE ABOVE TEXT? - In summary, accurate bridgmanite conductivity results can be produced with the direct method when the cell CSA is greater than  $2 \times 2$ , and the length between 8–24 UC. This will be the most efficient use of computational resources. Different lower mantle minerals may require different simulation geometries, making them easier or more difficult to compute.

### 1000 K

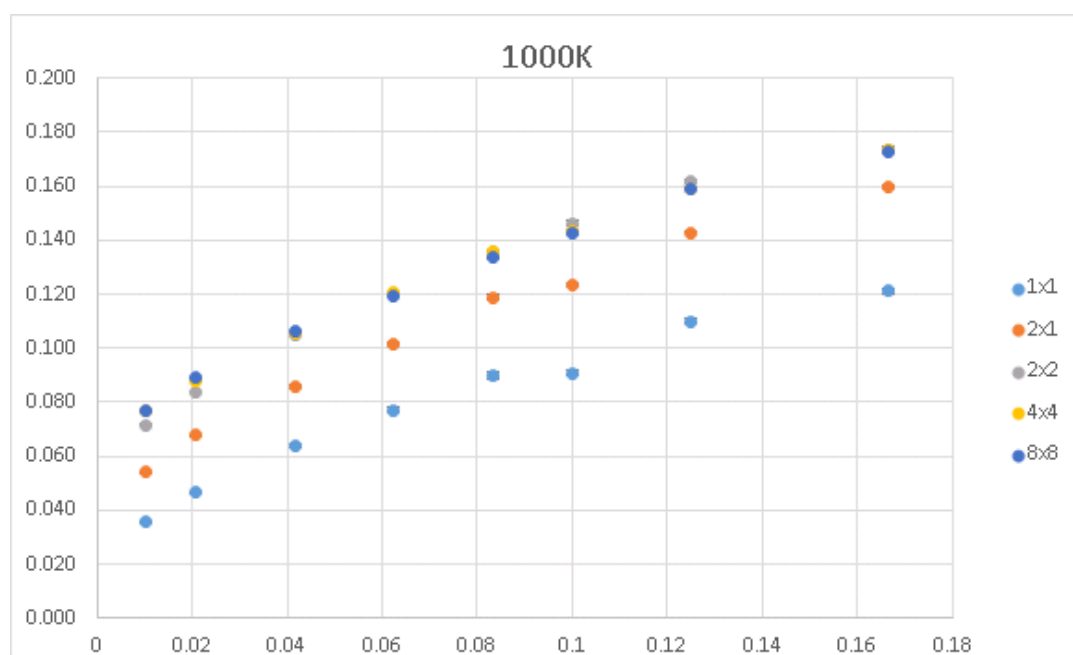


FIGURE 3.14: CAPTION

Everything is different with the FSE analysis at 1000 K. It still appears that the  $1 \times 1$  and  $2 \times 1$  CSAs overestimate conductivity, and that the smallest, 6 unit cell length data point overestimates conductivity compared to a hypothetical linear fit through the other points. Using cells between 8–24 UC for extrapolation does not produce conductivity results which agree with GK however.

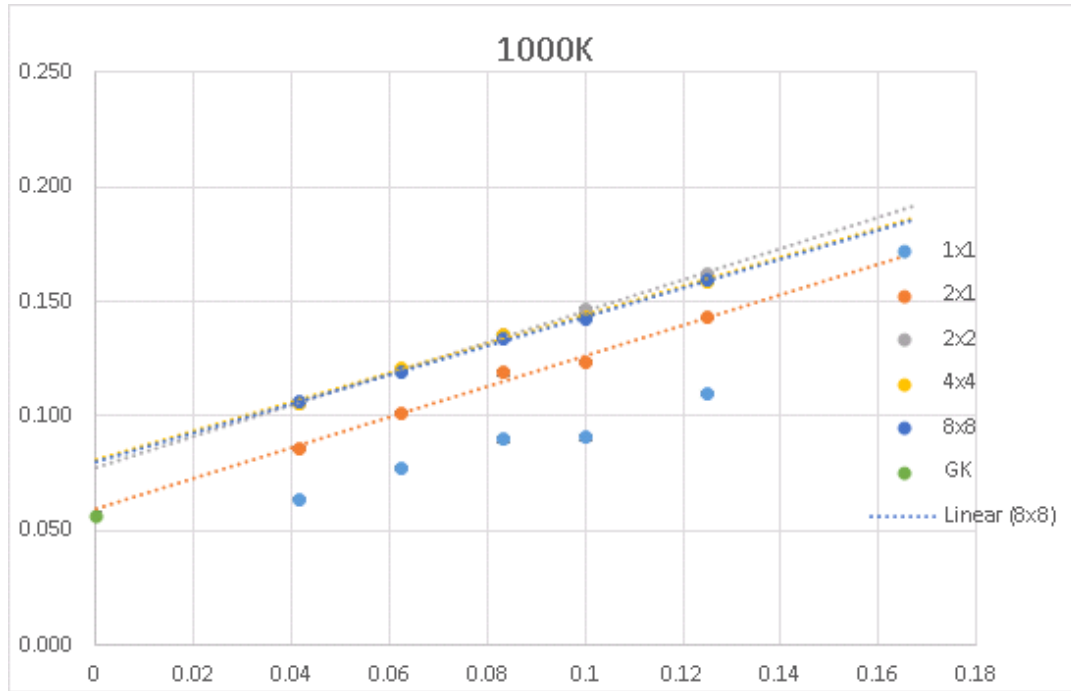


FIGURE 3.15: CAPTION

The discrepancy is around  $5 \text{ Wm}^{-1}\text{K}^{-1}$ ,  $12.5 \text{ Wm}^{-1}\text{K}^{-1}$  from direct method and  $17.5 \text{ Wm}^{-1}\text{K}^{-1}$  from Green-Kubo. The best CSA series to fit appears to be the  $2 \times 1$ . To get agreement between the two methods at these conditions, it appears cells longer than 48 UC should be considered. The  $2 \times 2$  or larger cells produce around the same result, suggesting convergence of the minimum CSA to the GK result.

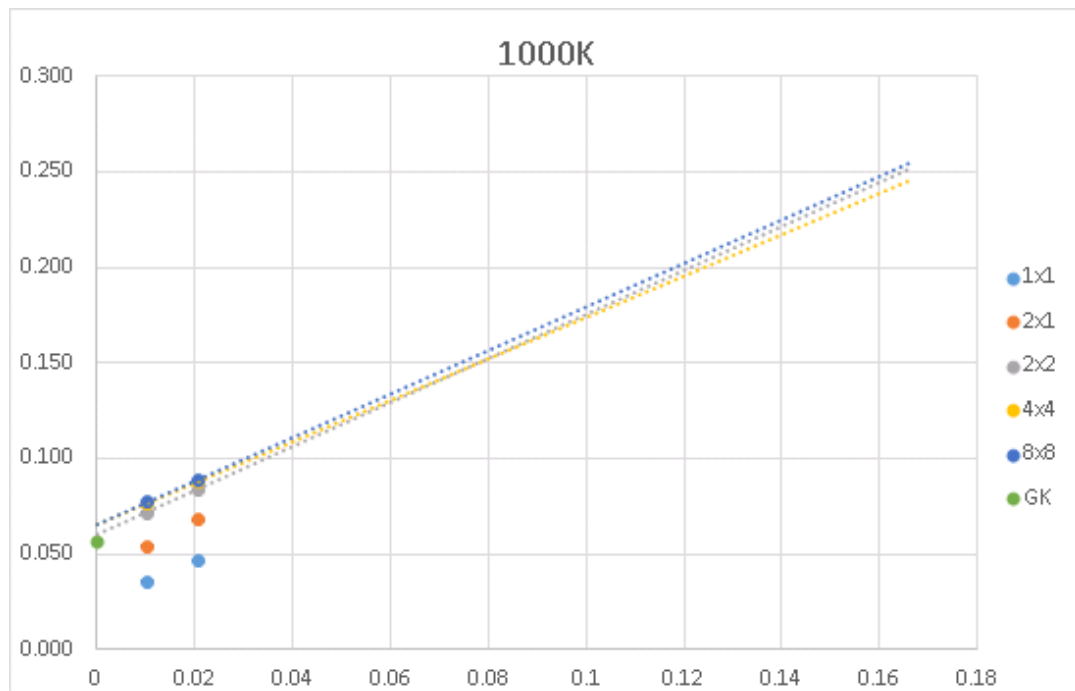


FIGURE 3.16: CAPTION

### 3.3.8 Explaining CSA effect

!!! GO THROUGH THEORY WITH STEPHEN - HU et al 2011

## 3.4 Summary

!!! EDIT ALL THIS

!!! STITCH METHODS TOGETHER IN THIS SECTION. COMPARE AND CONTRAST. PROBLEMS? HOW TO APPLY THIS GOING FORWARD?

For bridgmanite (at conditions representing the CMB), I show that use of the direct method for calculation of thermal conductivity will lead to an overestimate if the simulation cell is too long ( $>24$  unit cells). Small cross-sectional areas ( $<2 \times 2$  unit cells) also overestimate the thermal conductivity.

(ASSUMING THE RESULTS ARE CORRECT AND AGREE WITH GK) The non-linear region as described by Sellan et al. (2010) can be observed for the cell length of 6 unit cells, which has individually higher conductivity than expected from the linear fit through data points corresponding to lengths of 8–24 unit cells. When included in the extrapolation, this reduces the gradient of the fit, raising the intercept and thus causing conductivity to be underestimated.



I find conductivity is definitely dependent on CSA, and was able to increase CSA enough to eliminate aspect ratio-dependent divergence as reported by Hu et al. (2011). This does support my conclusion ignoring the longer cell lengths however, in order to ensure a linear fit is extrapolated and computational costs are kept low.

(WAFFLE ALERT) Ignoring the specifics of this study, I believe it is important to perform finite-size analysis when performing direct method calculations. Direct method cells spanning a range of lengths must be considered to find the linear regime for extrapolation. Cross-sectional area must be increased until the conductivity result converges. The same can be said about the Green-Kubo method, where the result converges with increasing volume. These effects vary with phonon mean-free path, sensitive to pressure, temperature, and compositional variations such as impurities. Completing finite-size effect analysis at conditions with the largest phonon mean-free path / thermal conductivity ensure all other conditions represent converged results. I believe classical molecular dynamics with interatomic potentials to be an excellent way of quantifying these effects quickly, to then utilise ab initio methods accurately (SHOULD I TAKE THIS SENTENCE OUT, NO PROOF OF THIS CLAIM).



## Chapter 4

# Modelling the thermal conductivity of Fe-bearing bridgmanite at the CMB

As stated previously, there are no experiments that can reach the high pressures and temperatures necessary to replicate the conditions of the lower mantle. The addition of impurities into minerals further complicates the matter. In addition to pressure and temperature-dependence, composition must be considered for full evaluation of lower mantle conductivity.

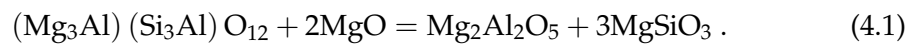
Manthilake et al. (2011) extrapolate their experimental results to lower mantle conditions, modelling conductivity for a 4 parts bridgmanite : 1 part ferropericlase compositional model. Their actual experimental results (performed between 500–1200 K) comprise of bridgmanite with iron and aluminium at 26 GPa, and ferropericlase at 8 and 14 GPa. At lower temperatures for any pressure or composition, adding any amount of impurity reduces conductivity by an order of around 3. The magnitude of this reduction decreases with temperature (as impurity-free conductivity decreases anyway), but impurities can have a huge effect. Conductivity decreases with temperature at a slower rate for the compositions with impurities, suggesting that reductions from impurities affect the reductions from other effects (such as temperature increase), and that there might be a minimum conductivity where there can be no further decreases.

Developing the methodologies presented in Chapter 3, in this chapter I will introduce iron into my existing bridgmanite model and establish the effects on lattice

thermal conductivity around the core-mantle boundary. This is in order to quantify conductivity as a function of temperature and composition, to use Fourier's law in assessing CMB heat flux with variable conductivity and temperature gradient.

## 4.1 Simulating the effect of atomic impurities

The bulk of the lower mantle comprises bridgmanite (~70%, and its high-pressure polymorph post-perovskite), ferropericlase (~20%), along with others (~10%) such as calcium silicate perovskite  $\text{CaSiO}_3$  (Trønnes, 2009). The composition can vary within these mineral archetypes, significantly the concentration of iron impurities. Magnesium is replaced with iron in  $\text{MgSiO}_3$  and  $\text{MgO}$  compositions, leading to  $\text{FeSiO}_3$  and  $\text{FeO}$  endmembers. Aluminium can similarly be substituted for Magnesium and Silicon (as in Brodholt, 2000) where,



Impurities reduce thermal conductivity by providing more opportunities for phonon scattering events. An impurity is an irregularity to a propagating phonon, much like a speedbump to a car. They have different properties to the atoms the phonon expects to meet from crystal regularity, namely mass and their bonds with neighbouring atoms. For this reason that the thermal conductivity of a solid solution is lower at intermediate compositions than at the endmembers. Even if one endmember has lower conductivity than the other, an irregular mix of the two can produce even lower values.

### 4.1.1 How do impurities affect conductivity?

The effect of impurities on lattice thermal conductivity is approximated by Klemens (1960) and Padture and Klemens (1997), a review of which can be found in the Supplementary Material of Stackhouse et al. (2015). Equations hereafter in this section with a SS-prefix refer to their position in this supplementary material. The lattice

thermal conductivity of a binary solid solution is given (Eq. SS6) as

$$\kappa_{SS} = \kappa_V \left( \frac{\omega_0}{\omega_D} \right) \arctan \left( \frac{\omega_D}{\omega_0} \right), \quad (4.2)$$

where  $\omega_0$  is the phonon frequency at which the mean free path is equal to that of the solute atoms, and  $\omega_D$  is the phonon frequency corresponding to the maximum of the acoustic branch in the phonon spectrum (the Debye frequency).  $\kappa_V$  is the compositionally-weighted (Voigt) average of endmember conductivities,

$$\kappa_V = (1 - C) \kappa_1 + C \kappa_2, \quad (4.3)$$

where  $\kappa_1$  and  $\kappa_2$  are the solid solution endmember conductivities, and  $C$  is the fractional concentration of the second endmember (Eq. SS7).

#### 4.1.2 Why does this model work?

When  $\omega_0 \gg \omega_D$ ,  $\arctan(\omega_D/\omega_0) \rightarrow (\omega_D/\omega_0)$ , so  $\kappa_{SS} \rightarrow \kappa_V$ , the conductivity including the effect of impurities tends toward the endmember linear average. This is the scenario when other factors, such as Umklapp processes at high temperatures, have caused conductivity to decrease significantly. Adding impurities at this point has little additional effect, conductivity is already close to its saturated minimum.

On the other hand, when  $\omega_D \gg \omega_0$ ,  $\arctan(\omega_D/\omega_0) \rightarrow \pi/2$ , but  $(\omega_0/\omega_D) \ll 2/\pi$ , so  $\kappa_{SS} < \kappa_V$ , and impurity scattering has a noticeable effect on the resultant conductivity. Adding impurities affects conductivity in this fashion when phonon-phonon collisions are not the dominant conductivity reducing process, like at low temperatures compared to the conditions mentioned in the above case. Additional information on  $\omega_0$  will be given at the end of this subsection.

#### 4.1.3 What effects the magnitude of impurity scattering?

That factors that affect the severity of impurity scattering are temperature, the mass difference between the impurity and what it replaced, and the concentration of said replacements. The ratio of the phonon frequencies in Eq. 4.2 can be expressed

(Eq. S11) as

$$\left(\frac{\omega_0}{\omega_D}\right)^2 = \frac{1}{(6\pi^2)^{1/3}} \frac{T}{3\epsilon T_0}, \quad (4.4)$$

where  $T$  is temperature,  $T_0$  is the temperature associated with  $\omega_0$ , and  $\epsilon$  is related to the mass difference and proportion of endmembers by

$$\epsilon = \frac{(M_2 - M_1)^2}{\bar{M}^2} C(1 - C), \quad (4.5)$$

where  $M_i$  is the atomic mass of the  $i$ -th endmember,  $\bar{M}$  is the mean atomic mass of the solid solution, and  $C$  is the proportion of endmembers (Eq. SS9).

As the temperature increases, so too does the left-hand side of Equation 4.4. As discussed earlier, this reduces the effect of scattering caused by impurities, which will be relevant at CMB conditions where temperature is large ( $\sim 4000$  K).

$\epsilon$  increases with the mass difference of the endmembers, and the impurity concentration. Increasing  $\epsilon$  tends to reduce the phonon frequency ratio, meaning impurity scattering will affect the resultant conductivity more. The atomic masses of Mg and Fe are 24 and 56, so FeSiO<sub>3</sub> is 1.32 times heavier than MgSiO<sub>3</sub>.

As an aside, Equation 4.5 predicts that isotopic variations will have little effect on conductivity, where the mass changes are typically small (e.g. <sup>24</sup>Mg to <sup>25/26</sup>Mg) and abundances are low (Mg standard atomic weight is 24.3, the ratio of <sup>24</sup>Mg to heavier isotopes is roughly 4:1). Mass difference is an additional reason why Fe impurities are more interesting theoretically than Al. The mass of Al is 27, compared to Mg with 24 and Si at 28.

The composition control term in Equation 4.5,  $C(1 - C)$ , increases from 0 to 0.25, when  $x = 0.5$ .  $\epsilon$  increases with composition up to 50%, the furthest point away from both endmembers, therefore the condition of most disorder in the model. While I investigate the full range of  $C$ , most of the lower mantle will have Fe content no greater than 15% (Lee et al., 2004). Knowledge of conductivity up to FeSiO<sub>3</sub> composition is interesting if ultra low velocity zones are thermochemical features of high Fe content (e.g. Mao et al., 2004; Dobson and Brodholt, 2005).

#### 4.1.4 Phonon frequency and relaxation time

The compositional model presented by Klemens considers the ratio of phonon frequencies, and the contribution of these frequencies to the effective relaxation time of the system.  $\omega_0$  is defined (by Klemens, 1960, Eq. 11) as the frequency at which

$$\tau'(\omega_0) = \tau_u(\omega_0), \quad (4.6)$$

where  $\tau'$  and  $\tau_u$  are the contributions of point defect scattering and Umklapp processes respectively to the effective phonon relaxation time (Klemens, 1960, Eq. 2 & 3), where

$$1/\tau' = A\omega^4, \quad (4.7)$$

and

$$1/\tau_u = B\omega^2. \quad (4.8)$$

The effective phonon relaxation time of the system, using the Matthiesen Rule (modified from Klemens, 1960, Eq. 7), is

$$\frac{1}{\tau(\omega)} = \frac{1}{\tau_u} + \frac{1}{\tau'}. \quad (4.9)$$

When Equation 4.6 is satisfied, the effective relaxation time will equal to half of either its constituents,

$$\frac{1}{\tau(\omega_0)} = \frac{1}{\tau_u} + \frac{1}{\tau'} = \frac{1}{\tau_{\omega_0}} + \frac{1}{\tau_{\omega_0}} = \frac{2}{\tau_{\omega_0}}. \quad (4.10)$$

When  $\tau' \neq \tau_u$ , the effective relaxation time will tend toward the smaller of the two as the difference increases. I illustrate in Figure 4.1 that a process' relaxation time will dominate the other in the effective behaviour when it is around 1,000 times smaller. At the point where the contribution is equal (i.e. 0.5), the  $\omega_0$  criterion is satisfied (Eq. 4.6). The contribution varies linearly when the magnitudes of the relaxation times are comparable, adopting an arctan-like form when they vary greatly.

For a CMB-like condition of high temperature, Umklapp process relaxation time is short (left hand side of Fig. 4.1). Adding impurities (reducing  $\tau'$ ) doesn't contribute much to an already large scattering effect. Where the Umklapp process relaxation time is longer (temperatures decreasing towards Debye temperature), even

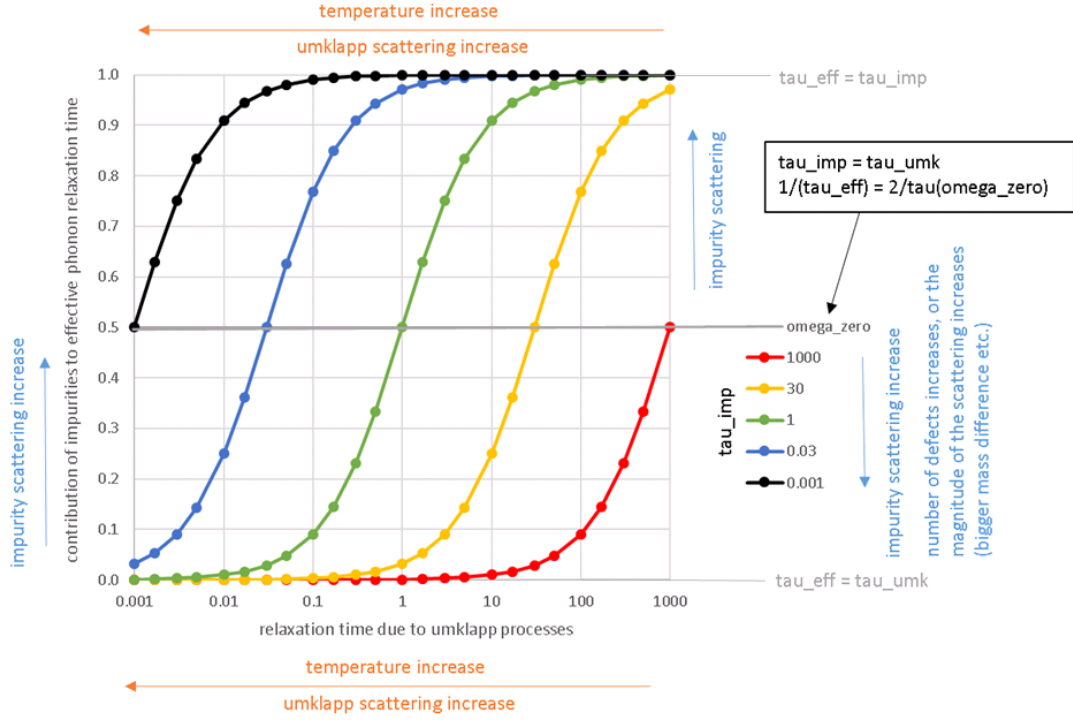


FIGURE 4.1: For a series of  $\tau'$ , their contribution to the effective phonon relaxation time is plotted against  $\tau_u$ . The quantity on the y-axis is the normalised difference in effective phonon relaxation time, comparing just Umklapp processes to Umklapp and the impurity scattering effect (as in Eq. 4.9).

adding a small amount of atomic impurity can influence the effective system behaviour. Considering the average phonon velocity, a longer relaxation time means a greater distance travelled, or phonon mean free path.

Calling back to Equation 4.7 & 4.8,  $A$  and  $B$  are constants, where only the latter is temperature-dependent ( $T$ ). The contribution of point defect scattering to the effective phonon relaxation time is constant with temperature (varying with impurity concentration and composition). It is the relative magnitude of  $\tau_u$ , which decreases with temperature ( $\propto 1/T$ , via  $B$ ), to  $\tau'$  that influences the effect of impurities on thermal conductivity (see Equation 4.9).

The two relaxation time terms above can be equated via Equation 4.6, showing  $\omega_0$  is similarly temperature-dependent

$$A\omega_0^4 = B(T)\omega_0^2,$$

$$\omega_0^2 = B(T)/A,$$



$$\omega_0 \propto T. \quad (4.11)$$

The Debye frequency is a constant, so

$$\left( \frac{\omega_0}{\omega_D} \right) \propto T. \quad (4.12)$$

As temperature increases (above the Debye temperature), conductivity decreases because of Umklapp processes. The significance of point defect scattering (but not the magnitude of its relaxation time) decreases as the effect of phonon-phonon scattering increases. Therefore the relative conductivity decrease due to impurities is inversely proportional with temperature, and less important as conductivity tends towards its saturated minimum.

## 4.2 Methodology

In this section I outline the process of taking Fe from chemistry to computer, by fitting my own coefficients to a Buckingham potential. I also go over how the Fe is incorporated into the  $\text{MgSiO}_3$ , considering its placement and concentration.

### 4.2.1 How does iron behave?

There are two reasonable methods I could use to introduce iron impurities to my bridgmanite models. The first approach is to simply create a magnesium atom with the mass of an iron atom, without changing any coefficients of the interatomic potentials from Oganov et al. (2000). Despite being an obviously "quick and dirty" method, I will show in Section 4.5.1 this is a reasonable first-order approximation. As the variation in mass number from Mg to Fe is large (24 to 56, a 133% increase), it is likely to change the behaviour of the system more than a subtle change in the atomic interactions.

Approximating Fe with heavier Mg atoms is used by Ammann et al. (2014) to investigate  $(\text{Mg,Fe})\text{SiO}_3$  with 20% impurity content at 20 GPa and 2000 K. They found the effect of adding impurities in this manner was variable on a number of factors (crystallographic direction, interatomic potential), and observed saturation in the conductivity decrease with concentration.

The second approach to add Fe into the  $\text{MgSiO}_3$  system is to fit interatomic potentials, as well as using the aforementioned mass change for a more realistic model. An in-depth review of these approaches can be found in Section 4.5.1. I adapted the Oganov et al. (2000)  $\text{MgSiO}_3$  Buckingham interatomic potential ( $U$ ) to include the Fe-O interaction (see Table 4.1). I determined two short-range potential parameters,  $b$  and  $\rho$ , shown in Eq. 11 from Oganov et al. (2000),

$$U_{ij}(R_{ij}) = \frac{z_i z_j}{R_{ij}} + b_{ij} \exp\left(-\frac{R_{ij}}{\rho_{ij}}\right) - \frac{c_{ij}}{R_{ij}^6}, \quad (4.13)$$

where  $ij$  refers to an atom pair,  $R$  is interatomic distance,  $z$  is atomic charge, and  $c$  relates to the Van der Waals force (zero for non O-O interactions). I determine  $\rho$  in the same fashion as Oganov et al. (2000), calculated from the atomic first ionisation potentials,

$$\rho_{ij} = \frac{1.85}{\sqrt{I_i} + \sqrt{I_j}}. \quad (4.14)$$

$b$  is constrained using the GULP code (Gale, 1997), using the calculated  $\rho$  value for Fe-O. I fit to structural information from Parise and Wang (1990), an experimental study of  $(\text{Mg}_{0.9}\text{Fe}_{0.1})\text{SiO}_3$  bridgmanite at ambient conditions. This study was chosen as it matches the conditions at which Oganov et al. (2000) fit their potential.

TABLE 4.1: Parameters used to define Oganov et al. (2000)'s  $\text{MgSiO}_3$  perovskite potential, including my fit Fe-O values.

Bond $ij$	$b_{ij}$ (eV)	$\rho_{ij}$ (Å)	$c_{ij}$ (eV.Å <sup>6</sup> )
Mg-O	1041.435	0.2866	0
Si-O	1137.028	0.2827	0
O-O	2023.800	0.2674	13.83
Fe-O	1440.437	0.2846	0

Despite potential fitting being an improvement on solely changing atomic mass, it is not perfect as I do not vary atomic charge from Mg to Fe. The problem is additionally complicated by the Fe-partitioning between  $\text{MgSiO}_3$  and  $\text{MgO}$ , the effect of ferrous vs. ferric iron, and how spin state affects properties such as conductivity as it varies along the geotherm (e.g. Ohta et al., 2017). These additional complexities are beyond the scope of this project, where only ferrous iron will be considered. The effects of impurities (i.e. some kind of irregular atom) is interesting, even if the exact chemistry is not accurate.

### 4.2.2 Where do the impurities go?

Iron is substituted with magnesium into the bridgmanite atomic structure. The unit cell contains 4 Mg atoms, and the smallest direct method cell I employ is a 6x2x2 supercell. Therefore the smallest amount of iron that can be added is 1/96 atoms, a concentration just over 1%. I use a simple MATLAB script is used to modify LAMMPS input files, randomly selecting a specified proportion of Mg atoms to be replaced with Fe. When a Mg atom changes to Fe, its mass and interatomic potential properties change.

Due to the microscopic nature of the system, you wouldn't want all of the added iron to be concentrated together in the simulation cell, especially in a heat source/sink region. To avoid this I order Mg atoms by length along supercell, and change a single atom every so many. For example, changing 1/4 atoms is different to changing 24/96. The latter has a higher variance in Fe per unit length, and the former chooses one atom to swap for every four along the system. These distributions are illustrated in Figure 4.2. After iron is added, the standard direct method or Green-Kubo workflow is followed.

## 4.3 Results

Lattice thermal conductivities obtained from Green-Kubo calculations are plotted against temperature in Figure 4.3, for Mg and Fe-endmembers and the 50/50 solid solution mix. Each Green-Kubo data point presented herein is obtained from 8 initial temperature conditions, each producing 10 ACFs/integrals, totaling 80 ns of simulation time.

Conductivity decreases with temperature, approximately following  $\kappa \propto 1/T^{0.9}$  at the pressure of 136 GPa considered here. This is in contrast to the typically expected  $\kappa \propto 1/T$  relation, indicating some kind of saturation in conductivity decrease with temperature.

FeSiO<sub>3</sub> has a consistently lower conductivity than MgSiO<sub>3</sub>, although both species may converge given a high enough, albeit unphysical, lower mantle temperature. This suggests there is a minimum conductivity associated with the crystal structure, reached first by FeSiO<sub>3</sub> with its inherently lower conductivity.

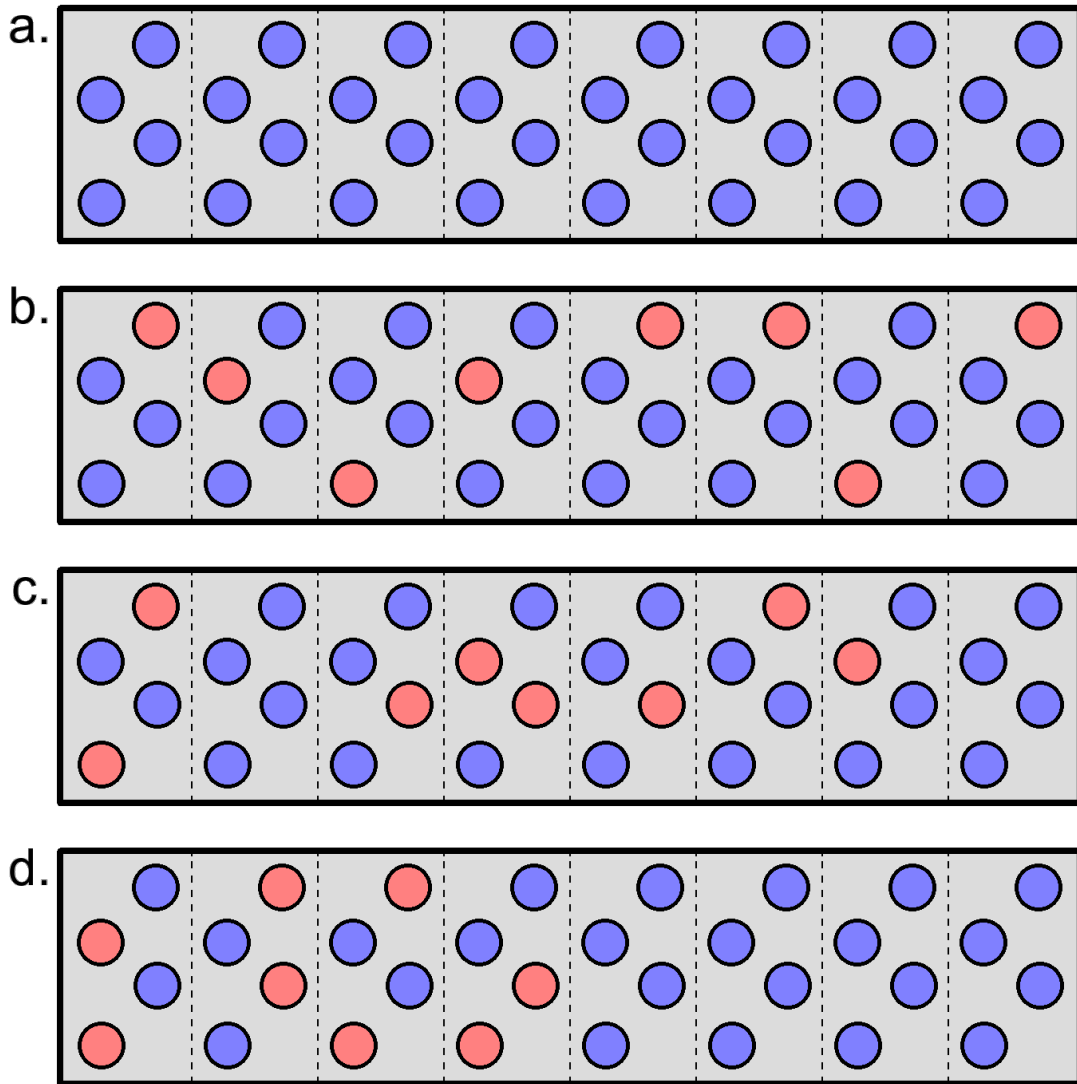


FIGURE 4.2: A cartoon showing the side view of Mg atoms in  $\text{MgSiO}_3$  along a supercell of dimensions  $8 \times 1 \times 1$ , where dashed lines mark a cell boundary. **a.** shows a  $\text{MgSiO}_3$  endmember composition (blue balls), with no Fe replacements. **b-d.** all show  $(\text{Mg,Fe})\text{SiO}_3$ , with 25% Fe substitution (red balls). **b.** shows a homogeneous distribution along a length unit, equal to a cell, or 1 substitution out of every possible 4 along length. **c.** shows the same Fe% concentration (8/32 replaced), but with a random distribution along the length. **d.** again has the same composition, but all the iron is clumped in the first half of the length. This scenario produces greatly differing temperature gradients on both halves when applying the direct method.

The 50% solid solution has a consistently lower conductivity than  $\text{MgSiO}_3$ , and a lower than or equal to relation to  $\text{FeSiO}_3$ . This is again to be expected, conductivity decreases from endmember to intermediate compositions as impurity concentration increases. It can be seen that conductivity differences are very small at high temperatures for  $\text{FeSiO}_3$  and the solid solution. If  $\text{FeSiO}_3$  has already reached its theoretical minimum, adding impurities will do little to decrease it further.

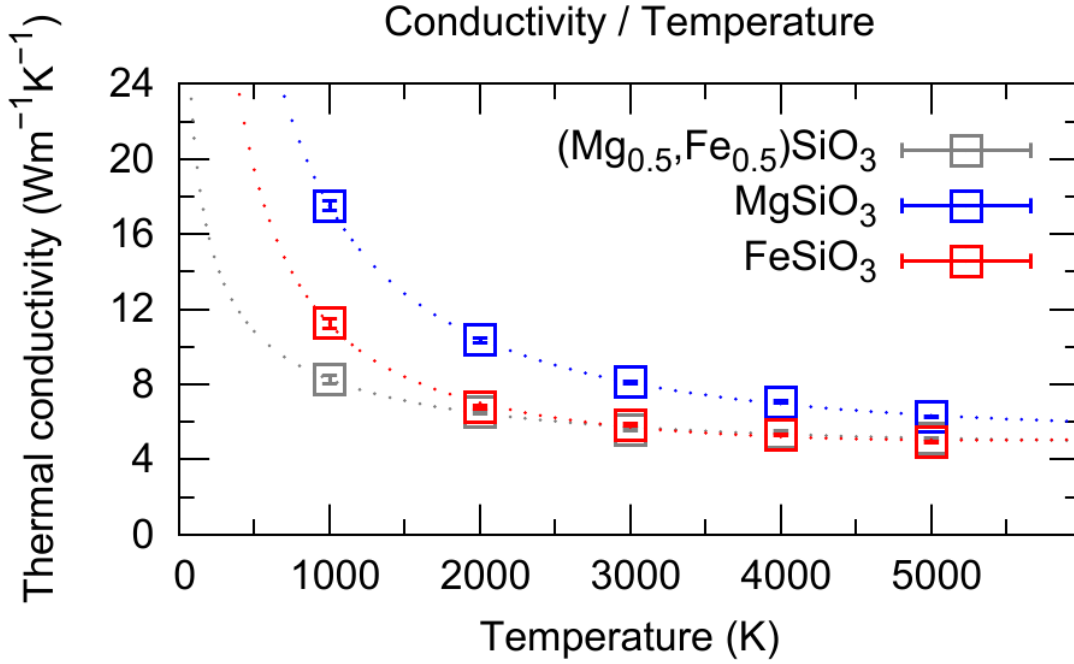


FIGURE 4.3: Data points are GK conductivity results, dotted line is the fit from Equation 4.25.

An alternative perspective to Figure 4.3 is presented in Figure 4.4, where Green-Kubo conductivity results are plotted as a function of Fe impurity content for several temperature series. Conductivity generally decreases with increasing temperature at all compositions, though the change becomes minimal at temperatures above 3000 K.

The MgSiO<sub>3</sub> endmember has a consistently higher conductivity than the FeSiO<sub>3</sub>. This can be explained by the reduction in shear modulus and increase in density associated with adding Fe, which decreases seismic velocity and thus conductivity.

The amount of Mg atoms replaced with Fe has a variable effect on conductivity. A better way to label the effect is impurities added to an endmember, i.e. Fe is added to MgSiO<sub>3</sub> and Mg to FeSiO<sub>3</sub>, which always serves increase phonon scattering and decrease conductivity. The decrease from this effect saturates towards a 50% compositional mix. At high temperatures, this effect is minimal when adding Mg to FeSiO<sub>3</sub>. The conductivity could already be close to its theoretical minimum due to temperature effects, little reduction is observed from adding impurities.

A simple interpolation between endmember conductivities is insufficient, the

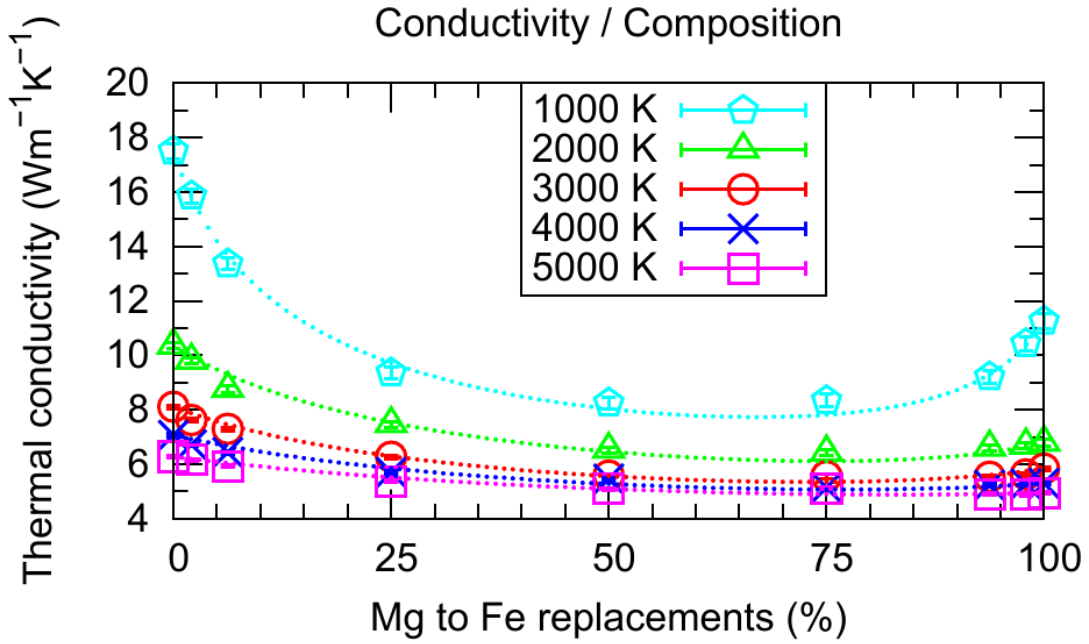


FIGURE 4.4: Computed thermal conductivities plotted as a function of Fe concentration for a range of temperatures. Dotted line for each series represents the model fit.

presence of a compositional mix has an effect. This effect is itself temperature-dependent, the trough-like trend flattens with increasing temperature. These temperature and compositional dependences can be combined, allowing conductivity to be determined for a range of possible CMB conditions (Figure 4.5).

#### 4.4 Parameterising composition and temperature effects on CMB conductivity

In this section I develop a model for the lattice thermal conductivity of  $(\text{Mg,Fe})\text{SiO}_3$  perovskite at CMB conditions. Whilst the CMB is a small section of the lower mantle, it marks the heat flow boundary from core to mantle. Mantle-side thermal conductivity controls the nature of this heat flow, making it an important parameter in studies on both sides of an important interface. The CMB is isobaric at 136 GPa, and isothermal at an uncertain temperature. Fe-content can vary with position. In terms of making a model I can collect data at one pressure condition, and investigate how an array of temperatures and compositions affect thermal conductivity.

Due to uncertainty in the lower mantle's composition, properties like thermal

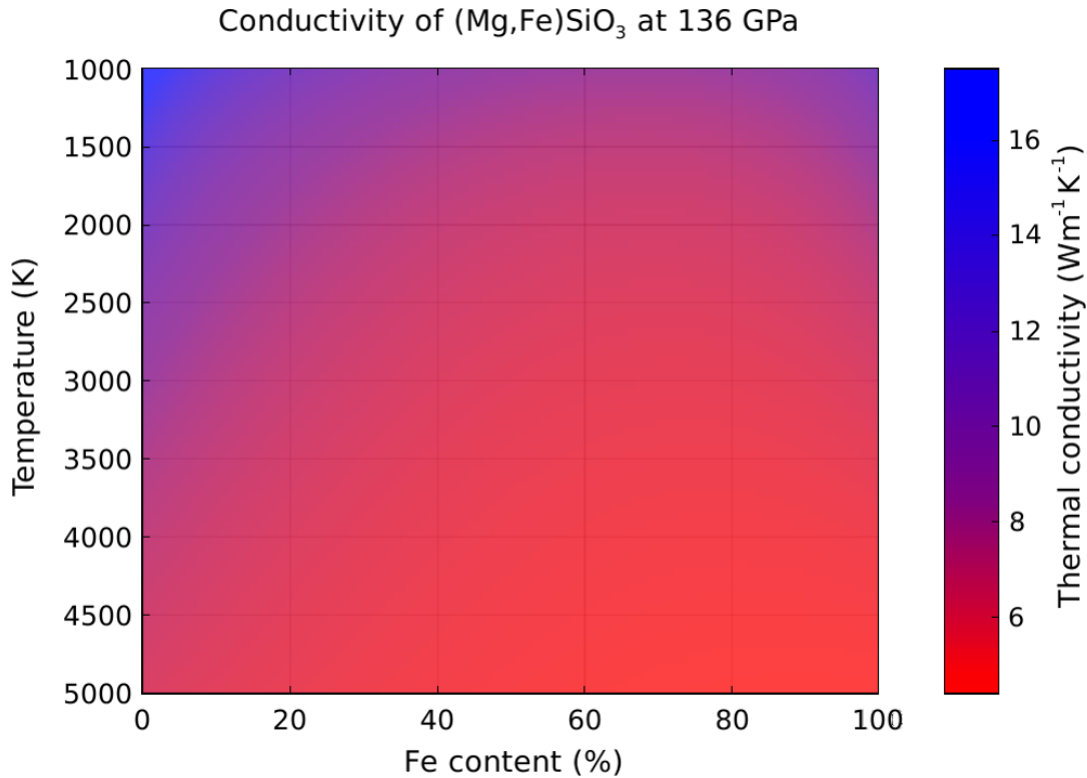


FIGURE 4.5: Modelled conductivity, shown plotted against temperature and composition. Note the sensitivity of the colour scale, showing low conductivities as dominant at high temperatures and intermediate compositions. High values are found only at low temperatures, and even then they rapidly decay and saturate to  $<8\text{Wm}^{-1}\text{K}^{-1}$ . Such conditions are unphysical at 136 GPa within the lower mantle.

conductivity are often averaged considering the abundance of each mineral component. There are also solid solutions to consider though, particularly the concentration of Fe in  $\text{MgSiO}_3$ , as well as the phase boundary between bridgmanite and  $\text{MgSiO}_3$  post-perovskite.

The conductivity of an intermediate composition is not a simple weighted average of the endmember values, you cannot interpolate linearly. This can be seen in Figure 4.3, where the  $(\text{Mg}_{0.5}\text{Fe}_{0.5})\text{SiO}_3$  results do not plot between those of  $\text{MgSiO}_3$  and  $\text{FeSiO}_3$ .

Equations and functional forms exist for the temperature and compositional dependence of thermal conductivity, and it is possible to combine the two. The basic idea is to determine the conductivity of  $\text{MgSiO}_3$  and  $\text{FeSiO}_3$  endmembers at the temperature of interest, and then apply the (temperature-dependent) effect of composition.

Padture and Klemens (1997) propose a model for how impurities affect lattice

thermal conductivity of a solid solution, which Ohta et al. (2017) use to fit experimental ferropericlase data. Following a similar methodology, I fit the functional form to my (Mg,Fe)SiO<sub>3</sub> perovskite results at various temperatures (1000 K, 2000 K, 3000 K, 4000 K, and 5000 K). In an additional step, I establish how the functional forms change with temperature, the temperature-dependence of the compositional-dependence if you will.

Okuda et al. (2017) present a temperature scaling relation for lattice conductivity (originally from Manthilake et al., 2011), fit to their experimental results of bridgmanite. I apply this temperature scaling to computational results of MgSiO<sub>3</sub> and FeSiO<sub>3</sub> at 136 GPa. With the temperature dependence of these endmembers and of the compositional effect, I am able to determine the conductivity of any composition, interpolating to temperatures in the range 1000 K to 5000 K, at 136 GPa pressure representative of the CMB.

The aforementioned temperature dependence from Manthilake et al. (2011) considers density, allowing conductivity to be determined as a function of temperature and pressure. In the examples I will present, I am only concerned with systems at 136 GPa. All density changes will result from thermal expansion, and the equations will be altered to accommodate this.

#### 4.4.1 Compositional dependence

The lattice thermal conductivity of a solid-solution as a function of temperature and composition can be approximated by the following equation (first seen as Eq. 4.2),

$$\kappa_{SS} = \kappa_V \left( \frac{\omega_0}{\omega_D} \right) \arctan \left( \frac{\omega_D}{\omega_0} \right), \quad (4.15)$$

where  $\omega_0$  is the phonon frequency at which the Umklapp/regular processes and impurity scattering effects' contributions to the mean free path and relaxation time (distance and time respectively travelled by a phonon) are equal. In terms of generating thermal resistance, neither effect dominates over the other at this frequency.  $\omega_D$  is the phonon frequency corresponding to the maximum of the acoustic branch in the phonon spectrum (the Debye frequency).  $\kappa_V$  is the conductivity of the solid solution in the absence of impurity scattering (previously as Eq. 4.3, modified for



the specific (Mg,Fe)SiO<sub>3</sub> endmembers)

$$\kappa_V = (1 - C) \kappa_{\text{MgSiO}_3} + C \kappa_{\text{FeSiO}_3} , \quad (4.16)$$

where  $C$  is the fractional concentration of Fe, and  $\kappa_{\text{MgSiO}_3}$  and  $\kappa_{\text{FeSiO}_3}$  the temperature dependent conductivities of the endmembers. The ratio of the phonon frequencies can be expressed as

$$\left( \frac{\omega_0}{\omega_D} \right)^2 = \frac{\chi^T}{C(1 - C)} , \quad (4.17)$$

where  $\chi$  is a temperature-dependent constant, and  $T$  is the temperature of interest (Padture and Klemens, 1997).  $\chi$  can be thought of as a measure of resistance to the effects of impurity scattering. The  $\kappa$  against  $C$  relationship (Figure 4.4) shows a larger effect of impurity scattering in the form of greater curvature when  $T$  and  $\chi$  are lower (see Table 4.2). For a given  $T$  and  $C$ , increasing  $\chi$  causes the phonon frequency ratio  $\left( \frac{\omega_0}{\omega_M} \right)$  to increase which, as discussed in Section 4.1.1, means  $\kappa_{\text{latt}}$  tends towards  $\kappa_i$ .  $\chi$  is fit to the data at each temperature, but for the model it needs to be a function of temperature. Figure 4.6 shows a plot of  $\chi$  against  $T$  with a power law (LEFT/B.) and 4th-order polynomial (RIGHT/B.), the former of which is a poor fit and the latter an egregious overfitting.

TABLE 4.2: Variation with temperature of parameters used to fit the chemical and temperature-dependences. Reference volume from 1000 K for both endmembers.

		Temperature (K)				
		1000	2000	3000	4000	5000
Conductivity (Wm <sup>-1</sup> K <sup>-1</sup> )	Mg	17.51	10.36	8.11	7.07	6.28
	Fe	11.26	6.79	5.84	5.30	4.95
Volume (Å <sup>3</sup> )	Mg	5960	6017	6075	6136	6199
	Fe	6253	6310	6369	6431	6500
$V_{\text{ref}}/V(T)$	Mg	1	0.9906	0.9811	0.9714	0.9616
	Fe	1	0.9909	0.9817	0.9723	0.9619
$\chi$		0.9973	0.9992	0.9996	0.9998	0.9999
$\chi^T$		0.0649	0.2035	0.2748	0.4277	0.7494

The lack of an obvious trend in  $\chi$  against  $T$  can be mitigated by plotting  $\chi^T$  over  $T$ , and fitting either a exponential or power law relationship (Figure 4.7). I use the

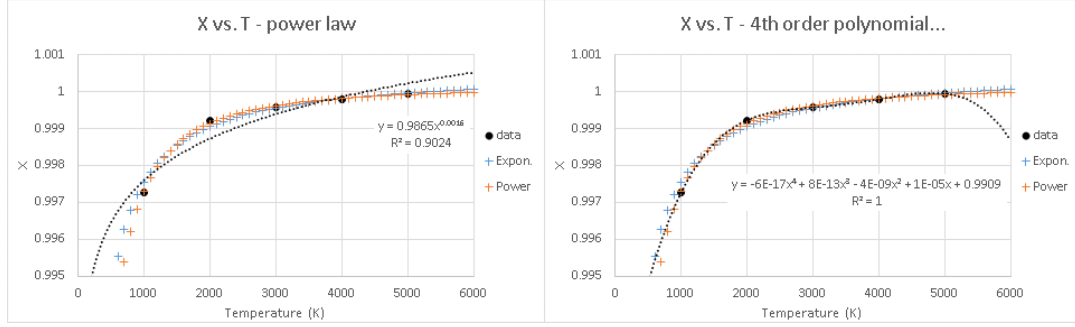


FIGURE 4.6: The fit  $\chi$  values plotted against  $T$ , with power law (LEFT/A.) and 4th order polynomial (RIGHT/B.) trendlines (both black). Blue and orange series are the exponential and power law fits obtained from plotting  $\chi^T/T$  (see Figure 4.7).

following power law-relationship,

$$\chi^T = AT^B, \quad (4.18)$$

where  $A$  is the coefficient and  $B$  is the exponent to be determined. The magnitudes of these fit parameters are  $3.468 \times 10^{-6}$  and 1.426 respectively. This fit represents the temperature-dependence better, both statistically and sensitivity-wise compared to an exponential relationship ( $\chi^T = Ae^{BT}$ ). The value of  $\chi^T$  at high  $T$  has a lesser effect on the conductivity-composition relationship than at low  $T$ , where the power law fit matches the data closer. In Figure 4.6, you can see that both the power law and exponential  $\chi^T$  over  $T$  relationships fit the data better than the  $\chi$  over  $T$  power law or polynomial relations.

#### 4.4.2 Why does this model work?

At this point, I have all the pieces in place to qualitatively describe how the equation for modelling a solid solution's thermal conductivity (Eq. 4.15) works and why. The first part is to scale a linearly interpolate the conductivity of two endmembers, at a given temperature, to the composition of interest. This ( $\kappa_V$ , Eq. 4.16) will be an overestimate of the true value, the conductivity is more complicated than a weighted average of the endmembers.

Increasing impurity mass difference and concentration (towards  $\sim 50\%$ ) increase the magnitude of point defect scattering. Mass difference is always constant in this study. Concentration varies, but as discrete values across the various temperatures.

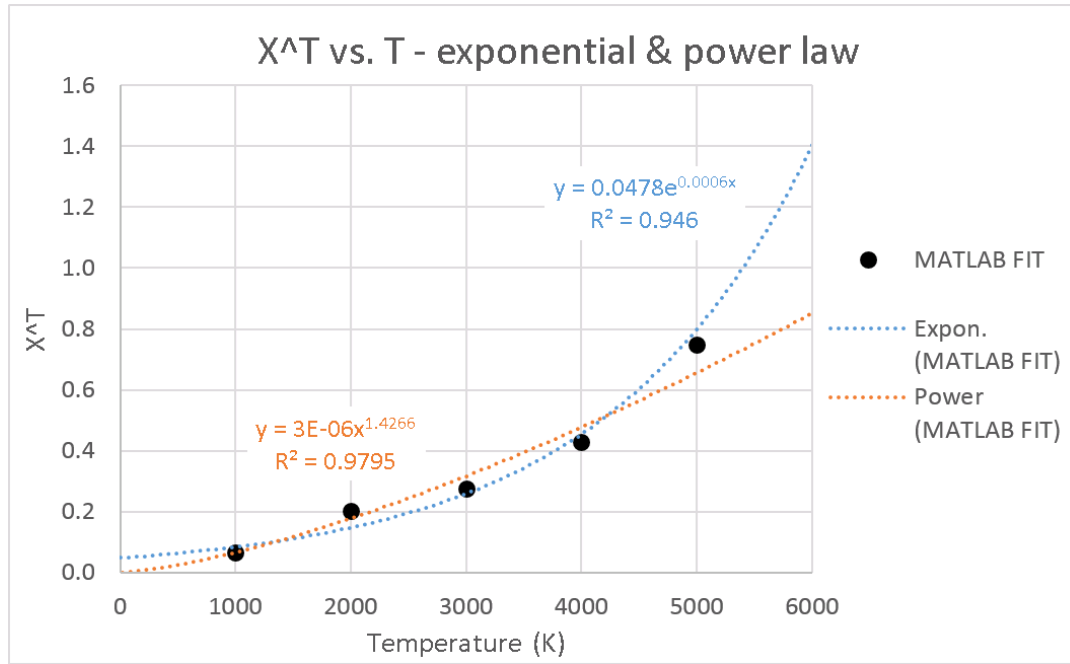


FIGURE 4.7: Exponential fit in blue (more curved), power law in orange (flatter)

For a given concentration at varying temperature, the mass difference and thus magnitude of point defect scattering is constant. Despite this, conductivity decrease due to adding impurities is not constant with varying temperature.

As temperature increases (through the range of conditions considered here) the magnitude of thermal/Umklapp scattering increases, tending to decrease conductivity (Figure. 4.3). The key thing in determining the effect of adding impurities is to consider the relative magnitudes of thermal scattering to defect scattering. As this ratio increases, with temperature, the significance of the defect scattering diminishes. An increase in thermal scattering reduces conductivity directly, but also reduces the change in conductivity associated with adding impurities.

This can be seen in Figure. 4.4, where the actual conductivity and curvature of the model fit decrease with temperature. “Curvature” in this sense can be measured by the area between the model and a straight line between endmembers. The model becomes more similar to the endmember line (area decrease) as temperature increases, as the effect of thermal scattering increases relative to defect scattering. An additional diagram is provided in Figure 4.8, showing how the

In the context of the model, the effect of this ratio is handled by the arctan segment of Eq. 4.15 (as alluded to in Figure. 4.2). The  $(\omega_0/\omega_D)$  term (Eq. 4.17) contains

the temperature and chemical ( $\chi$ ), and concentration (C) variables to control the scaling effect on  $\kappa_V$ .

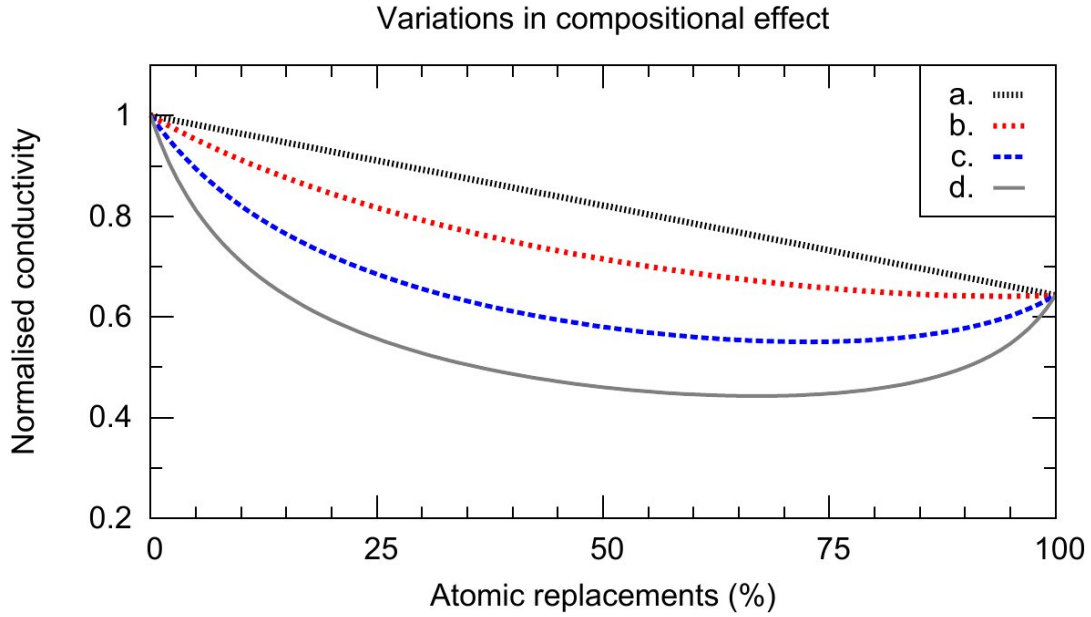


FIGURE 4.8: A graph showing how the relative magnitudes of defect and thermal scattering affect the resultant conductivity. Conductivity values are normalised to the maximum, the  $\text{MgSiO}_3$  value in this case. This figure does not show how the magnitude of conductivity variations with temperature, but the magnitude of conductivity changes from adding impurities.

a. shows the compositionally-weighted average of endmember conductivities. It represents the conductivity in absence of defect scattering, but with the addition of heavier Fe atoms having the effect of reducing conductivity.

d. represents conductivity if impurity scattering were to dominate over Umklapp processes. As with a., this series is hypothetical, and the physical result lies somewhere inbetween the two.

b. & c. represent a solid solution at hot and cold conditions respectively. b. would be found at a higher temperature, where increased thermal scattering reduces the significance of defect scattering. c. represents a colder condition with fewer Umklapp processes, where impurities are more relevant and there is a larger decrease relative to a., compared to the hot case (b.).

#### 4.4.3 Temperature dependence

The conductivities of  $\kappa_{\text{MgSiO}_3}$  and  $\kappa_{\text{FeSiO}_3}$  from Equation 4.16 can be scaled with temperature, giving an adjusted value

$$\kappa_{\text{adj}} = \kappa_{\text{ref}} \left( \frac{\rho}{\rho_{\text{ref}}} \right)^g \left( \frac{T_{\text{ref}}}{T} \right)^a. \quad (4.19)$$

$\rho$  is density,  $g$  and  $a$  are exponents which control the nature of the density and temperature-dependence, and “ref” denotes a reference value (Manthilake et al., 2011; Okuda et al., 2017). This equation is fit to the data, anchored around the values of the reference data point (the fit is shown in Figure 4.3). I fit to the data point at 1000 K, as the conductivities at higher temperatures become more similar, converging towards a minimum point. Anchoring to 1000 K reduces the error in the fit, on account of the relatively larger conductivity at this temperature.

For a given composition, the mass of the simulated system does not change with temperature. The number and type of atoms remains constant, while thermal effects cause density variations. The density relation in Equation 4.19 can be reformulated as

$$\frac{\rho}{\rho_{\text{ref}}} \equiv \frac{V_{\text{ref}}}{V}, \quad (4.20)$$

because  $\rho \propto V^{-1}$ , where  $V$  is the volume of the system in question. This leads to a modified version of Equation 4.19

$$\kappa_{\text{adj}} = \kappa_{\text{ref}} \left( \frac{V_{\text{ref}}}{V} \right)^g \left( \frac{T_{\text{ref}}}{T} \right)^a. \quad (4.21)$$

The exponent  $g$  (Manthilake et al., 2011) represents the rate of change of lattice thermal conductivity with density, at a constant temperature,

$$g = (\partial \ln \kappa_{\text{latt}} / \partial \ln \rho)_T. \quad (4.22)$$

The density/volume changes that I observe result from thermal effects, i.e. not at a constant temperature and not pressure-driven. The rate of change in conductivity with density in my data are better represented as something like

$$h \sim (\partial \ln \kappa_{\text{latt}} / \partial \ln \rho)_P, \quad (4.23)$$

where pressure ( $P$ ) is the condition kept constant. The significance here is that pressure-driven and temperature-driven density changes affect the conductivity differently. At constant temperature, conductivity and density increase with pressure.

The opposite is true at constant pressure for the material and temperatures considered here, conductivity and density decrease with increasing temperature. The result is  $g$  and  $h$  having opposite polarities based on the scenarios they describe.

Volume does not need to be an input variable for the model, as all the data are obtained from constant pressure (136 GPa) calculations and any volume variations relate to thermal expansion. I express the volume ratio shown in Equation 4.21 as

$$\frac{V_{\text{ref}}}{V(T)} \approx mT + c, \quad (4.24)$$

a simple linear function of temperature (see Figure 4.9), where  $m$  is the gradient and  $c$  the intercept (as you might expect).

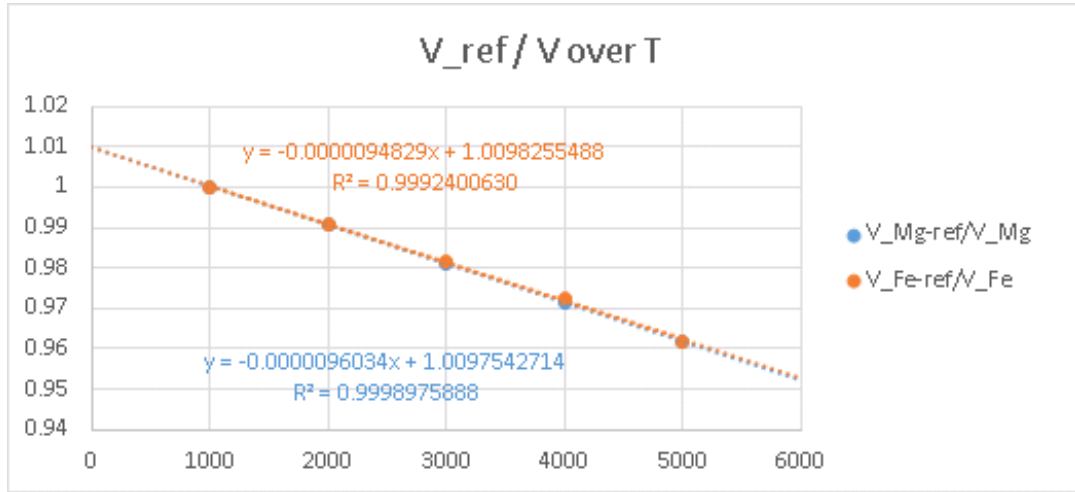


FIGURE 4.9:  $V_{\text{ref}}/V$  can be expressed as a simple linear function of  $T$ .

With Equation 4.24, I rewrite Equation 4.19 one more time,

$$\kappa_{\text{adj}} = \kappa_{\text{ref}} (mT + c)^h \left( \frac{T_{\text{ref}}}{T} \right)^a. \quad (4.25)$$

This equation allows me to obtain a conductivity value at any temperature within the fit range, comprising a reference conductivity and temperature for the material in question, with constants ( $m$ ,  $c$ ,  $h$ , &  $a$ , see Table 4.3) fit to data across a range of temperatures. This scaling process is necessary to obtain  $\kappa_{\text{MgSiO}_3}$  and  $\kappa_{\text{FeSiO}_3}$ , which have their own reference values and fit constants, for use in Eq. 4.16.

TABLE 4.3: Mg and Fe refer to  $\text{MgSiO}_3$  and  $\text{FeSiO}_3$  endmembers, SS the solid solution with a 50% mix.

	Composition		
	Mg	SS	Fe
$\kappa_{ref}$	17.51	8.26	11.26
$h$	-10.93	-5.52	-17.32
$a$	0.896	0.428	0.913
$m$	-9.60E-06	-9.47E-06	-9.48E-06
$c$	1.00975	1.00965	1.00983

## 4.5 Discussion

### 4.5.1 Significance of mass and atomic interactions on the iron potential

I believe mass is the most important thing for the magnitude of phonon-defect scattering. I am to prove this by running calculations where the mass of the impurities are kept the same as Mg, only changing their potential to match my fitted Mg-Fe interaction. I predict conductivity will be largely unchanged with varying composition.

Figure 4.10 shows the Green-Kubo conductivity results as a function as composition for 1000 and 4000 K, with the model fit to data. The other partial series represent a partial potential compared to the one I used, one where the iron impurities only have the correct mass (the isotopic model, akin to Ammann et al. (2014)), the other with my calibrated Fe-O pair potential but the Mg mass. The isotopic atomic model is much closer to the results of the full model than the potential model. Both atomic masses and chemical potential play a roll in determining the interaction, albeit mass is more significant.

### 4.5.2 Backcalculating mean free path

The conductivities from supercells ( $\kappa_L$ ) of varying length ( $L$ ) obtained via direct method calculations fit the form

$$\frac{1}{\kappa_L} = \left[ \frac{12}{C_v v} \right] \frac{1}{L} + \left[ \frac{3}{C_v v} \frac{1}{\Lambda_{\text{ph-ph}}} \right], \quad (4.26)$$

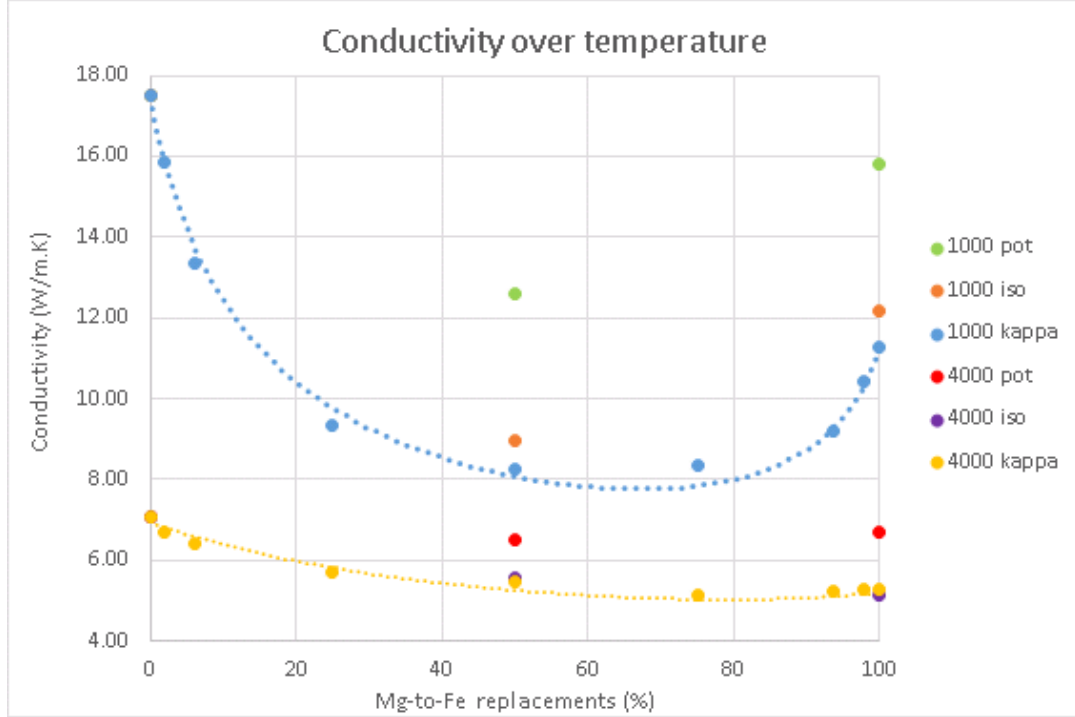


FIGURE 4.10: Green-Kubo conductivity results and model fits for 1000 K and 4000 K. The Fe in these series have the correct atomic mass, and the calibrated interatomic potential. The partial series show how conductivity changes when the atomic interactions are altered. Changing the atomic mass (i.e. Fe effectively becomes a heavy Mg isotope) produces small variation in conductivity result. Changing the interatomic potential but not the mass (i.e. an incredibly light Fe isotope) alters the result drastically.

where  $C_v$  is the volumetric isochoric heat capacity,  $v$  is the phonon group velocity, and  $\Lambda_{\text{ph-ph}}$  is the mean free path associated with phonon-phonon scattering (modified from Schelling et al., 2002, via Stackhouse and Stixrude, 2010). When the inverse conductivities are plotted against the inverse cell lengths, extrapolation to the y-axis ( $1/L = 0$ ) gives the bulk material ( $L \rightarrow \infty$ ) conductivity, and its associated phonon mean free path. The two square-bracketed terms in the above equation represent the gradient and intercept respectively, of such a line fit to data and extrapolated (as in Figure 2.5).

I can rewrite Equation 4.26 with the following simplifications

$$M = \left[ \frac{12}{C_v v} \right], \text{ and } \frac{M}{4} = \frac{3}{C_v v},$$

giving

$$\frac{1}{\kappa_L} = M \frac{1}{L} + \left[ \frac{M}{4} \frac{1}{\Lambda_{\text{ph-ph}}} \right]. \quad (4.27)$$



When  $1/L = 0$ , the extrapolated conductivity can be equated to the gradient and effective mean free path

$$\frac{1}{\kappa} = \frac{M}{4} \frac{1}{\Lambda},$$

and thus

$$\Lambda = \frac{M}{4} \kappa. \quad (4.28)$$

Using the gradient and conductivity from direct method calculations at 136 GPa, 4000 K, and a supercell cross-sectional area of  $12 \times 12$ , the mean free path is equal to  $0.23 \pm 0.03$  nm. This value is roughly half the width of the unit cell in the  $a/x$ -direction, or the width of a direct method temperature section.

### 4.5.3 Scaling MFP to quantify phonon-defect scattering

This MFP value is obtained from a conductivity representative of bulk  $\text{MgSiO}_3$  bridgmanite, therefore I can assume it is the effective MFP in the absense of phonon-defect or phonon-boundary scattering (Matthiessen's rule, recall Equation 1.3). MFP is directly proportional to conductivity (Equation 4.28), therefore I propose scaling the 4000 K GK conductivity results to quantify the phonon-defect scattering associated with adding iron. When considering the effect of impurities on conductivity, the effective MFP depends on phonon-phonon and phonon-defect interactions

$$\frac{1}{\Lambda} = \frac{1}{\Lambda_{\text{ph-ph}}} + \frac{1}{\Lambda_{\text{ph-d}}}. \quad (4.29)$$

The MFP determined from the direct method extrapolation can be matched with the equivalent 0% Fe, 4000 K Green-Kubo result on Figure 4.4. If  $7.07 \text{ Wm}^{-1}\text{K}^{-1}$  is proportional to an effective MFP of 0.23 nm, I can scale this MFP value by the  $\text{MgSiO}_3$  endmember-normalised conductivities (see Figure 4.11).

I make the assumption that the data points/curve of Figure 4.11 represent the effective MFP, and that the linear interpolation between endmembers the phonon-phonon scattering MFP. The interpolated conductivities do not capture the non-linear effects of defect scattering, at constant temperature the change in conductivity is proportional to the change in mass associated with changing Mg to Fe.

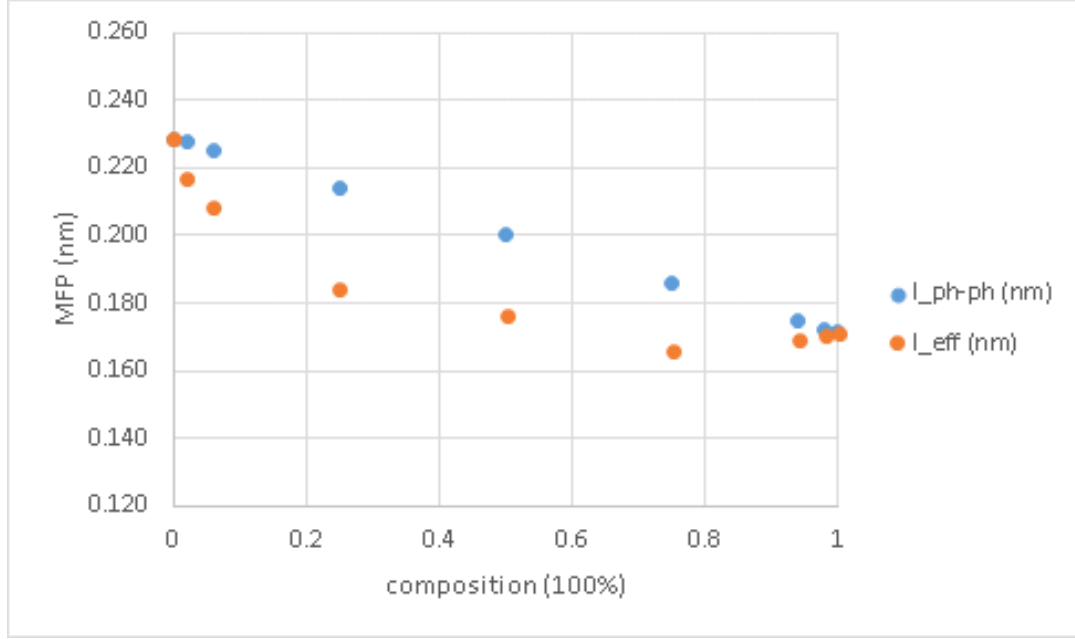


FIGURE 4.11: GK conductivity results from 4000 K, scaled to the MFP determined from analysis of direct method results. The linear interpolation between endmembers gives the MFP of phonon-phonon scattering, which decreases as Fe is introduced and the mass of the system increases.

The deficit between computed and interpolated conductivity can be imagined as phonon-defect contribution to  $\Lambda$ , the bigger the gap at a given composition, the greater significance of  $\Lambda_{\text{ph-d}}$ . I will obtain the phonon-defect MFP by subtracting the inverse of the two, as in

$$\frac{1}{\Lambda_{\text{ph-d}}} = \frac{1}{\Lambda} - \frac{1}{\Lambda_{\text{ph-ph}}} . \quad (4.30)$$

Table 4.4 shows how properties change across the range of compositions studied. The results are the computed conductivity, the interpolated conductivity as a function of composition, this difference between this two value, and the conductivity result normalised. This conductivity is then converted to a mean-free path value as discussed earlier, as is the interpolated conductivity to obtain my proxy for phonon-phonon scattering MFP. I then calculate the phonon-defect scattering MFP as in Equation 4.29. This value is then inverted and normalised, showing relative significance of scattering as conductivity varies.

If the mean free path is the distance between scattering events, then the inverse (as presented in Equation 4.30) is the amount of scattering events per unit distance.

The total number of scattering events combines the number of phonon-phonon and phonon-defect collisions, as shown for 4000 K and 1000 K respectively in Figures 4.12 & 4.13. Where phonon-phonon scattering is high because of 4000 K temperature, impurity scattering influences, but is not the dominant control on the magnitude of scattering. This behaviour is different at 1000 K, where the effect of phonon-defect scattering is of comparable magnitude to the decreased phonon-phonon scattering for high impurity contents (i.e. around 50%). The largest phonon-defect scattering coincides with the largest difference between computed and interpolated conductivity, as you might expect.

#### 4.5.4 $C(1 - C)$ model limitations

Using this method to determine  $\Lambda_{\text{ph-d}}$ , I am able to observe how its magnitude changes with composition. Table 4.4 has two group of rows, one with conductivity data points as computed, the other with the model predictions at the same compositions. When the data is used to determine  $\Lambda_{\text{ph-d}}$ , the greatest effect is at a composition between 25% and 50% (albeit closer to 25%).

Taking the 4000 K conductivity model however, the largest effect of phonon-defect scattering (smallest MFP) is at a composition around 50% (see Figure 4.14). This is to be expected, and is set by the  $C(1 - C)$  term in Equation 4.17. The  $C(1 - C)$  model is assuming that an equal proportion of each type of atom (i.e. 50/50 composition) creates the most phonon-defect scattering, but I suggest it is weighted by the masses of the atoms in question (which is captured in the data). The composition at which the mass contribution is equal can be calculated by

$$C_{\text{mass}} = \frac{A_{\text{Mg}}}{A_{\text{Mg}} + A_{\text{Fe}}} , \quad (4.31)$$

where  $A$  is atomic mass, Mg corresponds to  $C = 0$  and Fe to  $C = 1$ . For Mg and Fe,  $C_{\text{mass}} = 0.3$ , or 30% Fe to 70% Mg (see Figure 4.15). 30 Fe atoms weigh the same as 70 Mg atoms, which I believe to be the turning point in phonon-defect scattering. Defect scattering increases from zero up to its maximum at this composition, and decreases to zero as Fe content tends towards 100%. Even if conductivity/MFP

---

decreases overall due to phonon-phonon scattering effects with increasing temperature, this composition will be the point of minimum  $\Lambda_{\text{ph-d}}$  or maximum phonon-defect scattering.



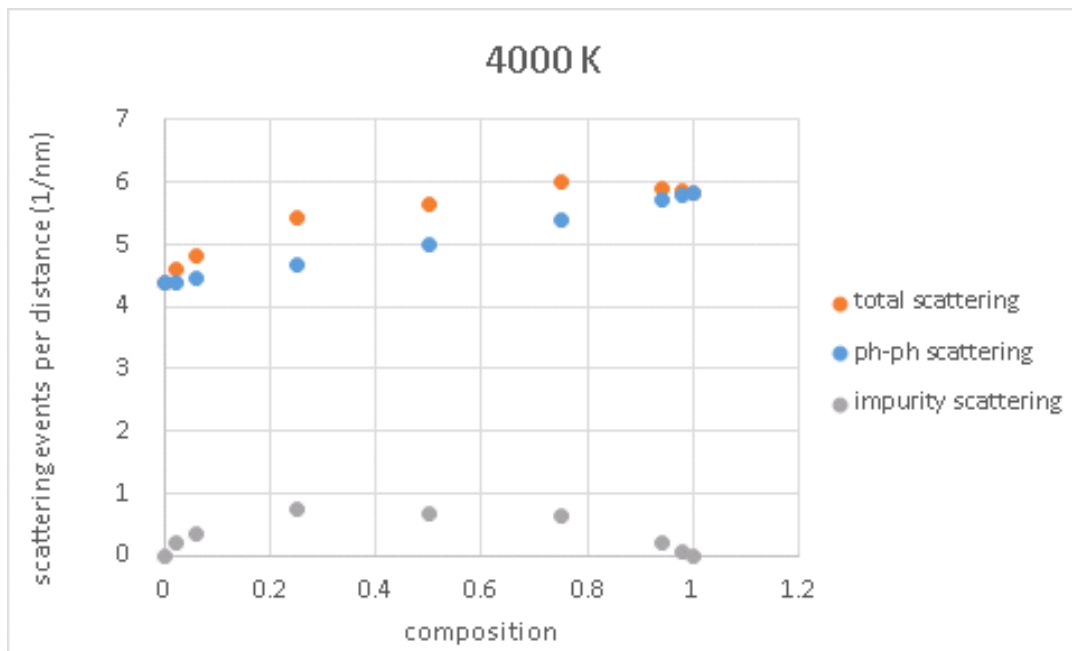


FIGURE 4.12: The scattering event frequency, or inverse of MFP, plotted against composition at 4000 K. The total scattering behaves like the inverse of the conductivity. Phonon-phonon scattering increases with composition, as the mass of the system increases. Phonon-defect scattering increases from each endmember, to a maximum point at an intermediate composition. The ph-ph scattering is high compared to ph-d, the 4000 K temperature dominates the MFP behaviour.

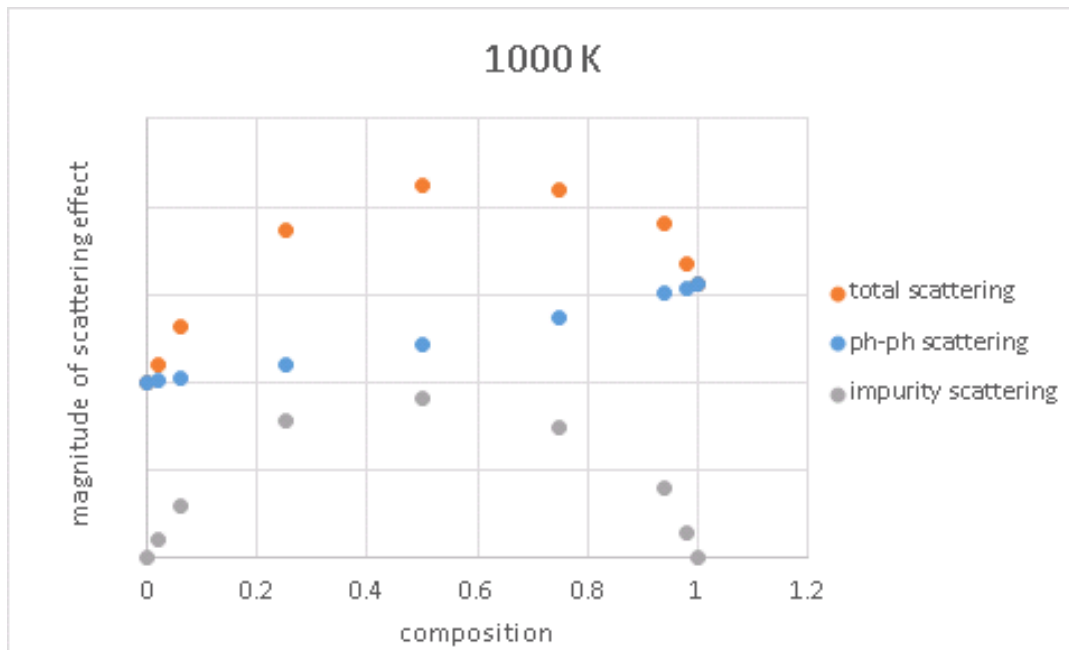


FIGURE 4.13: An illustrative measure of scattering significance, plotted against composition at 1000 K. The total scattering behaves like the inverse of the conductivity. Phonon-phonon scattering increases with composition, as the mass of the system increases. Phonon-defect scattering increases from each endmember, to a maximum point at an intermediate composition. While the magnitude of phonon-defect scattering is similar to that at 4000 K, ph-ph scattering is smaller due to the lower temperature. The relative significance of ph-d increases, meaning impurities have a greater effect on the conductivity.

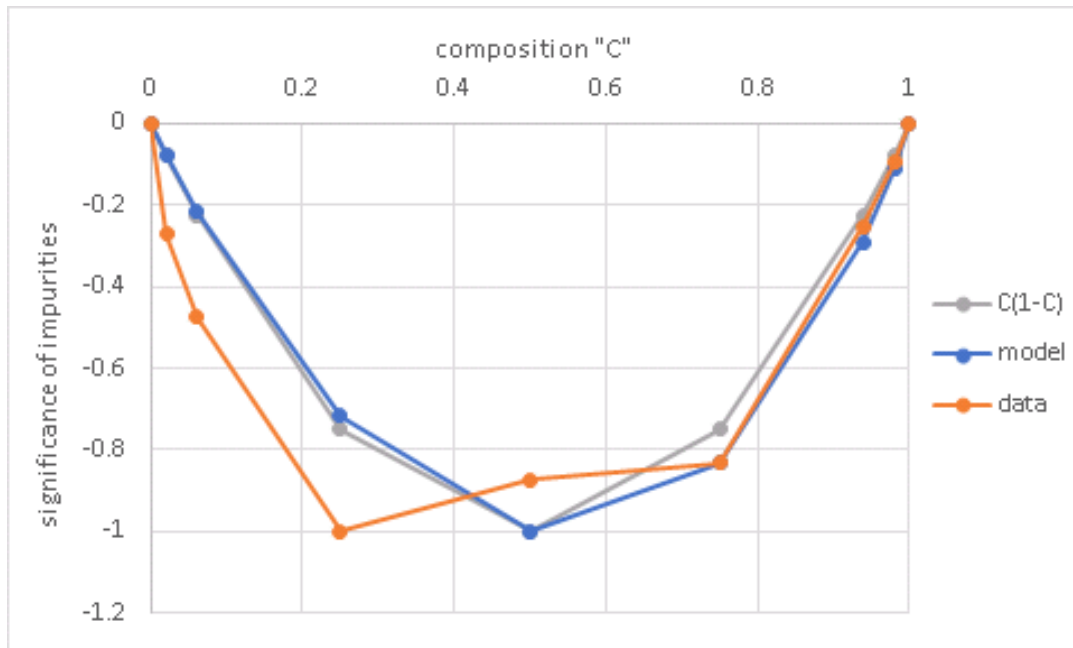


FIGURE 4.14: An illustration of how the significance of ph-d scattering changes with composition depending on the data. Determining the ph-d MFP from the model gives a result similar to  $C(1 - C)$ , as you might expect (not exactly though, error is introduced by the model not being fixed to the endmembers). However the data shows that the largest effect of defects is between 25% and 50%, presumably closer to 25%.

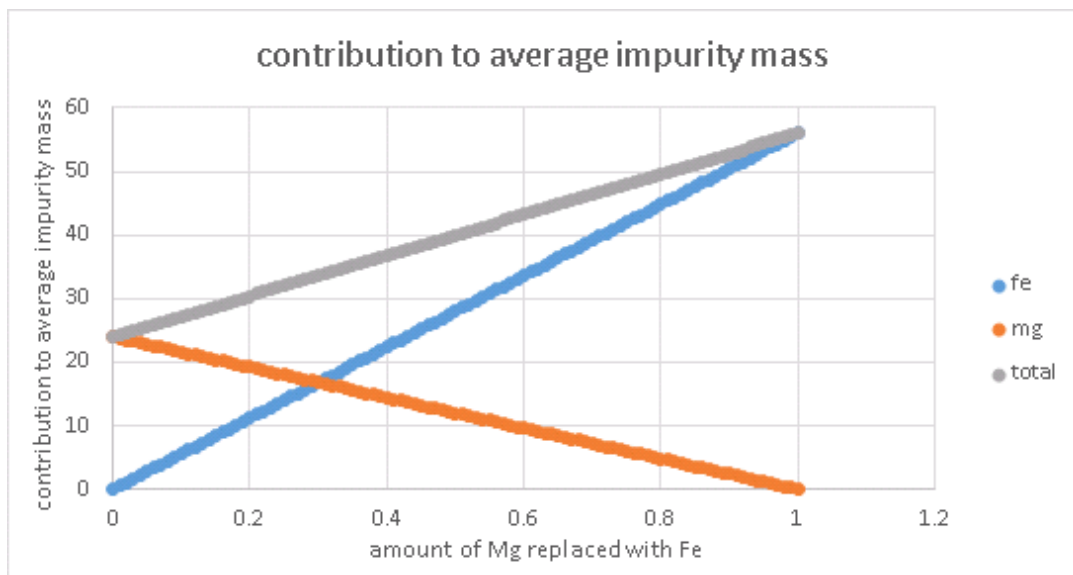


FIGURE 4.15: An illustration of contributions to the average mass of all Mg and Fe in the system. They contribute equally when 30% of Mg is replaced with Fe.



## Chapter 5

# Using STUFF to do THINGS

### 5.1 Draft words

I am able to construct a model of lower mantle heat flux, including the effect of LLSVP properties. Using LEMA, I specify a CMB base condition, and a TBL condition at some height above it. In all models I consider, the CMB will be isothermal. The TBL will have a variable mean temperature, and regions of higher and lower temperature. The lower mantle has an average Fe%, but the LLSVPs are enriched compared the depleted surrounding bulk lower mantle. By varying the temperature and composition at the CMB, conductivity can be altered using the model from PREVIOUS-REF. The difference in temperature between CMB and TBL, and the undulations on the latter, control the lower mantle temperature gradient.

Heat flux can be calculated using conductivity and temperature gradient via FOURIER'S LAW. While the magnitude of the heat flux will change with parameters, perhaps more interesting is the lateral variation of this parameter. This will show how the lower mantle heat flux is sensitive to the conditions therein, and what condition or combination of conditions is most significant. The results from these calculations can then be compared to observables, dismissing scenarios which are unfeasible or unstable. There are many variables in the lower mantle, and observables to compare to. The variable conductivities from this work will play an important role in constraining CMB heat flux.

I can use spherical harmonics to generate structures that resemble LLSVPs. The centre of LLSVPs are approximately(/loosely?) located on the equator, antipodal

at  $0^\circ$  and  $180^\circ$  longitude (the African and Pacific LLSVPs respectively). A first order approximation for this geometry is the spherical harmonic  $Y_2^2$ , four quadrants of varying polarity around the polar axis. This looks good, but the projection is misleading in that it actually extends to the poles. It can be improved by stacking  $Y_2^0$  on top of it, enhancing regions on the equator and reducing everything towards the poles. The results is two circular patterns, each located at opposite sides of the equator.

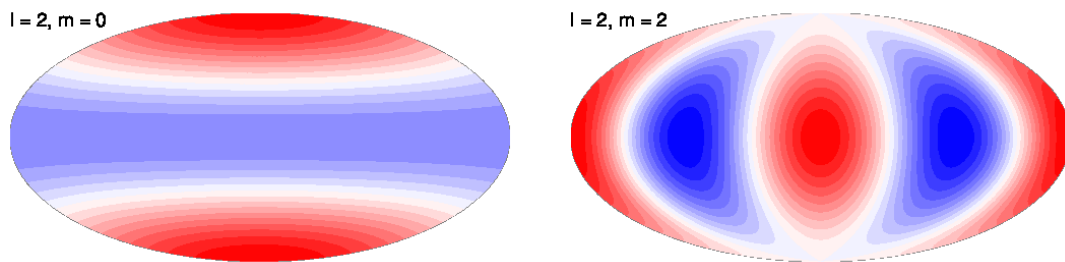


FIGURE 5.1: Source: <http://www-udc.ig.utexas.edu/external/becker/teaching-sh.html>  
These two harmonics are added together, amplifying blue regions on the equator, and diminishing everything else.

For the  $Y_2^2$  pattern, the areas of positive and negative amplitude regions are equal. For the  $Y_2^0$ -combined model, the distribution of polarities is not even. By the way something like temperature is set up in the model, having a mean value with a “ $\pm$ ” range leads to hotter hots, and warmer colds. There is more of the cold, surrounding mantle compared to LLSVP-designated regions, the LLSVPs have to be hotter than the surrounding mantle is colder.

Conductivity cannot be probed from the surface, but seismic velocities can be inferred from tomography. The same processes that affect conductivity generally affect shear wave velocity in the same fashion, be it increase or decrease. I can use  $V_S$  observations as an analogue to make inferences about the lower mantle.

When conductivity is kept constant across the whole CMB, variations in heat flux are determined solely by the lower mantle temperature profile. The reverse is also true, with constant temperature gradient above the CMB, conductivity controls lateral heat flow variations. This is a vast oversimplification, just talking about possible endmembers, in reality there will be both temperature and compositional factors affecting heat flux. Conductivity itself is temperature-dependent, further tying the

two variables together.

When modelling LLSVPs, we are assuming they are thermochemical piles, that they are hotter and denser (e.g. high Fe%) than the surrounding lower mantle. Increasing temperature reduces conductivity, as does increasing impurity inclusion. By modelling LLSVPs as purely thermal piles (i.e. increasing their temperature), we see a reduction in heat flux. This flux is further reduced when Fe content is increased, as conductivity decreases with impurity content. By altering temperature and composition in tandem, I will be able to suggest sets of lower mantle conditions which reproduce observations.

While this model is of dubious use in constraining the exact nature of CMB heat flux, inferences can be made on the relative variations laterally. How much heat is impeded passing through a LLSVP? How extreme do temperature and compositional variations need to be to significantly affect the distribution of heat flow? An important parameter will be that of the lateral variation in heat flux

$$q^* = \frac{q_{\max} - q_{\min}}{q_{\text{mean}}} , \quad (5.1)$$

where max and min refer to the calculated extremes, and mean the average over the whole CMB. The larger the value of  $q^*$ , the smaller the heat flux through the LLSVPs. While the magnitudes of heat flux may not be accurate, using  $q^*$  will let me make comments on thermal conductivity's role in the Earth heat engine for a wide range of possible lower mantle conditions.

### 5.1.1 Notes

#### VARIABLES TO PLAY WITH

Temp-cmb, Temp-tbl, Temp-diff, Temp-hot, Temp-cold,

Height-tbl, Height-llsvp (peak height, how is shape considered, sph. harm.?)

Comp-mean, Comp-lm, Comp-llsvp,

The things I can vary are temperature, composition, and TBL thickness. Temperature and thickness amount to the same thing in the model however, which is the thermal gradient.

Temperature variations are set at the top of the model (1000 km above CMB). The temperature is constant all the way down to the TBL, at which it increases up to the CMB temperature. I only need to plot the temperature gradient at the CMB. WHAT IS THE POINT OF THE TBL THEN? OR RATHER, WHAT IS THE POINT OF MANTLE ABOVE THE TBL?

In the real world, Fe may be localised. in the model, it is constant radially up.

I need to fiddle with parameters to obtain realistic change in shear velocity. I can then record this and  $q^*$  "about 2% shear wave anomaly" - vary temp to get this, then comp, then both

Changing temperature at the top of the model changes gradient. Changing temperature at the bottom also changes conductivity.

Keep the top around 1000 K cooler?

Turn notebook into function with input arguments, then run in a loop.

Investigate thermo mantle, chemical mantle, and then thermochemical. How sensible are these models? How feasible are they?

Lateral temperature variations are different to radial variations!

use model to link tomography

what range could  $q^*$  occupy, and why would jon and chris care?

PLAN

Refresh LLSVP theory

Ask question about how conductivity can affect heat flux and the lower mantle generally. "given what we now know about the effect of T and Fe on K, can we say what these models imply for CMB heat flux?"

Introduce heat flux and the lateral variation. "for Q and  $q^*$ , what is it, what do we know, what does it mean?"

LEMA - what is, why am i using it, how does it work "i will use LEMA to explore" - numerical tests

CHEBYSHEVYS related to LEMA section? -numerical tests "1D CMB heat flux"

Future work / conclusion / caveats / limitations. i am only using bridgmanite, future work would be to add MgO

## Chapter 6

# Summary/Discussion/Conclusion

### 6.1 Main Section 1

Lorem ipsum dolor sit amet, consectetur adipiscing elit. Aliquam ultricies lacinia euismod. Nam tempus risus in dolor rhoncus in interdum enim tincidunt. Donec vel nunc neque. In condimentum ullamcorper quam non consequat. Fusce sagittis tempor feugiat. Fusce magna erat, molestie eu convallis ut, tempus sed arcu. Quisque molestie, ante a tincidunt ullamcorper, sapien enim dignissim lacus, in semper nibh erat lobortis purus. Integer dapibus ligula ac risus convallis pellentesque.

#### 6.1.1 Subsection 1

Nunc posuere quam at lectus tristique eu ultrices augue venenatis. Vestibulum ante ipsum primis in faucibus orci luctus et ultrices posuere cubilia Curae; Aliquam erat volutpat. Vivamus sodales tortor eget quam adipiscing in vulputate ante ullamcorper. Sed eros ante, lacinia et sollicitudin et, aliquam sit amet augue. In hac habitasse platea dictumst.



## Appendix A

# Frequently Asked Questions

### A.1 How do I change the colors of links?

The color of links can be changed to your liking using:

```
\hypersetup{urlcolor=red}, or  
\hypersetup{citecolor=green}, or  
\hypersetup{allcolor=blue}.
```

If you want to completely hide the links, you can use:

```
\hypersetup{allcolors=.}, or even better:  
\hypersetup{hidelinks}.
```

If you want to have obvious links in the PDF but not the printed text, use:

```
\hypersetup{colorlinks=false}.
```





# Bibliography

- Alfè, D., M. J. Gillan, and G. D. Price (2007). "Temperature and composition of the Earth's core". In: *Contemp. Phys.* 48.2, pp. 63–80. ISSN: 00107514. DOI: [10.1080/00107510701529653](https://doi.org/10.1080/00107510701529653).
- Allègre, C. J. et al. (1995). "The chemical composition of the Earth". In: *Earth Planet. Sci. Lett.* 134, pp. 515–526. ISSN: 14684004. DOI: [10.1093/astrogeo/atv065](https://doi.org/10.1093/astrogeo/atv065).
- Ammann, M. W. et al. (2014). "Variation of thermal conductivity and heat flux at the Earth's core mantle boundary". In: *Earth Planet. Sci. Lett.* 390, pp. 175–185. ISSN: 0012821X. DOI: [10.1016/j.epsl.2014.01.009](https://doi.org/10.1016/j.epsl.2014.01.009). URL: <http://linkinghub.elsevier.com/retrieve/pii/S0012821X14000120>.
- Balandin, A. A. et al. (2008). "Superior thermal conductivity of single-layer graphene." In: *Nano Lett.* 8.3, pp. 902–907. ISSN: 1530-6984. DOI: [10.1021/nl0731872](https://doi.org/10.1021/nl0731872). URL: <http://www.ncbi.nlm.nih.gov/pubmed/18284217>.
- Brodholt, J. P. (2000). "Pressure-induced changes in the compression mechanism of aluminous perovskite in the Earth's mantle". In: *Nature* 407.6804, pp. 620–622. ISSN: 00280836. DOI: [10.1038/35036565](https://doi.org/10.1038/35036565).
- Brown, J. M. (1986). "Interpretation of the D" zone at the base of the mantle: dependence on assumed values of thermal conductivity". In: *Geophys. Res. Lett.* 13.13, pp. 1509–1512.
- Chen, Y. et al. (2012). "Critical assessment of classical potentials for MgSiO<sub>3</sub> perovskite with application to thermal conductivity calculations". In: *Phys. Earth Planet. Inter.* 210-211, pp. 75–89. ISSN: 00319201. DOI: [10.1016/j.pepi.2012.08.002](https://doi.org/10.1016/j.pepi.2012.08.002). URL: <http://linkinghub.elsevier.com/retrieve/pii/S0031920112001483>.
- Dalton, D. A. et al. (2013). "Effect of mass disorder on the lattice thermal conductivity of MgO periclase under pressure." In: *Sci. Rep.* 3, pp. 2400–2405. ISSN: 2045-2322. DOI: [10.1038/srep02400](https://doi.org/10.1038/srep02400). URL: <http://www.pubmedcentral.nih.gov/>

`articlerender.fcgi?artid=3739002{\&}tool=pmcentrez{\&}rendertype=abstract.`

- Dekura, H., T. Tsuchiya, and J. Tsuchiya (2013). "Ab initio lattice thermal conductivity of MgSiO<sub>3</sub> perovskite as found in Earth's lower mantle". In: *Phys. Rev. Lett.* 110, pp. 1–5. ISSN: 0031-9007. DOI: [10.1103/PhysRevLett.110.025904](https://doi.org/10.1103/PhysRevLett.110.025904). URL: <http://link.aps.org/doi/10.1103/PhysRevLett.110.025904>.
- Dobson, D. P. and J. P. Brodholt (2005). "Subducted banded iron formations as a source of ultralow-velocity zones at the core-mantle boundary". In: *Nature* 434, pp. 371–374. DOI: [10.1038/nature03385](https://doi.org/10.1038/nature03385).
- Dong, H. et al. (2018). "Equivalence of the equilibrium and the nonequilibrium molecular dynamics methods for thermal conductivity calculations: From bulk to nanowire silicon". In: *Phys. Rev. B* 97.9, pp. 1–8. ISSN: 24699969. DOI: [10.1103/PhysRevB.97.094305](https://doi.org/10.1103/PhysRevB.97.094305).
- Dubuffet, F. and D. A. Yuen (2000). "A thick pipe-like heat-transfer mechanism in the mantle: Nonlinear coupling between 3-D convection and variable thermal conductivity". In: *Geophys. Res. Lett.* 27, pp. 17–20. URL: <http://onlinelibrary.wiley.com/doi/10.1029/1999GL008338/full>.
- Gale, J. D. (1997). "GULP: A computer program for the symmetry-adapted simulation of solids". In: *J. Chem. Soc.* 93, pp. 629–637.
- Garnero, E. J. and A. K. McNamara (2008). "Structure and dynamics of Earth's lower mantle". In: *Science* (80-. ). 320, pp. 626–629. URL: <http://www.sciencemag.org/content/320/5876/626.short>.
- Ghaderi, N. et al. (2017). "Lattice Thermal Conductivity of MgSiO<sub>3</sub> Perovskite from First Principles". In: *Sci. Rep.* 7.1, pp. 1–9. ISSN: 2045-2322. DOI: [10.1038/s41598-017-05523-6](https://doi.org/10.1038/s41598-017-05523-6). URL: <http://dx.doi.org/10.1038/s41598-017-05523-6>.
- Goncharov, A. F. et al. (2008). "Radiative conductivity in the Earth's lower mantle." In: *Nature* 456, pp. 231–234. ISSN: 1476-4687. DOI: [10.1038/nature07412](https://doi.org/10.1038/nature07412). URL: <http://www.ncbi.nlm.nih.gov/pubmed/19005553>.
- Goncharov, A. F. et al. (2009). "Thermal conductivity of lower-mantle minerals". In: *Phys. Earth Planet. Inter.* 174, pp. 24–32. ISSN: 00319201. DOI: [10.1016/j.pepi.2008.07.033](https://doi.org/10.1016/j.pepi.2008.07.033). URL: <http://linkinghub.elsevier.com/retrieve/pii/S0031920108001945>.

- Green, M. S. (1954). "Markoff random processes and the statistical mechanics of time-dependent phenomena. II. Irreversible processes in fluids". In: *J. Chem. Phys.* 22.3, pp. 398–413. ISSN: 00219606. DOI: [10.1063/1.1740082](https://doi.org/10.1063/1.1740082).
- Gubbins, D., A. P. Willis, and B. Sreenivasan (2007). "Correlation of Earth's magnetic field with lower mantle thermal and seismic structure". In: *Phys. Earth Planet. Inter.* 162, pp. 256–260. ISSN: 00319201. DOI: [10.1016/j.pepi.2007.04.014](https://doi.org/10.1016/j.pepi.2007.04.014). URL: <http://linkinghub.elsevier.com/retrieve/pii/S0031920107000908>.
- Haigis, V., M. Salanne, and S. Jahn (2012). "Thermal conductivity of MgO, MgSiO<sub>3</sub> perovskite and post-perovskite in the Earth's deep mantle". In: *Earth Planet. Sci. Lett.* 355-356, pp. 102–108. ISSN: 0012821X. DOI: [10.1016/j.epsl.2012.09.002](https://doi.org/10.1016/j.epsl.2012.09.002). URL: <http://linkinghub.elsevier.com/retrieve/pii/S0012821X12004815>.
- Hofmeister, A. M. (1999). "Mantle values of thermal conductivity and the geotherm from phonon lifetimes". In: *Science* (80-. ). 283, pp. 1699–1706. ISSN: 00368075. DOI: [10.1126/science.283.5408.1699](https://doi.org/10.1126/science.283.5408.1699). URL: <http://www.sciencemag.org/cgi/doi/10.1126/science.283.5408.1699>.
- Horai, K. (1971). "Thermal conductivity of rock-forming minerals". In: *Earth Planet. Sci. Lett.* 76.5, pp. 359–368. ISSN: 0012821X. DOI: [10.1016/0012-821X\(69\)90186-1](https://doi.org/10.1016/0012-821X(69)90186-1).
- Howell, P. C. (2012). "Comparison of molecular dynamics methods and interatomic potentials for calculating the thermal conductivity of silicon." In: *J. Chem. Phys.* 137.22, p. 224111. ISSN: 1089-7690. DOI: [10.1063/1.4767516](https://doi.org/10.1063/1.4767516). URL: <http://www.ncbi.nlm.nih.gov/pubmed/23248991>.
- Hu, L., W. J. Evans, and P. Keblinski (2011). "One-dimensional phonon effects in direct molecular dynamics method for thermal conductivity determination". In: *J. Appl. Phys.* 110.11, p. 113511. ISSN: 00218979. DOI: [10.1063/1.3660234](https://doi.org/10.1063/1.3660234). URL: <http://scitation.aip.org/content/aip/journal/jap/110/11/10.1063/1.3660234>.
- Keppler, H. et al. (2008). "Optical absorption and radiative thermal conductivity of silicate perovskite to 125 gigapascals". In: *Science* (80-. ). 322, pp. 1529–1532. URL: <http://www.sciencemag.org/content/322/5907/1529.short>.

- Klemens, P. G. (1959). "Deviation from Matthiessen's rule and lattice thermal conductivity of alloys". In: *Aust. J. Phys.* 12.2, pp. 199–202. ISSN: 0004-9506. DOI: [10.1071/ph590199](https://doi.org/10.1071/ph590199).
- (1960). "Thermal resistance due to point defects at high temperatures". In: *Phys. Rev.* 119.2, pp. 507–509. ISSN: 0031-899X. DOI: [10.1103/PhysRev.119.507](https://doi.org/10.1103/PhysRev.119.507). URL: <http://link.aps.org/doi/10.1103/PhysRev.119.507>.
- Koker, N. de (2009). "Thermal conductivity of MgO periclase from equilibrium first principles molecular dynamics". In: *Phys. Rev. Lett.* 103.12, pp. 1–4. DOI: [10.1103/PhysRevLett.103.125902](https://doi.org/10.1103/PhysRevLett.103.125902).
- Kubo, R. (1957). "Statistical-mechanical theory of irreversible processes. I." In: *J. Phys. Soc. Japan* 12.6, pp. 570–586. DOI: [10.1143/JPSJ.12.570](https://doi.org/10.1143/JPSJ.12.570).
- (1966). "The fluctuation-dissipation theorem". In: *Rep. Prog. Phys.* 29.1, p. 255. ISSN: 00319007.
- Lay, T. et al. (2006). "A post-perovskite lens and D'' heat flux beneath the central Pacific." In: *Science* (80-. ). 314, pp. 1272–1276. ISSN: 1095-9203. DOI: [10.1126/science.1133280](https://doi.org/10.1126/science.1133280). URL: <http://www.ncbi.nlm.nih.gov/pubmed/17124317>.
- Lay, T., J. Hernlund, and B. A. Buffett (2008). "Core–mantle boundary heat flow". In: *Nat. Geosci.* 1, pp. 25–32. ISSN: 1752-0894. DOI: [10.1038/ngeo.2007.44](https://doi.org/10.1038/ngeo.2007.44). URL: <http://www.nature.com/doifinder/10.1038/ngeo.2007.44>.
- Lee, D. et al. (1995). "Thermal characterization of carbon-opacified silica aerogels". In: *J. Non. Cryst. Solids* 186, pp. 285–290. ISSN: 00223093. DOI: [10.1016/0022-3093\(95\)00055-0](https://doi.org/10.1016/0022-3093(95)00055-0). URL: <http://linkinghub.elsevier.com/retrieve/pii/0022309395000550>.
- Lee, K. K. M. et al. (2004). "Equations of state of the high-pressure phases of a natural peridotite and implications for the Earth's lower mantle". In: *Earth Planet. Sci. Lett.* 223, pp. 381–393. ISSN: 0012821X. DOI: [10.1016/j.epsl.2004.04.033](https://doi.org/10.1016/j.epsl.2004.04.033).
- Lobanov, S. S. et al. (2017). "Radiative conductivity and abundance of post-perovskite in the lowermost mantle". In: *Earth Planet. Sci. Lett.* 479, pp. 43–49. ISSN: 0012821X. DOI: [10.1016/j.epsl.2017.09.016](https://doi.org/10.1016/j.epsl.2017.09.016). URL: <http://dx.doi.org/10.1016/j.epsl.2017.09.016>.
- Manthilake, G. M. et al. (2011). "Lattice thermal conductivity of lower mantle minerals and heat flux from Earth's core." In: *Proc. Natl. Acad. Sci. U. S. A.* 108,

- pp. 1–4. ISSN: 1091-6490. DOI: [10.1073/pnas.1110594108](https://doi.org/10.1073/pnas.1110594108). URL: <http://www.pubmedcentral.nih.gov/articlerender.fcgi?artid=3207700&tool=pmcentrez&rendertype=abstract>.
- Mao, W. L. et al. (2004). “Ferromagnesian post-perovskite silicates in the D” layer of the Earth”. In: *Proc. Natl. Acad. Sci.* 101.45, pp. 15867–15869. ISSN: 0027-8424. DOI: [10.1073/pnas.0407135101](https://doi.org/10.1073/pnas.0407135101). URL: <http://www.pnas.org/cgi/doi/10.1073/pnas.0407135101>.
- McCammon, C. A. (1997). “Perovskite as a possible sink for ferric iron in the lower mantle”. In: *Nature* 387.6634, pp. 694–696. ISSN: 00280836. DOI: [10.1038/42685](https://doi.org/10.1038/42685).
- Muir, J. M. R. and J. P. Brodholt (2016). “Ferrous iron partitioning in the lower mantle”. In: *Phys. Earth Planet. Inter.* 257, pp. 12–17. ISSN: 00319201. DOI: [10.1016/j.pepi.2016.05.008](https://doi.org/10.1016/j.pepi.2016.05.008). URL: <http://dx.doi.org/10.1016/j.pepi.2016.05.008>.
- Müller-Plathe, F. (1997). “A simple nonequilibrium molecular dynamics method for calculating the thermal conductivity”. In: *J. Chem. Phys.* 106.14, p. 6082. ISSN: 00219606. DOI: [10.1063/1.473271](https://doi.org/10.1063/1.473271). URL: <http://scitation.aip.org/content/aip/journal/jcp/106/14/10.1063/1.473271>.
- Murakami, M. et al. (2004). “Post-perovskite phase transition in MgSiO<sub>3</sub>”. In: *Science* (80-. ). 304, pp. 855–858.
- Naliboff, J. B. and L. H. Kellogg (2006). “Dynamic effects of a step-wise increase in thermal conductivity and viscosity in the lowermost mantle”. In: *Geophys. Res. Lett.* 33, pp. 1–4. ISSN: 0094-8276. DOI: [10.1029/2006GL025717](https://doi.org/10.1029/2006GL025717). URL: <http://doi.wiley.com/10.1029/2006GL025717>.
- Nieto-Draghi, C. and J. B. Avalos (2013). “Non-equilibrium momentum exchange algorithm for molecular dynamics simulation of heat flow in multicomponent systems”. In: *Mol. Phys.* 101.14, pp. 2303–2307. DOI: [10.1080/0026897031000154338](https://doi.org/10.1080/0026897031000154338).
- Oganov, A. R. and S. Ono (2004). “Theoretical and experimental evidence for a post-perovskite phase of MgSiO<sub>3</sub> in Earth’s D” layer”. In: *Nature* 430, pp. 445–448.
- Oganov, A. R., J. P. Brodholt, and D. G. Price (2000). “Comparative study of quasi-harmonic lattice dynamics, molecular dynamics and Debye model applied to MgSiO<sub>3</sub> perovskite”. In: *Phys. Earth Planet. Inter.* 122, pp. 277–288. URL: <http://www.sciencedirect.com/science/article/pii/S0031920100001977>.

- Ohta, K. et al. (2012). "Lattice thermal conductivity of MgSiO<sub>3</sub> perovskite and post-perovskite at the core–mantle boundary". In: *Earth Planet. Sci. Lett.* 349-350, pp. 109–115. ISSN: 0012821X. DOI: [10.1016/j.epsl.2012.06.043](https://doi.org/10.1016/j.epsl.2012.06.043). URL: <http://linkinghub.elsevier.com/retrieve/pii/S0012821X12003354>.
- Ohta, K., T. Yagi, and K. Hirose (2014). "Thermal diffusivities of MgSiO<sub>3</sub> and Al-bearing MgSiO<sub>3</sub> perovskites". In: *Am. Mineral.* 99, pp. 94–97. URL: <http://www.degruyter.com/view/j/am.2014.99.issue-1/ammin.2014.4598/ammin.2014.4598.xml>.
- Ohta, K. et al. (2017). "Thermal conductivity of ferropericlase in the Earth's lower mantle". In: *Earth Planet. Sci. Lett.* 465, pp. 29–37. ISSN: 0012821X. DOI: [10.1016/j.epsl.2017.02.030](https://doi.org/10.1016/j.epsl.2017.02.030). URL: <http://dx.doi.org/10.1016/j.epsl.2017.02.030>.
- Okuda, Y. et al. (2017). "The effect of iron and aluminum incorporation on lattice thermal conductivity of bridgmanite at the Earth's lower mantle". In: *Earth Planet. Sci. Lett.* 474, September, pp. 25–31. ISSN: 0012821X. DOI: [10.1016/j.epsl.2017.06.022](https://doi.org/10.1016/j.epsl.2017.06.022). URL: <http://dx.doi.org/10.1016/j.epsl.2017.06.022>.
- Osako, M. and E. Ito (1991). "Thermal diffusivity of MgSiO<sub>3</sub> perovskite". In: *Geophys. Res. Lett.* 18, pp. 239–242. URL: <http://onlinelibrary.wiley.com/doi/10.1029/91GL00212/full>.
- Padture, N. P. and P. G. Klemens (1997). "Low thermal conductivity in garnets". In: *J. Am. Ceram. Soc.* 80.4, pp. 1018–1020. ISSN: 00027820. DOI: [10.1111/j.1151-2916.1997.tb02937.x](https://doi.org/10.1111/j.1151-2916.1997.tb02937.x).
- Parise, J. B. and Y. Wang (1990). "Crystal structure and thermal expansion of (Mg,Fe)SiO<sub>3</sub> perovskite". In: *October* 12, pp. 2089–2092.
- Plimpton, S. (1995). "Fast parallel algorithms for short-range molecular dynamics". In: *J. Comput. Phys.* 117, pp. 1–19. ISSN: 00219991. DOI: [10.1006/jcph.1995.1039](https://doi.org/10.1006/jcph.1995.1039).
- Pozzo, M. et al. (2012). "Thermal and electrical conductivity of iron at Earth's core conditions". In: *Nature* 485.7398, pp. 355–358. ISSN: 00280836. DOI: [10.1038/nature11031](https://doi.org/10.1038/nature11031).
- Rost, S. et al. (2005). "Seismological constraints on a possible plume root at the core–mantle boundary". In: *Nature* 435.7042, pp. 666–669. ISSN: 00280836. DOI: [10.1038/nature03620](https://doi.org/10.1038/nature03620).

- Schelling, P. K., S. R. Phillpot, and P. Keblinski (2002). "Comparison of atomic-level simulation methods for computing thermal conductivity". In: *Phys. Rev. B* 65.14, p. 144306. ISSN: 1098-0121. DOI: [10.1103/PhysRevB.65.144306](https://doi.org/10.1103/PhysRevB.65.144306). URL: <http://link.aps.org/doi/10.1103/PhysRevB.65.144306>.
- Sellan, D. P. et al. (2010). "Size effects in molecular dynamics thermal conductivity predictions". In: *Phys. Rev. B* 81, pp. 1–10. ISSN: 1098-0121. DOI: [10.1103/PhysRevB.81.214305](https://doi.org/10.1103/PhysRevB.81.214305). URL: <http://link.aps.org/doi/10.1103/PhysRevB.81.214305>.
- Snyder, G. J. and E. S. Toberer (2008). "Complex thermoelectric materials". In: *Nat. Mater.* 7.2, pp. 105–114. ISSN: 1476-1122. DOI: [10.1038/nmat2090](https://doi.org/10.1038/nmat2090). arXiv: [1512.00567](https://arxiv.org/abs/1512.00567).
- Stackhouse, S. and L. Stixrude (2010). "Theoretical methods for calculating the lattice thermal conductivity of minerals". In: *Rev. Mineral. Geochemistry* 71, pp. 253–269. ISSN: 1529-6466. DOI: [10.2138/rmg.2010.71.12](https://doi.org/10.2138/rmg.2010.71.12). URL: <http://ring.geoscienceworld.org/cgi/doi/10.2138/rmg.2010.71.12>.
- Stackhouse, S., L. Stixrude, and B. B. Karki (2010). "Thermal Conductivity of Periclase (MgO) from First Principles". In: *Phys. Rev. Lett.* 104.20, p. 208501. ISSN: 0031-9007. DOI: [10.1103/PhysRevLett.104.208501](https://doi.org/10.1103/PhysRevLett.104.208501). URL: <http://link.aps.org/doi/10.1103/PhysRevLett.104.208501>.
- (2015). "First-principles calculations of the lattice thermal conductivity of the lower mantle". In: *Earth Planet. Sci. Lett.* 427, pp. 11–17. ISSN: 0012821X. DOI: [10.1016/j.epsl.2015.06.050](https://doi.org/10.1016/j.epsl.2015.06.050). URL: <http://dx.doi.org/10.1016/j.epsl.2015.06.050>.
- Tadano, T., Y. Gohda, and S. Tsuneyuki (2014). "Anharmonic force constants extracted from first-principles molecular dynamics: applications to heat transfer simulations." In: *J. Phys. Condens. Matter* 26, pp. 1–12. ISSN: 1361-648X. DOI: [10.1088/0953-8984/26/22/225402](https://doi.org/10.1088/0953-8984/26/22/225402). URL: <http://www.ncbi.nlm.nih.gov/pubmed/24824156>.
- Tang, X. and J. Dong (2009). "Pressure dependence of harmonic and anharmonic lattice dynamics in MgO: A first-principles calculation and implications for lattice thermal conductivity". In: *Phys. Earth Planet. Inter.* 174, pp. 33–38. ISSN: 00319201. DOI: [10.1016/j.pepi.2008.10.003](https://doi.org/10.1016/j.pepi.2008.10.003).



- Tang, X. and J. Dong (2010). "Lattice thermal conductivity of MgO at conditions of Earth's interior". In: *Proc. Natl. Acad. Sci.* 107.10, pp. 4539–4543. ISSN: 0027-8424. DOI: [10.1073/pnas.0907194107](https://doi.org/10.1073/pnas.0907194107). URL: <http://www.pnas.org/cgi/doi/10.1073/pnas.0907194107>.
- Tang, X. et al. (2014). "The thermal conductivity of the Earth's lower mantle". In: *Geophys. Res. Lett.* 41, pp. 2746–2752. DOI: [10.1002/2014GL059385](https://doi.org/10.1002/2014GL059385). Received. URL: <http://onlinelibrary.wiley.com/doi/10.1002/2014GL059385/pdf>.
- Tosi, N. et al. (2013). "Mantle dynamics with pressure- and temperature-dependent thermal expansivity and conductivity". In: *Phys. Earth Planet. Inter.* 217, pp. 48–58. ISSN: 00319201. DOI: [10.1016/j.pepi.2013.02.004](https://doi.org/10.1016/j.pepi.2013.02.004). URL: <http://dx.doi.org/10.1016/j.pepi.2013.02.004>.
- Touloukian, Y. S. et al. (1970). "Thermal conductivity of nonmetallic solids". In: *Thermophys. Prop. Matter* 2, pp. 183–193.
- Trønnes, R. G. (2009). "Structure, mineralogy and dynamics of the lowermost mantle". In: *Mineral. Petrol.* 99, pp. 243–261. ISSN: 0930-0708. DOI: [10.1007/s00710-009-0068-z](https://doi.org/10.1007/s00710-009-0068-z). URL: <http://link.springer.com/10.1007/s00710-009-0068-z>.
- Turney, J. E. et al. (2009). "Predicting phonon properties and thermal conductivity from anharmonic lattice dynamics calculations and molecular dynamics simulations". In: *Phys. Rev. B - Condens. Matter Mater. Phys.* 79.6, pp. 1–12. ISSN: 10980121. DOI: [10.1103/PhysRevB.79.064301](https://doi.org/10.1103/PhysRevB.79.064301).
- Wang, Z. and X. Ruan (2017). "On the domain size effect of thermal conductivities from equilibrium and nonequilibrium molecular dynamics simulations". In: *J. Appl. Phys.* 121.044301, pp. 1–8. DOI: [10.1063/1.4974884](https://doi.org/10.1063/1.4974884). URL: <http://dx.doi.org/10.1063/1.4974884>.